STRUCTURE OF THE Mn-Na_2WO_4/SiO_2 CATALYST FOR OXIDATIVE COUPLING OF METHANE (OCM) AT REAL REACTION CONDITIONS

Carlos Andres Ortiz Bravo

Tese de Doutorado apresentada ao Programa de Pós-graduação em Engenharia Química, COPPE, da Universidade Federal do Rio de Janeiro, como parte dos requisitos necessários à obtenção do título de Doutor em Engenharia Química.

Orientadores: Fabio Souza Toniolo
Carlos Alberto Chagas

Rio de Janeiro

Agosto de 2021

STRUCTURE OF THE Mn-Na_2WO_4/SiO_2 CATALYST FOR OXIDATIVE COUPLING OF METHANE (OCM) AT REAL REACTION CONDITIONS

Carlos Andres Ortiz Bravo

TESE SUBMETIDA AO CORPO DOCENTE DO INSTITUTO ALBERTO LUIZ COIMBRA DE PÓS-GRADUAÇÃO E PESQUISA DE ENGENHARIA DA UNIVERSIDADE FEDERAL DO RIO DE JANEIRO COMO PARTE DOS REQUISITOS NECESSÁRIOS PARA A OBTENÇÃO DO GRAU DE DOUTOR EM CIÊNCIAS EM ENGENHARIA QUÍMICA.

Orientadores: Fabio Souza Toniolo
Carlos Alberto Chagas

Aprovada por: Prof. Fabio Souza Toniolo
Prof. Carlos Alberto Chagas
Dra. Neuman Solange de Resende
Prof. Sebastián Henrique Collins
Dra. Cristiane Barbieri Rodella
Dr. Antônio Marcos Fonseca Bidart

RIO DE JANEIRO, RJ - BRASIL
AGOSTO DE 2021

Bravo, Carlos Andres Ortiz

Structure of the Mn-Na_2WO_4/SiO_2 catalyst for Oxidative Coupling of Methane (OCM) at Real Reaction Conditions / Carlos Andres Ortiz Bravo. – Rio de Janeiro: UFRJ/COPPE, 2021.

XII, 101 p.: il.; 29,7 cm.

Orientadores: Fabio Souza Toniolo

Carlos Alberto Chagas

Tese (doutorado) – UFRJ/ COPPE/ Programa de Engenharia Química, 2021.

Referências Bibliográficas: p. 87-101.

1. Acoplamento oxidativo de metano. 2. Espectroscopia. 3. Catálise. 4. *Operando.* 5. *In situ*. I. Toniolo, Fabio Souza *et al*. II. Universidade Federal do Rio de Janeiro, COPPE, Programa de Engenharia Química. III. Título.

A mi familia y amigos, y en especial
a mi nona Elvia, a quien siempre llevaré en mi corazón.

Acknowledgments

A presente tese envolveu a participação e colaboração de diferentes instituições e pessoas que gostaria de agradecer:

As entidades de financiamento pela concessão da bolsa de doutorado do CNPQ [165782/2018-8], de doutorado aluno nota 10 da FAPERJ [E-26/200.785/2019] e de doutorado sanduiche da CAPES [88887.368574/2019-00].

O Programa de Engenharia Química – PEQ, o Instituto Alberto Luiz Coimbra de Pós-Graduação e Pesquisa em Engenharia – COPPE e a Universidade Federal do Rio de Janeiro – UFRJ, pelo suporte e instalações de pesquisa.

Meus orientadores, Dr. Fabio Souza Toniolo e Dr. Carlos A. Chagas, pelo acompanhamento e apoio em cada etapa do meu doutorado, em especial, na exaustiva coleta de dados no Laboratório Nacional de Luz Sincrotron – LNLS (Campinas, SP).

Meus coautores, Dr. Miguel A. Bañares e Dra. Raquel Portela, por terem me acolhido no Instituto de Catálisis y Petroleoquímica – ICP del Consejo Superior de Investigaciones Científicas – CSIC (Madrid, Espanha) durante meu doutorado sanduiche. Foram seis meses de muito trabalho, mas também de muito aprendizado pessoal e profissional. Também, o Dr. Santiago Figueroa, por ter comprado minha ideia e me apoiado na obtenção e análise dos dados no LNLS.

Meus colegas de laboratório, Dra. Maria Auxiliadora S. Baldanza, Antônio José de Almeida e o pessoal do I-2000 do NUCAT, pela ajuda sempre oportuna e contundente no desenvolvimento dos set-ups experimentais. O pessoal da unidad de apoyo do ICP pela obtenção dos XRD. E o pessoal do laboratório de química do LNLS.

Minha família e amigos que me apoiaram e questionaram minhas ideias.

Muito obrigado por tudo!

Resumo da Tese apresentada à COPPE/UFRJ como parte dos requisitos necessários para a obtenção do grau de Doutor em Ciências (D.Sc.)

ESTRUTURA DO CATALISADOR Mn-Na_2WO_4/SiO_2 PARA O ACOPLAMENTO OXIDATIVO DE METANO (OCM) EM CONDIÇÕES REAIS DE REAÇÃO

Carlos Andres Ortiz Bravo

Agosto/2021

Orientadores: Fabio Souza Toniolo
Carlos Alberto Chagas

Programa: Engenharia Química

O desempenho do catalisador Mn-Na_2WO_4/SiO_2 para OCM é associado a fases cristalinas que não estão presentes em condições reais de reação. Neste trabalho se estuda a estrutura dos sítios W e Mn nos catalisadores 2% Mn-5% Na_2WO_4/SiO_2, 5% Na_2WO_4/SiO_2 e 3.1% WO_3/SiO_2 (% em massa) para OCM em condições ambiente, *in situ* e *operando* via DRX e espectroscopias Raman e XANES. As fases cristalinas identificadas a temperatura ambiente se transformam durante o aquecimento sob fluxo oxidante: γ→β→α-WO_3, α→β-cristobalita e cúbico→ortorômbico→fundido-Na_2WO_4. A ordem de ligação dos sítios W com simetria octaédrica (O_h) e tetraédrica (T_d) muda durante as transições γ→β→α-WO_3 e cúbico→ortorômbico→fundido-Na_2WO_4, respetivamente. Estas variações se devem a mudanças no grau de distorção dos sítios W, pois todas as amostras preservam principalmente valência W^{6+} no aquecimento. Os sítios O_h-W^{6+} são inativos e os sítios T_d-W^{6+} são menos distorcidos e mais ativos para a ativação do metano na presença dos sítios O_h-Mn^{3+}. Os sítios T_d-W^{6+} e O_h-Mn^{3+} continuam presentes mesmo se o aquecimento é feito sob uma mistura de gases OCM e efetuam reações OCM em estado estável. Por fim, o catalisador Mn-Na_2WO_4/SiO_2 efetua reações OCM sem oxigênio na fase gasosa devido à redutibilidade do Mn.

Abstract of Thesis presented to COPPE/UFRJ as a partial fulfillment of the requirements for the degree of Doctor of Science (D.Sc.)

STRUCTURE OF THE Mn-Na_2WO_4/SiO_2 CATALYST FOR OXIDATIVE COUPLING OF METHANE (OCM) AT REAL REACTION CONDITIONS

Carlos Andres Ortiz Bravo

August/2021

Advisors: Fabio Souza Toniolo
Carlos Alberto Chagas

Department: Chemical Engineering

The OCM performance of the Mn-Na_2WO_4/SiO_2 catalyst has been ascribed to crystalline phases that are not present at real reaction conditions. This work studies the W and Mn sites structure on the 2wt.% Mn-5wt.% Na_2WO_4/SiO_2, 5wt.% Na_2WO_4/SiO_2, and 3.1wt. % WO_3/SiO_2 catalysts for OCM at ambient, *in situ*, and *operando* conditions via XRD, Raman, and XANES spectroscopies. The crystalline phases identified at room temperature transform at heating under oxidizing conditions: γ→β→α-WO_3, α→β-cristobalite, and cubic→orthorhombic→molten-Na_2WO_4. The bond order of the W sites with octahedral (O_h) and tetrahedral (T_d) symmetry changes during the γ→β→α-WO_3 and cubic→orthorhombic→molten-Na_2WO_4 transitions, respectively. Such bond order changes are due to distortion degree variations because all samples preserve essentially W^{6+} valence at heating. O_h-W^{6+} sites are inactive and T_d-W^{6+} sites are less distorted and more active towards methane activation in the presence of O_h-Mn^{3+} sites. The T_d-W^{6+} and O_h-Mn^{3+} sites are present even at heating under an OCM gas mixture and perform OCM reactions at steady-state. Finally, the Mn-Na_2WO_4/SiO_2 catalyst performs OCM reactions in the absence of gas-phase oxygen due to the Mn reducibility.

SUMMARY

List of Figures

List of Tables

Chapter 1

"*El mundo era tan reciente, que muchas cosas carecían de nombre, y para mencionarlas había que señalarlas con el dedo*" – Gabriel García Márquez

Introduction

1.1 Background and Motivation

The increasing worldwide reserves of natural gas and the lack of an efficient industrial process for methane upgrading have renewed interest in the oxidative coupling of methane (OCM) (FARRELL *et al.*, 2016, MCFARLAND, 2012). Since the unprecedented work of KELLER & BHASIN (1982), OCM has been known as a promising route to directly convert methane into C_2 hydrocarbons (*i.e.*, ethane and ethylene). However, the industrial deployment of the OCM route remains limited by the low C_2 yield resulting from inherent thermodynamic and kinetic limitations. Indeed, the high stability of methane and the faster formation of more thermodynamically stable CO_x compounds compared with that of C_2 hydrocarbons result in low, not economically competitive, C_2 yields (FARRELL *et al.*, 2016, SCHWACH *et al.*, 2017, STANSCH *et al.*, 1997). Among hundreds of materials tested in the past decades, Mn-Na_2WO_4/SiO_2 is considered as the state-of-the-art catalyst, exhibiting high stability (~ 500 h on stream) and C_2 yields (14 - 27%) (ARNDT *et al.*, 2012, KIANI *et al.*, 2019). However, for the OCM route to be economically viable, a single-pass C_2 yield of 30% and a C_2 selectivity of 90% are necessary (CRUELLAS *et al.*, 2019, KUO *et al.*, 1989).

Although a fundamental understanding of the Mn-Na_2WO_4/SiO_2 catalyst is crucial to design improved formulations, the literature remains unclear about the nature of the active sites and the mechanism for the selective activation of methane. Several studies have ascribed the performance of the Mn-Na_2WO_4/SiO_2 catalyst for OCM to W^{6+} sites with distorted tetrahedral (T_d) oxygen coordination (FANG *et al.*, 1992, JIANG *et al.*, 1993, WU & LI, 1995). However, the proposed mechanisms for the selective activation of methane on these sites are inconsistent. WU *et al.* (1995) suggested that the activation of methane occurs at the T_d-W^{6+} sites via a $W^{6+}\leftrightarrow W^{4+}$ redox cycle, where gas-phase oxygen completes the cycle. Conversely, JIANG *et al.* (1997) proposed a $W^{6+}\leftrightarrow W^{5+}$ redox cycle along with a previous activation of gas-phase oxygen at the

Mn^{3+} sites with octahedral (O_h) oxygen coordination. The O_h-Mn^{3+} would act as oxygen storage-release sites via $Mn^{2+} \leftrightarrow Mn^{3+}$ redox cycle, supplying activated oxygen species to the T_d-W^{6+} sites. On the other hand, WANG *et al.* (1995) proposed that the active sites are the Mn-O-Na instead of T_d-W^{6+}. The activation of gas-phase oxygen would occur at the Mn-O-Na sites via dissociative adsorption, forming Mn-O-Na$\cdots O^{\cdot}$ sites, where methane then activates by cleaving C-H bond. However, W appears as a crucial performer: ELKINS & HAGELIN-WEAVER (2015) recently showed the poor OCM performance of catalysts without W.

Most OCM studies have associated crystalline phases observed via X-ray powder diffraction (XRD) at ambient conditions with the presence of the proposed active sites during OCM reactions. For instance, the T_d-W^{6+} sites have been associated with the crystalline Na_2WO_4 phase (W^{6+} ions with T_d coordination) (FANG *et al.*, 1992, JIANG *et al.*, 1993, WU & LI, 1995, WU *et al.*, 1995), whereas the O_h-Mn^{3+} sites have been associated with Mn_2O_3 (JIANG *et al.*, 1997). Thus, the crystalline Na_2WO_4 and Mn_2O_3 phases have been proposed to be active for OCM. Moreover, the formation of the crystalline α-cristobalite phase from amorphous SiO_2 support during catalyst calcination has been proposed to be critical for stabilizing the T_d-W^{6+} sites (ELKINS & HAGELIN-WEAVER, 2015, PALERMO *et al.*, 1998, PALERMO *et al.*, 2000). Although other crystalline phases may also be present, depending on the catalyst synthesis method and precursors ($Na_2W_2O_7$, $MnWO_4$, and $MnMn_6SiO_2$) (JI *et al.*, 2002, 2003, WANG, Jiaxin *et al.*, 2006), the absence of either Na_2WO_4, Mn_2O_3, or α-cristobalite phases has been associated with worse OCM performances (*i.e.*, lower C_2 yield).

The identification of active species via XRD is, however, limited to the observation of crystalline phases, being unable to report the potential presence of other structures, such as molecularly dispersed, amorphous, or molten phases. This is critical because some crystalline phases with weak diffraction pattern intensities, such as Mn_2O_3, may be overwhelmed by the intense pattern of other crystalline phases, such as Mn_7SiO_{12}. Moreover, establishing structure-activity/selectivity relationships based only on *ex situ* XRD evidence may be inadequate because the crystalline phases identified at room temperature may not be present during reaction. This is the particular case of the Mn-Na_2WO_4/SiO_2 catalyst, which structure changes because of the typical high OCM temperatures and reagents flow. On the one hand, crystalline cubic Na_2WO_4 and α-cristobalite phases transform to molten Na_2WO_4 and β-cristobalite, respectively, at heating under oxidizing conditions, as evidenced by differential scanning calorimetry

(DSC) (SADJADI *et al.*, 2015), high energy X-ray diffraction computed tomography (XRD-CT) (VAMVAKEROS, *et al.*, 2015a, VAMVAKEROS *et al.* 2020a), and Raman spectroscopy (KIANI *et al.*, 2020, WERNY *et al.*, 2020). On the other hand, the presence of methane at relevant OCM temperatures (> 700 ºC) allows the $MnWO_4$ phase formation, converting O_h-Mn^{2+} and O_h-W^{6+} sites of the Mn_2O_3 and Na_2WO_4 phases, respectively, into O_h-Mn^{2+} and O_h-W^{6+} sites (*i.e.*, wolframite structure).

While the Mn-Na_2WO_4/SiO_2 catalyst is a very dynamic system, the current OCM literature does not provide complete information about the catalyst structure at real OCM reaction conditions. The XRD-CT studies fail to reveal the structure of the W sites under oxidizing conditions at temperatures above 680 ºC because of the Na_2WO_4 melting (VAMVAKEROS, A. *et al.*, 2015b) and XANES spectroscopy results were reported only in *ex situ* conditions (KOU *et al.*, 1998a). Therefore, determining the structure of the catalyst at real OCM reaction conditions is critical to understand the nature of the species involved in the catalytic cycle, thus contributing to the rational design of improved formulations.

1.2 Objectives

In the framework described above, this thesis aims to contribute to elucidating the Mn-Na_2WO_4/SiO_2 catalyst structure at real OCM reaction conditions. For this purpose, some objectives may be listed as follows:

- To prepare the conventional 2wt.% Mn-5wt.% Na_2WO_4/SiO_2 catalyst and the Mn-free 5wt.% Na_2WO_4/SiO_2, and Mn- and Na-free 3.1wt.% WO_3/SiO_2 catalysts for comparison.
- To characterize the synthesized catalysts at ambient conditions to ensure they correspond to the materials widely reported in the literature.
- To monitor the structure of the W and Mn sites on the synthesized catalysts at heating under oxidizing conditions, which is the typical pretreatment used for testing the steady-state OCM catalytic performance.
- To verify if methane flow admission into the reactor introduces changes on the catalyst structure previously characterized at high temperatures under oxidizing conditions.
- To elucidate the nature of the lattice oxygen of the Mn-Na_2WO_4/SiO_2 catalyst.

1.3 Thesis Outline

The present thesis splits into five main chapters after this introduction. Chapter 2 presents a critical literature review of the challenges and opportunities for developing methane upgrading technologies via the OCM route. The high stability of the methane molecule and the inherent thermodynamic and kinetic limitations of the OCM route, responsible for the low and not economically competitive C_2 yields, are discussed. Furthermore, fundamentals to be considered to design improved OCM catalysts, such as C-H bond activation, tuning of electronic properties of oxide-based catalysts, and active oxygen species are analyzed. Finally, common insights about the Mn-Na_2WO_4/SiO_2 catalyst are presented by contrasting the well-consolidated literature with recent fast-developing *in situ*/*operando* studies.

Chapter 3 address all experimental methods employed: bulk- and surface-sensitive characterization techniques and steady-state and dynamic catalytic tests. The characterization techniques were performed at *i*) ambient conditions (room temperature and atmosphere), *ii*) *in situ* (at heating under oxidizing conditions), and *iii*) *operando* conditions (under an OCM gas mixture flow at temperatures above 700 ºC). In sequence, Chapter 4 presents the catalyst characterization results at ambient and *in situ* conditions, contrasting the catalyst structure with steady-state OCM catalytic tests. While catalyst characterization at ambient conditions is required to ensure that synthesized catalysts correspond to the materials widely reported in the literature, *in situ* characterization is required to monitor the structural changes introduced at heating under oxidizing conditions. The latter is the typical pretreatment used to measure the steady-state OCM performance of this catalyst. Chapter 5 discusses the catalyst structure in *operando* conditions. Here, methane-flow-induced changes on catalyst structure are measured by co-feeding methane and gas-phase oxygen or feeding only methane, allowing catalyst lattice oxygen to participate in the OCM reactions. Finally, Chapter 6 wraps everything up in conclusions, including suggestions and perspectives for future works.

Chapter 2

"*Les géographies, dit le géographe, sont les livres les plus précieux de tous les livres. Elles ne se démodent jamais. Il est très rare qu'une montagne change de place. Il est très rare qu'un océan se vide de son eau. Nous écrivons des choses éternelles*" – Antoine de Saint-Exupéry

Literature Review

2.1 Methane Conversion Routes

The exploitation of unconventional reservoirs such as *shale*, *coalbed*, and *tight* formations by hydraulic fracturing (fracking) has increased worldwide reserves of natural gas in the past decade (KERR, 2010, MCFARLAND, 2012). In this regard, methane, the main component of natural gas, has gained attention as a primary source of fuels and chemicals. Unfortunately, most of these reservoirs are localized in remote areas, making methane transportation not economically viable (SCHWACH *et al.*, 2017). Because methane cannot be converted *on site* into easily transportable hydrocarbons or chemicals, it becomes an underused byproduct that is burned, releasing greenhouse gases (CO_x) (HORN & SCHLÖGL, 2015, TAIFAN & BALTRUSAITIS, 2016). Therefore, developing efficient methane upgrading technologies to utilize natural gas economically and making the oil industry more environmentally friendly is needed. The quest for conversion. Nowadays, methane can be converted via indirect or direct routes, as shown in Figure 2.1.

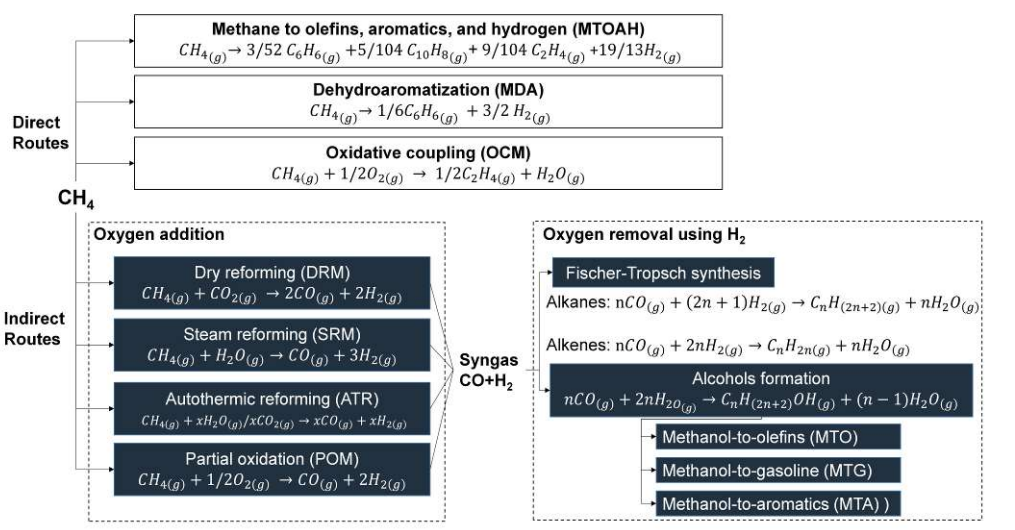

Figure 2.1 Methane conversion routes.

The industrial conversion of methane typically proceeds via indirect routes, which require the intermediate step of producing synthesis gas (syngas, CO + H_2). Here, methane is initially reformed to syngas and then converted to olefins, gasoline, diesel, or oxygenates via the Fischer-Tropsch synthesis (FTS). Alternatively, syngas can be converted to methanol and then to small olefins (methanol-to-olefins), gasoline (methanol-to-gasoline), or aromatics (methanol-to-aromatics) (HORN & SCHLÖGL, 2015, SCHWACH *et al.*, 2017). However, the sequence of initially oxidize methane to syngas and then reduce CO to a desirable product has several disadvantages. Firstly, methane reforming processes are energy-intensive and require high temperatures and pressures (15 - 40 atm, 700 - 900 ºC) (IULIANELLI *et al.*, 2016, JANG *et al.*, 2019). Secondly, the FTS needs CO or H_2 to remove oxygen from CO, resulting in a carbon-atom utilization efficiency below 50% (GUO *et al.*, 2014). Furthermore, the H_2 used here is typically obtained by cracking naphtha, which emits enormous CO_2 amounts. Finally, methane reforming and FTS processes have operating problems, such as carbonaceous deposit formations and sintering, which lead to catalyst deactivation (JANG *et al.*, 2019, RYTTER & HOLMEN, 2015).

The conversion of methane also proceeds via direct routes, which are cheaper and simpler because they do not involve syngas production. These routes can be either nonoxidative, such as *methane to olefins, aromatics, and hydrogen* (MTOAH) (GUO *et al.*, 2014) and *methane dehydroaromatization* (MDA) (WANG *et al.*, 1993) or oxidative, such as *oxidative coupling of methane* (OCM) (KELLER & BHASIN, 1982). Although the nonoxidative routes offer some advantages, such as *i*) potential operation in remote areas since no reagents are needed and *ii*) no explosion risk or CO_x emissions because of the oxygen absence, they present several drawbacks (HUANG *et al.*, 2018, SCHWACH *et al.*, 2017, SPIVEY & HUTCHINGS, 2014). While MTOAH suffers from high-temperature requirements and narrow operating conditions, MDA suffers from coke formation, catalyst stability issues, and low methane conversion (SCHWACH *et al.*, 2017). Conversely, the OCM route occurs at wider operating conditions, lower temperatures, and higher methane conversions (SCHWACH *et al.*, 2017). The OCM directly converts methane into ethane and ethylene (C_2 hydrocarbons), with ethylene being an important building block to produce a wide range of chemicals, such as cosmetics, detergents, lubricants, and polymers (FAN *et al.*, 2013, SCHWACH *et al.*, 2017).

Since the unprecedented work of KELLER & BHASIN (1982), the OCM route has attracted attention as a technology to supply the chemical industry with raw materials and minimize crude oil dependency. However, after decades of research, the industrial deployment of the OCM route remains limited (CRUELLAS *et al.*, 2019, KUO *et al.*, 1989, ORTIZ-ESPINOZA *et al.*, 2017, SPALLINA *et al.*, 2017). The OCM route suffers from selective issues, where undesirable deep oxidation compounds (CO_x) are more thermodynamically stable and produce faster than C_2 hydrocarbons (CRUELLAS *et al.*, 2019, KUO *et al.*, 1989, ORTIZ-ESPINOZA *et al.*, 2017, SPALLINA *et al.*, 2017). These thermodynamic and kinetic OCM limitations are analyzed in the following section.

2.2 Thermodynamic OCM Limitations

To understand the inherent challenges of converting methane directly, the thermodynamic feasibility of some potential reactions is discussed in this section. Considering the MDA route as a set of separate reactions, the direct conversion of methane to benzene (C_6H_6), naphthalene ($C_{10}H_8$), ethane (C_2H_6), and ethylene (C_2H_4) may be described as follows:

$$CH_{4(g)} \rightarrow 1/6\ C_6H_{6(g)} + 3/2\ H_{2(g)} \quad \Delta G_r^{25\,^oC} = 75\ kJ\ mol^{-1} \quad \Delta H_r^{25\,^oC} = 89\ kJ\ mol^{-1} \qquad (2.1)$$

$$CH_{4(g)} \rightarrow 1/10\ C_{10}H_{8(g)} + 8/5\ H_{2(g)} \quad \Delta G_r^{25\,^oC} = 75\ kJ\ mol^{-1} \quad \Delta H_r^{25\,^oC} = 90\ kJ\ mol^{-1} \qquad (2.2)$$

$$CH_{4(g)} \rightarrow 1/2\ C_2H_{6(g)} + 1/2\ H_{2(g)} \quad \Delta G_r^{25\,^oC} = 50\ kJ\ mol^{-1} \quad \Delta H_r^{25\,^oC} = 33\ kJ\ mol^{-1} \qquad (2.3)$$

$$CH_{4(g)} \rightarrow 1/2\ C_2H_{4(g)} + H_{2(g)} \quad \Delta G_r^{25\,^oC} = 85\ kJ\ mol^{-1} \quad \Delta H_r^{25\,^oC} = 101\ kJ\ mol^{-1} \qquad (2.4)$$

The change in the Gibbs free energy ($\Delta G_r^{25\,^oC}$) for all considered reactions is positive at 25 ºC and 1 atm, indicating that the MDA route is not feasible at such conditions. However, the thermodynamic equilibrium can be shifted using two approaches: increasing system temperature or introducing an oxidant. To assess the first approach, the change in the Gibbs free energy for all considered reactions was calculated over a wide range of temperatures at 1 atm using Equation 2.5.

$$\Delta G_r^T = \sum_i \upsilon_i \cdot \Delta H_r(T) \ - \ T \ \sum_i \upsilon_i \cdot \Delta S_r(T) \qquad (2.5)$$

In which, ΔG_r^T is the change in the Gibbs free energy for a certain reaction *r* at a temperature *T*, υ_i is the stoichiometric coefficient of the species *i*, and $\Delta H_r(T)$ and $\Delta S_r(T)$ are the change in the enthalpy and entropy of the species *i* at a temperature *T*, respectively. The thermodynamic data for each compound were collected from the NIST online library. Figure 2.2 depicts the calculated change in the Gibbs free energy for all considered reactions. Appendix A presents complete thermodynamic calculations.

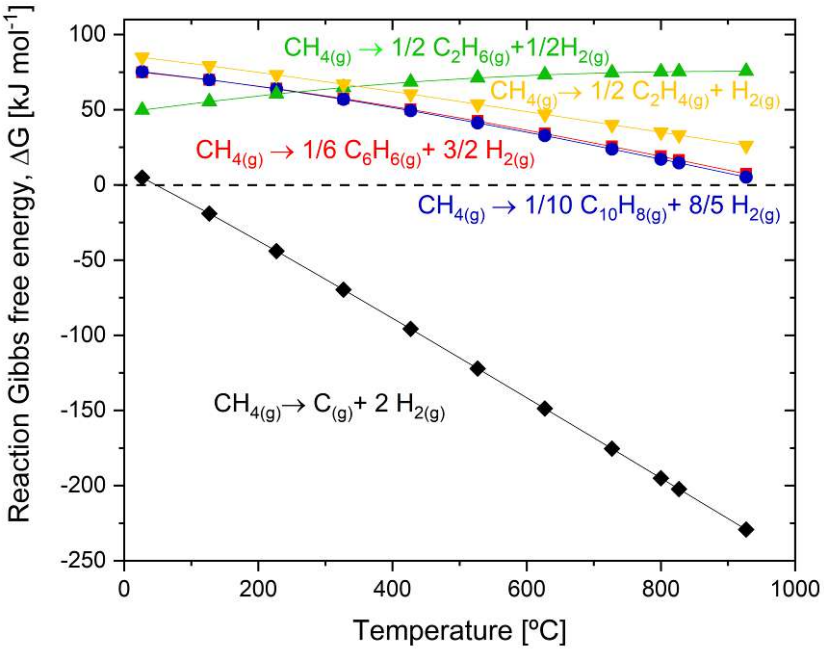

Figure 2.2 Change in the Gibbs free energy as a function of temperature for a set of potential reactions that can occur in the MDA route at 1 atm.

The ΔG_r^T for the formation of benzene and naphthalene are lower than that for the formation of ethane and ethylene at temperatures above ~ 240 ºC and decrease with temperature. This indicates that the formation of aromatics is more favorable than that of C_2 hydrocarbons under such conditions. However, aromatics production is thermodynamically limited even at high temperatures and competes with carbon formation. While the production of benzene and naphthalene becomes spontaneous ($\Delta G_r^T = 0$) above 900 ºC, the formation of carbon (coke) becomes above ~ 50 ºC, with ΔG_r^T sharply decreasing with temperature. The extensive formation of coke is the main drawback of the MDA route, as discussed elsewhere (SPIVEY & HUTCHINGS, 2014).

The second approach to shift the thermodynamic equilibrium is introducing an oxidant. This approach is known as the oxidative coupling of methane (OCM) route when oxygen is feeding at CH_4/O_2 molar ratios ≥ 2. Here, the formation of oxygen-containing species (H_2O and CO_x) provides the thermodynamic driving force to obtain negative ΔG_r^T values. Thus, the OCM route directly converts methane into desirable C_2 hydrocarbons (*i.e.*, ethane and ethylene) and undesirable CO_x compounds. Considering the OCM route as a set of separate reactions (Equations A.1-A.4 in Appendix A), the ΔG_r^T over a wide range of temperatures at 1 atm was calculated using Equation 2.5, and the results are shown in Figure 2.3.

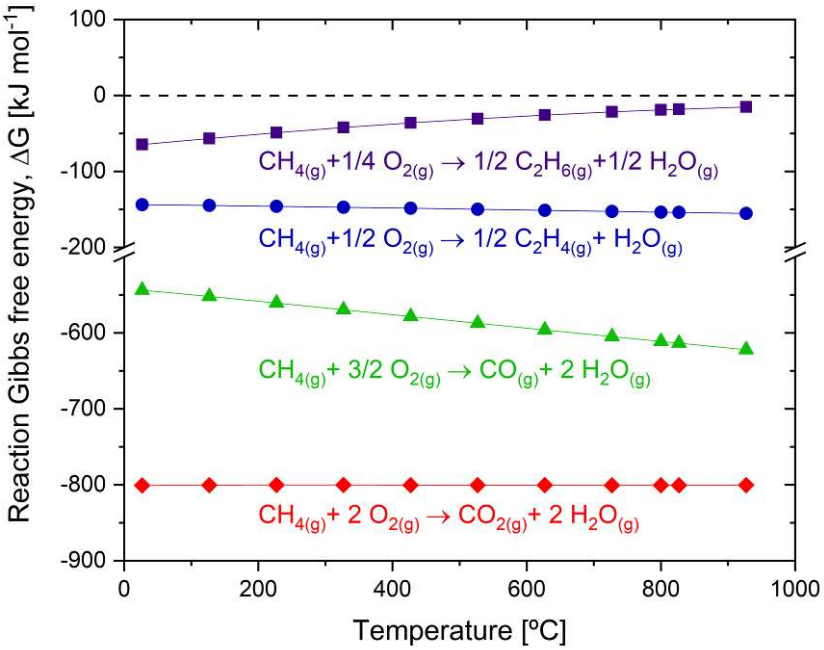

Figure 2.3 Change in the Gibbs free energy as a function of temperature for a set of potential reactions that can occur in the OCM route at 1 atm.

The OCM route is more favorable thermodynamically than the nonoxidative MDA route, with ΔG_r^T being negative for all considered reactions in the evaluated temperature window. However, although the ΔG_r^T for the formation of ethylene becomes slightly more negative with temperature, the formation of CO and CO_2 compounds goes even more downhill energetically. Therefore, the formation of deep oxidation products (CO_x) is more favorable thermodynamically than that of desirable C_2 hydrocarbons, thus decreasing the C_2 selectivity. This partially explains why the OCM route has not achieved industrial deployment. Techno-economic projections calculate that for the OCM route to be economically viable, a single-pass yield to C_2

hydrocarbons between 25 - 30% is needed (CRUELLAS *et al.*, 2019, KUO *et al.*, 1989). However, despite the numerous works, this techno-economic target has not been achieved. Finally, the high exothermicity of the OCM route is another important thermodynamic property to be considered. Figure A.1 shows that the change in the enthalpy, $\Delta H_r(T)$, for all considered reactions is negative in the evaluated temperature range. Note that deep oxidation reactions to form CO_x compounds release more heat than selective reactions to form C_2 hydrocarbons.

2.3 Kinetic OCM Limitations

The analysis of the OCM kinetic limitations is challenging because the complete set of the catalytic reaction pathways in this route remains unclear. The discrepancies in the literature are due to different reasons. Firstly, OCM follows a heterogeneous-homogeneous reaction pathway, with heterogeneous and homogeneous reactions having a strong influence on each other. Hundreds of OCM kinetic studies have used different catalysts, which led to different heterogeneous-homogeneous reactions that hinder comparison (PAK *et al.*, 1998a, STANSCH *et al.*, 1997, TAKANABE & IGLESIA, 2009). Secondly, rapid free-radical homogeneous reactions in the gas phase make the complete identification of involved species not easy (DOOLEY *et al.*, 2010, FLEISCHER *et al.*, 2016). Furthermore, several studies consider a great number of species (radical species). For instance, DOOLEY *et al.* (2010) proposed a microkinetic model with a network of 1582 reactions and 269 radical species. Thirdly, the high exothermicity of the OCM route may lead to the appearance of high-temperature zones in the catalytic bed called *hot spots*, hindering the temperature control (LEE *et al.*, 2013, SCHWACH *et al.*, 2017). Finally, typical high OCM temperatures induce structural and chemical changes in the catalysts, leading to rapid changes in the catalytic activity (ARNDT *et al.*, 2011, KARAKAYA & KEE, 2016, VAMVAKEROS *et al.*, 2015a).

Despite the discrepancies in the literature, most of the studies agree that the selective methane conversion via OCM occurs *via* three stages: (*i*) heterogeneous activation of methane on the catalyst surface yielding methyl radicals ($CH_3^{\bullet}$), (*ii*) homogeneous coupling of two $CH_3^{\bullet}$ to ethane, and (*iii*) oxidative dehydrogenation of ethane to ethylene (KIANI *et al.*, 2019, LOMONOSOV & SINEV, 2016, LUNSFORD, 1989, SINEV *et al.*, 2003). Unfortunately, methane, ethane, and ethylene also follow deep oxidation reactions to CO_x compounds that may occur in the gas phase and

catalyst surface. Table 2.1 presents the reaction steps of some OCM kinetic models over different catalysts. Such models propose similar pathways for reactants and products but different reaction steps, component types, and rate equations. Although the catalytic OCM reaction pathways are strongly dependent on the type of catalyst used, some kinetic models may describe the kinetic behavior over other catalysts. DANESHPAYEH *et al.* (2009) compared the models proposed by OLSBYE *et al.* (1992) over $BaCO_3/La_2O_n(CO_3)_{3-n}$ (n>1.5), LACOMBE *et al.* (1995) over La_2O_3, SOHRABI *et al.* (1996) over $CaTiO_3$**,** STANSCH *et al.* (1997) over La_2O_3/CaO, and TRAYKOVA *et al.* (1998) over La_2O_3/MgO to identify the best reaction network to describe the kinetic behavior over the Mn-Na_2WO_4/SiO_2 catalyst. The authors estimated the parameters of the rate equations using a decimal genetic algorithm of optimization. After discriminating these models, the model of STANCH *et al*. (1997) showed the best accuracy.

Table 2.1 Stoichiometric equations of the proposed kinetic models for OCM over different catalysts.

Step	**Reaction \ Reference**	(OLSBYE *et al.*, 1992)	(LACOMBE *et al.*, 1995)	(SOHRABI *et al.*, 1996)	(STANSCH *et al.*, 1997)	(TRAYKOVA *et al.*, 1998)	(SHAHRI & ALAVI, 2009)	(TIEMERSMA *et al.*, 2012)
1	$2CH_4+0.5O_2\rightarrow C_2H_6+2H_2O$	*	*	*	*	*	*	*
2	$CH_4+O_2\rightarrow CO+H_2O+H_2$	*			*			
3	$CH_4+1.5O_2\rightarrow CO+2H_2O$			*		*	*	
4	$CH_4+2O_2\rightarrow CO_2+2H_2O$	*	*	*	*		*	*
5	$2CH_4+O_2\rightarrow C_2H_4+2H_2O$			*				
6	$CO+0.5O_2\rightarrow CO_2$		*		*			
7	$C_2H_6+0.5O_2\rightarrow C_2H_4+H_2O$		*		*	*	*	*
8	$C_2H_6+O_2\rightarrow 2CO+3H_2$		*					
9	$C_2H_6+2.5O_2\rightarrow 2CO+3H_2O$	*						
10	$C_2H_6+3.5O_2\rightarrow 2CO_2+3H_2O$	*	*					*
11	$C_2H_6\rightarrow C_2H_4+H_2$	*			*	*		
12	$C_2H_4+O_2\rightarrow 2CO+2H_2$		*					
13	$C_2H_4+2O_2\rightarrow 2CO+2H_2O$	*			*		*	
14	$C_2H_4+3O_2\rightarrow 2CO_2+2H_2O$	*						*
15	$C_2H_4+2H_2O\rightarrow 2CO+4H_2$				*			
16	$CO_2+H_2\rightarrow CO+H_2O$				*	*	*	
17	$CO+H_2O\rightarrow CO_2+H_2$				*	*	*	

Reprinted (adapted) from DANESHPAYEH *et al.* (2009). Copyright (2021), with permission from Elsevier.

The kinetic model proposed by STANCH *et al*. (1997) involves three primary and seven consecutive reaction steps, as shown in Figure 2.4. In the three primary steps, methane is converted in parallel to ethane, CO, and CO_2 (steps 1, 2, and 4, in Table 2.1). The consecutive reactions involve the oxidative and thermal dehydrogenation of ethane (steps 7 and 11, in Table 2.1), oxidation and steam ethylene reforming (steps 13 and 15, in Table 1), oxidation of CO (step 6, in Table 2.1), and the water gas shift reactions (steps 16 and 17, in Table 2.1). The conversion of hydrocarbons and carbon monoxide with oxygen was described by applying the Hougen-Watson type rate equation and the rest by power-law rate equations.

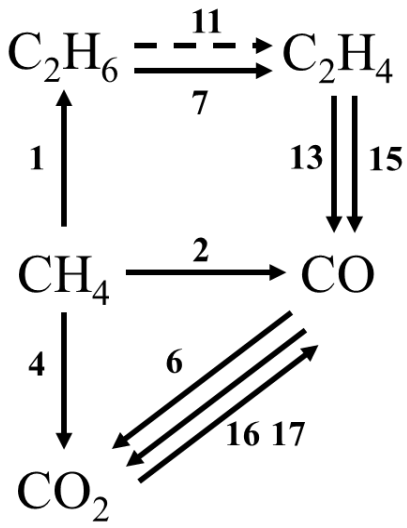

Figure 2.4 Reaction scheme (dashed line indicates gas-phase reaction) of the kinetic model proposed by STANSCH *et al.* (1997) for the OCM route. Reprinted (adapted) with permission from Ind. Eng. Chem. Res. Copyright 2021, American Chemical Society.

Although the kinetic model proposed by STANSCH *et al.* (1997) is relatively simple, it allows us to analyze general aspects of the OCM kinetic. Firstly, the formation rate of ethane and ethylene exhibits 0.4- and 0.37-order dependence on oxygen partial pressure, while the formation rate of CO_x compounds exhibits approximately 1.0-order dependence. TIEMERSMA *et al.* (2012) reported a similar dependence of C_2 hydrocarbons and CO_x production rate on the oxygen partial pressure in kinetic studies over the Mn-Na_2WO_4/SiO_2 catalyst. Thus, to achieve high C_2 selectivity, operating at low oxygen partial pressure is necessary. Secondly, the reaction rates calculated at selected reaction conditions (T = 1073 K, P_{CH4}= 63 kPa, P_{O2}= 4.2 kPa, P_{C2H6}= 1.9 kPa, P_{C2H4}= 0.6 kPa, P_{H2O}= 7.4 kPa, and P_{CO2}= 1.5 kPa) showed that oxidative dehydrogenation of ethane (r_7, step 7) and ethylene (r_{13}, step 13)

proceed faster than the methyl radicals coupling to ethane (r_1, step 1), that is, $r_7/r_2 = 5$ and $r_{13}/r_2 = 42$. This behavior is typical of processes where desired products sequentially convert to others more stable thermodynamically. Finally, the apparent activation energy to produce ethane was determined as 182 kJ mol^{-1}, which is similar to those reported for other La-containing catalysts (~172 kJ mol^{-1} for $BaCO_3/La_2O_n(CO_3)_{3-n}$ (n>1.5) (OLSBYE *et al.*, 1992) and ~165 kJ mol^{-1} for Sr-doped La_2O_3 (DEBOY, 1988)) and lower than for the Mn-Na_2WO_4/SiO_2 catalyst (~268 kJ mol^{-1}) (PAK *et al.*, 1998b). Meanwhile, the activation energies to form CO and CO_2 were lower than that to form ethane, 48 and 68 kJ mol^{-1}, respectively.

Regardless of the extensive number of published OCM kinetic models, the literature agrees that methane activation is the rate-determining step of the OCM route (KIANI *et al.*, 2019). TAKANABE & IGLESIA (2009) showed the kinetic relevance of the C-H bond activation by measuring kinetic isotope effects (KIE) for CH_4/O_2 and CD_4/O_2 reactants over the Mn-Na_2WO_4/SiO_2 catalyst. Normal KIE values of 1.24, 1.25, and 1.29 were determined for CH_4 - O_2/CD_4 - O_2 at oxygen partial pressures of 0.9, 1.8, and 3.5 kPa, respectively (TAKANABE & IGLESIA, 2009). This result shows that the C-H bond activation is the most relevant step kinetically. Similar studies were performed on other materials such as the Li-doped MgO catalyst (CANT *et al.*, 1993). Therefore, understanding the fundamentals of methane activation is critical to design improved OCM catalysts.

2.4 Methane Activation

The methane activation occurs by abstracting a hydrogen atom via C-H bond cleavage. However, the methane molecule is highly stable, exhibiting strong C-H bonds (first bond dissociation energy = 439.3 kJ mol^{-1}) (SCHWACH *et al.*, 2017) with weak polarization (2.84×10^{-40} C^2 m^2 J^{-1}) (AMOS, 1979). This is due to the geometrical structure of the methane molecule, where a central carbon atom is tetrahedrally coordinated (point group, T_d) to four hydrogen atoms (sp^3 hybridization) with C-H bond lengths of 1.090 Å and H-C-H bond angles of 109.47º (HORN & SCHLÖGL, 2015). Furthermore, methane is a very weak acid (pK_a ~ 48) (PAGANINI *et al.*, 2003) and has negligible electron affinity (-1.9 eV) (ZHAN *et al.*, 2003) and large ionization potential (12.6 eV) (BERKOWITZ *et al.*, 1987). Because of the T_d symmetry, methane does not present a dipole moment, which implies that it can resist a nucleophilic or electrophilic

attack (HORN & SCHLÖGL, 2015). However, if methane absorbs on the catalyst surface, the T_d symmetry decreases, giving rise to a distorted methane molecule (LI *et al.*, 1994). The imposed distortion decreases the bond order of the methane molecule by either elongating C-H bonds or varying H-C-H bond angles. In both cases, the C-H bond loses strength and cleaves to form a methyl group: an anion (CH_3^-) or a radical ($CH_3^\bullet$) in the heterolytic or homolytic C-H bond activation, respectively (SCHWACH *et al.*, 2017).

2.4.1 Heterolytic C-H bond activation under OCM conditions

GARRONE *et al.* (1980) studied the dissociative adsorption of acetylene, propane, and butane on the MgO surface via electron paramagnetic resonance (EPR) spectroscopy. The authors proposed the formation of carbanions (CH_3^-) and protons (H^+) from the heterolytic C-H bond cleavage. Thus, the heterolytic activation of methane may be understood as follows:

$$CH_{4\,(g)} \rightarrow CH^-_{3\,(ads)} + H^+_{(ads)} \tag{2.6}$$

Here, the catalyst allows for abstracting a hydrogen atom from methane via an acid-base reaction. Depending on the oxide basic strength, the dissociative adsorption of the weakly acidic methane involves the formation of two charged fragments (*i.e.*, CH_3 and H), one negatively and the other positively charged (SCHWACH *et al.*, 2017). Because these fragments are amphoteric, they may act as either an acid or a base. Recently, CHRÉTIEN & METIU (2014) used density-functional theory (DFT) to calculate the energy for the dissociative adsorption of methane on the La_2O_3 (001), MgO (001), and CaO (001) surfaces. The lowest adsorption energy resulted when H bounds to the lattice oxygen and CH_3 bounds to a cation site, that is, when CH_3^- and H^+ form, in agreement with ALJAMA *et al.* (2018). Subsequently, a proton (H^+) reacts with unsaturated surface lattice oxygen (O^{2-}) to form a surface hydroxyl (OH^-) as follows:

$$H^+_{(ads)} + O^{2-}_{(lat)} \rightarrow OH^-_{(ads)} \tag{2.7}$$

The desorption of a carbanion (CH_3^-) to the gas phase requires the loss of an electron to form a methyl radical ($CH_3^\bullet$). Over a nonreducible oxide, an oxidant agent (typically gas-phase oxygen) may accept this electron. However, over a reducible oxide,

the literature is unclear about if this electron is directly transferred to the oxidant agent or firstly transferred to the oxide as a polaron and then to the oxidant agent (SCHWACH *et al.*, 2017). Once gas-phase oxygen accepts this electron, a superoxide ion (O_2^-) is formed on the catalyst surface (CHIESA *et al.*, 2010, GARRONE *et al.*, 1980). Therefore, according to GARRONE *et al.* (1980), carbanion (CH_3^-) desorption in the presence of gas-phase oxygen yields a methyl radical ($CH_3^\bullet$) and a surface superoxide ion (O_2^-) as follows:

$$CH^-_{3\,(ads)} + O_{2\,(g)} \rightarrow CH^\bullet_{3\,(g)} + O^-_{2\,(ads)} \quad (2.8)$$

The final step of the heterolytic C-H bond activation is the formation of methyl radicals, which are required for the subsequent coupling reaction to ethane. Equation 2.8 suggests that the formation of methyl radicals requires the presence of gas-phase oxygen in the reactor when a nonreducible oxide is used as catalyst. Thus, in the absence of gas-phase oxygen, OCM occurs only if the catalyst can store and release oxygen (*i.e.*, materials with variable oxidation state) in agreement with KELLER & BHASIN (1982). Note that the electron resource to form superoxide ions on the oxide surface is the dissociative adsorption of methane (GARRONE *et al.*, 1980). Additionally, superoxide species are proposed to be very reactive and capable of promoting deep oxidation reactions to CO_x (MAITRA, 1993, SCHWACH *et al.*, 2017, VOSKRESENSKAYA *et al.*, 1995). Thus, superoxide ions dissipations should occur in selective OCM reaction pathways.

2.4.2 Homolytic C-H bond activation under OCM conditions

DRISCOLL *et al.* (1985) and later LIN *et al.* (1986) proposed the homolytic C-H bond activation. DRISCOLL *et al.*, (1985) studied the OCM performance of the MgO and Li-doped MgO catalysts. Over the Li-doped MgO catalyst, Li^+ ions react with lattice oxygen of the MgO framework to form $[Li^+O^-]$ sites. The resulting O^- site is a strong Lewis acid that can easily capture electrons and activate methane. Thus, a methyl radical ($CH_3^\bullet$) directly forms on an O^- site by abstracting a hydrogen atom from methane as follows:

$$[Li^+O^-] + CH_{4(g)} \rightarrow [Li^+OH^-] + CH^\bullet_{3(g)} \quad (2.9)$$

The resulting methyl radical is then released to the gas phase for the coupling reaction to ethane. Here, electrons are supplied to O^- sites as a hydrogen atom, forming a surface hydroxyl (OH^-). Note that methane interacts with the O^- site by the abstracted hydrogen instead of by its central carbon as occurs in the heterolytic C-H bond activation (SCHWACH *et al.*, 2017). Hydroxyl (OH^-) then forms either an F^+-center or an F-center, Equation 2.10. Furthermore, in the presence of gas-phase oxygen, $[Li^+O^-]$ sites are regenerated following Equation 2.11.

$$2\,[Li^+OH^-] \rightarrow [Li^+O^{2-}] + [Li^+]V_O^{\bullet\bullet} + H_2O \quad (2.10)$$

$$[Li^+O^{2-}] + [Li^+]V_O^{\bullet\bullet} + 1/2\,O_{2\,(g)} \rightarrow 2\,[Li^+O^-] \quad (2.11)$$

In which, using Kröger-Vink convention for the X_a^b notation, X is a species (*e.g.*, atom, vacancies, electrons, or electron-hole), the subscript a is the lattice site occupied by species X (*e.g.*, lattice or interstitial site), and the superscript b is the effective electronic charge of the species X. The symbols •, ´, and X denote positive, negative, and neutral effective electronic charges, respectively (´ and X not shown in Equations 2.10 and 2.11). Thus, $V_O^{\bullet\bullet}$ denotes a vacancy in an oxygen lattice site with an effective electronic charge of 2+. Furthermore, Equation 2.11 suggests that active sites are regenerated only in the presence of gas-phase oxygen. Note that the homolytic C-H bond activation considers the previous presence of O^- sites on the catalyst.

2.5 Gas-phase oxygen activation

As shown in the methane activation section, the charge transference between methane and the catalyst is crucial to produce methyl radicals ($CH_3^\bullet$), and thus, C_2 hydrocarbons. Since the first reports, the OCM literature has pointed out some metal oxides as good catalysts because of their high conductivity. Specifically, an electron-acceptor oxide (p-type conductors) is desirable to activate methane (ZHANG *et al.*, 1994). The increased C_2 selectivity evidenced for doped oxide-based catalysts is explaining in terms of oxygen-ion conductivity (ANSHITS *et al.*, 2016, MAITRA, 1993). Indeed, the conductivity of oxides can be tuned by inserting a foreign metal cation into its framework, in other words, by doping. Considering substitutional doping, the variation of the electronic properties (*i.e.*, Fermi level and electrical conductivity) depends on the valence of the foreign cation.

On the one hand, if the valence of the foreign cation is higher than that of the host cation, an electron deficiency arises. The resulting positive effective charge is compensated by forming either cationic vacancies or free or bound electrons in the host framework (*i.e.*, vacancies of the host metal atom) (ANSHITS *et al.*, 1990, SCHWACH *et al.*, 2017, VOSKRESENSKAYA *et al.*, 1995). For instance, the substitution of a Ca^{2+} cation for a La^{3+} cation in Ca-doped La_2O_3 creates a cationic vacancy ($V_{Ca}^{\prime}$) as follows:

$$La_2O_3 \rightleftarrows 2La_{Ca}^{\bullet} + 2V_{Ca}^{\prime} + 3O_O^{\times} \quad (2.12)$$

On the other hand, if the valence of the foreign cation is lower than that of the host cation, an electrons excess arises. For instance, one extra electron for each substituted Mg^{2+} cation by a Li^{+} cation in the conventional Li-doped MgO catalyst. The resulting negative effective charge is compensated either by forming anionic vacancies (*i.e.*, oxygen vacancies) or electron holes or by oxidizing host cation (ANSHITS *et al.*, 1990, SCHWACH *et al.*, 2017, VOSKRESENSKAYA *et al.*, 1995). For instance, the substitution of a Tb^{3+} cation for a Na^{+} cation in the Na-doped Tb_4O_7 creates an oxygen vacancy ($V_O^{\bullet\bullet}$) (Equation 2.13) or induces the oxidation of Tb cation from Tb^{3+} to Tb^{4+} (Equation 2.14).

$$3/2Na_2O \rightleftarrows 2Na_{Tb}^{\prime\prime\prime} + 2Na_{Tb}^{\prime\prime} + 4V_O^{\bullet\bullet} + 3/2O_O^{\times} \quad (2.13)$$

$$4Tb^{3+} + Na_2O \rightleftarrows 2Na_{Tb}^{\bullet} + 4Tb^{4+} + O^{2-} \quad (2.14)$$

The compensation process described by Equation 2.14 is not valid for alkali and alkaline-earth oxides because they present unchanging valence (*i.e.*, nonreducible oxides). Therefore, doping alkali and alkaline-earth oxides with lower valence cations only form oxygen vacancies ($V_O^{\bullet\bullet}$) or electron holes ($h^{\bullet}$). However, the stability of the oxygen vacancies depends on the oxygen partial pressure in the gas phase (VOSKRESENSKAYA *et al.*, 1995). For high oxygen partial pressures ($P_{O2} \geq 0.1$ kPa), gas-phase oxygen adsorbs on the oxide surface and then reduces, forming various oxygen intermediate species, such as peroxides (O_2^{2-}), O^{-} sites, lattice oxygen (O^{2-}), and free or bonded electron holes ($h^{\bullet}$) as follows:

$$V_O^{\bullet\bullet} + O_{2\,(g)} \rightleftarrows O_2^{2-} + 2h^{\bullet} \rightleftarrows 2O^{-} + 2h^{\bullet} \rightleftarrows 2O^{2-} + 4h^{\bullet} \quad (2.15)$$

If an electron-hole is strongly bound to the lattice oxygen, an O^- site forms with a strong radical character, such as the $[Li^+O^-]$ site in the Li-doped MgO catalyst. This process is known as gas-phase oxygen activation and may be understood as an acid-base reaction (SCHWACH *et al.*, 2017). The oxide with an excess of electrons acts as a Lewis base by transferring electrons to adsorbed diatomic oxygen (Lewis acid). Depending on the number of electrons transferred, adsorbed diatomic oxygen reduces, forming different electron-rich oxygen species (oxyanions) following Equation 2.15. The nature of these oxyanions is associated with the selectivity for OCM. Indeed, the formation of deep oxidation compounds (CO_x) is related to nucleophilic oxyanions, whereas the selective formation of C_2 hydrocarbons is related to electrophilic oxyanions. Nucleophilic oxyanions are species that can eventually donate an electron pair to an electrophilic species. Thus, the O^- site acts as electrophilic species because it accepts an electron during the homolytic C-H cleavage. Therefore, the gas-phase oxygen activation on the oxide surface is a critical step in the OCM route because it is directly associated with the C_2 selectivity.

Figure 2.5 depicts the gas-phase oxygen activation on the catalyst surface. Initially, gas-phase oxygen adsorbs on a free site of the catalyst surface, resulting in a diatomic oxygen molecule weakly bound to the catalyst surface and in equilibrium with gas-phase oxygen (FLEISCHER *et al.*, 2016, LEE *et al.*, 2012, SUN *et al.*, 2008). Adsorbed diatomic oxygen can then either reduce forming oxyanions or refill oxygen vacancies. As electrons are adding into an adsorbed diatomic oxygen, superoxide, peroxide, and lattice oxygen species are formed. Furthermore, the electron transference to adsorbed diatomic oxygen increases the adsorption strength and changes the nature of the oxygen species from nucleophilic to electrophilic (GAMBO *et al.*, 2018).

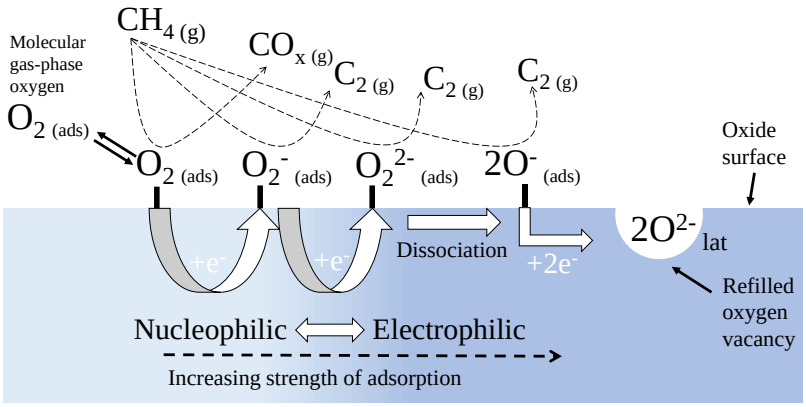

Figure 2.5 Schematic illustration of the gas-phase oxygen activation on the oxide catalyst surface.

Gas-phase oxygen adsorption on an n-type oxide (*e.g.*, reducible rare-earth oxides, such as CeO_2, Pr_6O_{11}, Tb_6O_7), however, is limited, thus they are known as poorly selective OCM catalysts (present low C_2 selectivity) (DUBOIS & CAMERON, 1990). The growth of repulsive forces between the negatively charged surface and mobile electrons avoids gas-phase oxygen absorbs on the oxide surface, even at high oxygen partial pressure ($P_{O2} \geq 0.1$ kPa) (VOSKRESENSKAYA *et al.*, 1995). Thus, electrophilic species required to selectively activate methane are not formed. The absence of electrophilic species makes methane directly activate on lattice oxygen (O^{2-}) of reducible rare-earth oxides, which are nucleophilic oxygen species that promote deep oxidation reactions.

2.6 The Mn-Na_2WO_4/SiO_2 catalyst

Among all materials used for OCM, Mn-Na_2WO_4/SiO_2 is considered as the state-of-the-art catalyst because it exhibits high C_2 yields (14 − 27%) (ARNDT *et al.*, 2012) and stability (450 − 1000 h) (CHUA *et al.*, 2008, LIU *et al.*, 2008, WANG *et al.*, 2006). The literature suggests that the remarkable performance of this catalyst lies in the synergistic interaction among the supported oxides (*i.e.*, MnO_x, NaO_x, and WO_x), as shown in Table 2.2.

Table 2.2 The OCM performance of mono, bi, and trimetallic oxide-supported catalysts. T = 1123 K; CH_4:O_2 = 4.5:1; total flow rate = 18 cm^3 min^{-1}; 0.4 g catalyst.

Catalyst	Crystalline phases	Methane conversion (%)	C_2 selectivity (%)	Ref.
SiO_2	Amorphous	27	23	(PALERMO *et al.*, 1998)
1.9wt.% Mn/SiO_2	Amorphous	23	23	(PALERMO *et al.*, 1998)
0.9wt.% Na/SiO_2	α-cristobalite	2	-	(PALERMO *et al.*, 2000)
4.1wt.% W/SiO_2	Amorphous	12	20	(PALERMO *et al.*, 1998)
2.0wt.% Mn-0.8wt.% Na/SiO_2 [a]	Not informed	2	58	(JI *et al.*, 2002)
1.9wt.% Mn-4.1wt.%W/SiO_2	Amorphous	20	40	(PALERMO *et al.*, 1998)
5.0wt.% Na_2WO_4/SiO_2	Na_2WO_4 α-cristobalite	44	52	(PALERMO *et al.*, 1998)
2.0wt%Mn-5.0wt.%Na_2WO_4/SiO_2	Na_2WO_4 α-cristobalite Mn_2O_3	33	80	(PALERMO *et al.*, 1998)

[a] 800 ºC; CH_4:O_2 = 3:1; GHSV = 36000 h^{-1}

The metal loadings on the different mono and bimetallic oxide catalysts in Table 2.2 are similar to that on the conventional trimetallic oxide Mn-Na_2WO_4/SiO_2 catalyst (*i.e.*, ~1.9wt.% Mn and ~4-5wt.% Na_2WO_4) (JIANG *et al.*, 1993). Bulk SiO_2 and Mn/SiO_2 are active but poorly selective for OCM, while Na/SiO_2 and W/SiO_2 are both inactive and unselective (PALERMO *et al.*, 2000). Adding Na (from NaOH) into the Mn/SiO_2 catalyst results in a more selective but less active catalyst while adding W (from $(NH_4)_2{\cdot}WO_4$) only increases the selectivity. The Na_2WO_4/SiO_2 catalyst (prepared from $Na_2WO_4{\cdot}H_2O$) is active and selective. Finally, adding Mn into the Na_2WO_4/SiO_2 catalyst leads to a decrease in the activity but a significant increase in the selectivity, exhibiting the highest C_2 yield (~ 26.4%). Thus, the absence of any supported metal compromises the OCM performance of the conventional trimetallic oxide Mn-Na_2WO_4/SiO_2 catalyst (*i.e.*, decreases C_2 yield).

The OCM literature has attempted to explain the synergistic effect by proposing active sites, selective methane activation mechanisms, and roles for each supported oxide. For this purpose, different combinations and composition variations of the conventional trimetallic oxide Mn-Na_2WO_4/SiO_2 catalyst have been studied via surface-sensitive techniques, such as XPS and Raman spectroscopy, and bulk-sensitive techniques, such as XRD analysis, EPR, and X-ray absorption (XAS) spectroscopies. Although no consensus has been reached, we can highlight some common insights in the next section.

2.6.1 Proposed active sites and mechanisms for the selective activation of methane on the Mn-Na_2WO_4/SiO_2 catalyst for OCM

FANG *et al.* (1992) published the unprecedented use of Mn-Na_2WO_4/SiO_2 for OCM, reporting a promissory C_2 yield of ~ 23.9% at 800 ºC. The same research group then studied the structure of the supported oxides (*i.e.*, MnO_x, NaO_x, and WO_x) and their interaction with SiO_2 (JIANG *et al.*, 1993). For this purpose, The Na_2WO_4 loading on SiO_2 was increased, keeping Mn loading constant (~ 1.9wt.%). The catalysts were prepared via the incipient-wetness impregnation (IWI) method using $Na_2WO_4{\cdot}xH_2O$, $Mn(NO_3)_2{\cdot}xH_2O$, and amorphous silica gel as precursors. At 1wt.% Na_2WO_4 loading, the XRD pattern displayed only peaks related to the crystalline α-cristobalite phase, whose intensity increased with the Na_2WO_4 loading. At 4wt.% Na_2WO_4 loading, the silica phase transition from amorphous to crystalline α-cristobalite occurred totally,

catalyst surface area decreased drastically (from 140 to 7.4 $m^2\ g^{-1}_{cat}$), and methane conversion was the highest (~ 36.8%). At Na_2WO_4 loadings higher than 4wt.%, the XRD pattern also displayed peaks associated with the crystalline Na_2WO_4 phase, while methane conversion remained almost unchanged. In addition, the W4*f* / Si2*p* peak intensity ratio obtained by XPS increased linearly with the Na_2WO_4 loading up to 4wt.%, and then it continued to increase but with a steeper slope. The authors concluded that Na_2WO_4 was highly dispersed on the silica surface until 4wt.% Na_2WO_4 loading, which corresponded to the monolayer coverage. Higher Na_2WO_4 loadings led to the formation of crystalline Na_2WO_4 particles, which were inactive for OCM. The dispersed active species on the catalyst monolayer would be distorted WO_4 tetrahedra formed by reconstructing the catalyst surface. The authors showed the catalyst surface reconstruction by studying the 5wt.% Na_2WO_4/SiO_2 catalyst via XPS and Raman spectroscopy. The O1s XPS spectrum exhibited two bands at 531.6 and 530.3 eV, which were attributed to W-O-Si and W=O bonds, respectively. Thus, a W atom would form a tetrahedron by binding to three Si atoms (W-O-Si bonds) and one O atom (W=O double bond). Furthermore, Raman spectra exhibited three bands at 1073, 842, and 783 cm^{-1}. The former band was assigned to the terminal W=O double bond, whereas the other two bands were assigned to the W-O-Si bonds (FANG *et al.*, 1992).

In a further publication, WU & LI (1995) studied the molecular structure of distorted WO_4 tetrahedra via Raman spectroscopy and XRD analysis. For this purpose, 3wt.% WO_3/SiO_2, 1.2wt.% Na^+-3wt.% WO_3/SiO_2, and 5wt.% Na_2WO_4/SiO_2 catalysts were prepared. In the absence of Na^+, the WO_3/SiO_2 catalyst (prepared using ammonium para-tungstate, $(NH_4)_6H_2W_{12}O_{40}\cdot nH_2O$) exhibited Raman bands (807, 713, and 271 cm^{-1}) assigned to the crystalline WO_3 phase, with W atom being octahedrally coordinated (O_h-symmetry) to six oxygen atoms. Furthermore, this catalyst did not show diffraction peaks related to the crystalline α-cristobalite phase. Adding 1.2wt.% Na^+ (using $NaNO_3$) before calcination to the 3wt.% WO_3/SiO_2 catalyst led to the appearance of Raman bands (927, 811, 788, 416, 311, and 231 cm^{-1}) assigned to the crystalline Na_2WO_4 phase, with W atom being tetrahedrally coordinated (T_d-symmetry) to four oxygen atoms. However, some of these bands (788, 416, and 231 cm^{-1}) were incorrectly assigned because they are actually related to the crystalline α-cristobalite phase (RICHET & MYSEN, 1999). Finally, the 5wt.% Na_2WO_4/SiO_2 catalyst exhibited similar Raman spectra to the 1.2wt.% Na^+-3wt.% WO_3/SiO_2 catalyst. Thus, Na^+ was proposed to promote the tetrahedral coordination of the W atom and the formation of

the crystalline α-cristobalite phase. Moreover, the structure-activity relationship was established via steady-state OCM catalytic studies. Catalysts containing W atoms with T_d-symmetry (*i.e.*, 1.2wt.% Na^+-3wt.% WO_3/SiO_2 and 5wt.% Na_2WO_4/SiO_2) exhibited a much higher C_2 yield (13% and 16.4%, respectively) than that containing W atoms with O_h-symmetry (1%). Thus, the early literature pointed out distorted WO_4 tetrahedra as the active sites of the Mn-Na_2WO_4/SiO_2 catalyst.

Three mechanisms for the selective methane activation on the Mn-Na_2WO_4/SiO_2 catalyst have received attention in the past years. The first one was proposed by WU *et al.* (1995) based on EPR and Raman spectroscopies measurements. The Mn-Na_2WO_4/SiO_2 catalyst was initially reduced under methane at 800 ºC and then cooled down under vacuum to be reoxidized at different temperatures. The reduced catalyst showed a slightly distorted EPR band assigned to the W^{4+} cation and no typical Raman bands (922, 838, 794, 403, 334, and 311 cm^{-1}) presumably because of the break of W=O bonds, Figure 2.6b. Once the catalyst was reoxidized at 25 ºC, the EPR spectrum showed the disappearance of the band related to W^{4+} species and the appearance of a band at g = 2.0046, which was associated with the presence of F-centers (*i.e.*, an oxygen vacancy with two trapped electrons), Figure 2.6c. After reoxidation at 80 ºC, the band at g = 2.0046 disappeared, suggesting that gas-phase oxygen was activated on the F-center to produce lattice oxygen, Figure 2.6a. Furthermore, three Raman bands (not specified) were detected and assigned to the crystalline Na_2WO_4 phase, indicating the restoring of W=O bonds and the completion of the redox cycle. Thus, the methane activation was proposed to occur at lattice oxygen of distorted WO_4 tetrahedra following a $W^{6+} \leftrightarrow W^{4+}$ redox mechanism, while gas-phase oxygen completes the cycle.

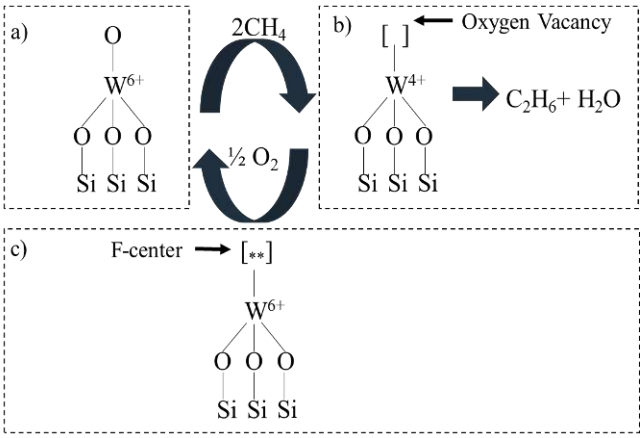

Figure 2.6 Proposed redox mechanism for the selective methane activation on the Mn_2O_3–Na_2WO_4/SiO_2 catalyst for OCM. Reprinted (adapted) from WU et al. (1995). Copyright (2021), with permission from Elsevier.

The mechanism proposed for WU *et al.* (1995), however, has been questioned. Firstly, considering that EPR spectroscopy cannot detect W^{4+} sites because they are not paramagnetic, the arbitrary assignment of the broad EPR band to W^{4+} sites is inappropriate. Secondly, the thermal stability of F-centers, and therefore, its presence at real OCM reaction temperatures, is questionable (ARNDT *et al.*, 2012). Finally, the disappearance of all the Raman bands would not be associated with a reduction of the W sites because the Raman bands related to the crystalline α-cristobalite phase should remain unaltered.

The second mechanism for the selective methane activation on the Mn-Na_2WO_4/SiO_2 catalyst was proposed by JIANG *et al.* (1997), Figure 2.7. According to this mechanism, methane activation occurs in parallel with gas-phase oxygen activation. Methane would heterolytically activate on distorted WO_4 tetrahedron (W^{6+}), with the carbanion (CH_3^-) binding to W^{6+} cation and the proton (H^+) binding to lattice oxygen, Figure 2.7a. The W^{6+} cation would reduce to W^{5+} to release a methyl radical ($CH_3^{\bullet}$) to the gas phase and then reoxidizes by transferring an electron to Mn^{3+}. The resulting Mn^{2+} cation would reoxidize to Mn^{3+} in the presence of gas-phase oxygen, thus completing the redox cycle, Figure 2.7b. Oxygen spillover in the opposite direction of the electron transfer was proposed to be responsible for supply active oxygen species to distorted WO_4 tetrahedra. Thus, methane would activate following a $W^{6+} \leftrightarrow W^{4+}$ redox cycle, while gas-phase oxygen activates following an $Mn^{3+} \leftrightarrow Mn^{2+}$. Methane activation mechanisms on the Mn-Na_2WO_4/SiO_2 catalyst considering two active metal sites have also been recently proposed in the literature (FLEISCHER *et al.*, 2018, WANG *et al.*, 2017).

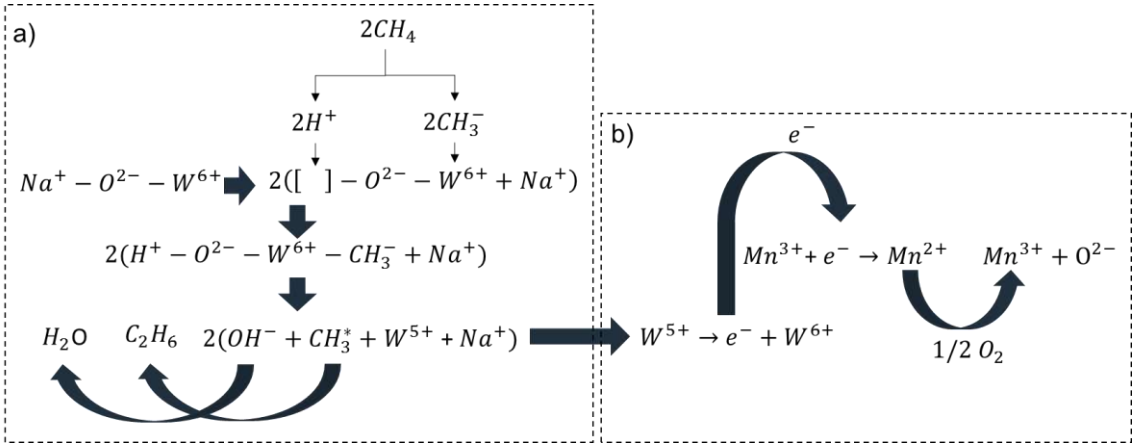

Figure 2.7 Proposed redox mechanism considering two active metal sites for the activation of methane and gas-phase oxygen on the Mn–Na_2WO_4/SiO_2 catalyst for OCM.

The third mechanism for the methane activation on the Mn-Na_2WO_4/SiO_2 catalyst was proposed by WANG *et al.* (1995). Interestingly, the authors did not consider the presence of distorted WO_4 tetrahedra as active sites. They investigated three different catalyst formulations: Mn-Na_2WO_4/SiO_2, Mn-Na_2WO_4/MgO, and $NaMnO_4$/MgO, in a co-fed flow system and a pulse reactor. Because all catalysts presented similar OCM performance, the authors concluded that the methane activation proceeds via the same mechanism on the Mn-O-Na sites. The mechanism considers that gas-phase oxygen is initially activated via dissociative adsorption to form Mn-O-Na$^{\cdots}$O$^{\bullet}$ sites. Methane is then activated by cleaving the C-H bond on these sites. Moreover, the presence of a common active site was consistent with the similar activation energy of methane calculated on the Mn-Na_2WO_4/SiO_2 and Mn/Na_2WO_4/MgO catalysts (*i.e.*, ~ 280 and ~268 kJ mol^{-1}, respectively) (PAK *et al.*, 1998b). However, ELKINS *et al.* (2015) recently reported that the Mn-Na_2WO_4/MgO catalyst exhibited a C_2 yield (3.2%) markedly lower than the Mn-Na_2WO_4/SiO_2 catalyst (18.5%) at 800 ºC. The authors attributed the poor OCM performance of the MgO-supported catalyst to the impossibility of stabilizing the crystalline Na_2WO_4 phase, which would be required to activate methane.

5.6.2 The proposed role of Na

Although the monometallic oxide Na/SiO_2 catalyst is inactive and unselective for OCM, adding Mn and W metals creates a synergistic promoting effect, as shown in Table 2.2. Considering the interactions of the Na-Mn, Na-W, and Na-Mn-W systems, the literature has assigned a large set of roles for Na. In this regard, Na has been proposed to introduce basic sites, allowing the activation of methane on the proposed Mn-O-Na active sites (PAK *et al.*, 1998a, WANG *et al.*, 1995). The Na-promoted Mn/SiO_2 catalyst with increased C_2 selectivity has been extensively informed in the literature (JONES *et al.*, 1987, JI *et al.*, 2002). Here, Na offered a higher promoting effect than other alkali metals (Li, K, Rb, and Cs), alkaline-earth metals (Mg, Ca, Sr, and Ba), or lanthanum (La) atom (JONES *et al.*, 1987). Moreover, Na has been proposed to accelerate the formation of the crystalline α-cristobalite phase during catalyst calcination (WU & LI, 1995). MAZZARA *et al.* (2000) studied the role of Na in the crystallization of amorphous silica via XAS at the Na-K edge. The authors observed that once Na atoms diffused into the amorphous silica network (even at room

temperature), the length of the Si-O bonds relaxed around them, cleaving the siloxane bridges (Si-O-Si) bonds. Thus, the Na presence leads to the formation of nonbridging oxygen bonds, such as Si-O-Na and Na-O-Si, which are typically present in crystalline silica phases. However, the silica phase transition has also been observed for other silica-supported alkali oxides (K, Rb, and Cs) but with negligible activity for OCM (PALERMO *et al.,* 2000). Thus, only the presence of the α-cristobalite phase does not ensure a good OCM performance.

The role of Na has also been associated with the transformation of the W sites symmetry and the distortion of WO_4 tetrahedra. As discussed before, adding 1.2wt.% Na^+ (using $NaNO_3$) before calcination into the 3wt.% WO_3/SiO_2 catalyst made W atoms exhibit T_d-symmetry on the 1.2wt.% Na^+-3wt.% WO_3/SiO_2 catalyst (WU & LI, 1995). This featuring was also observed for silica-supported dispersed WO_x phases. KIANI *et al.* (2020) prepared a series of Na-WO_x/SiO_2 catalysts with different Na/W molar ratios using various Na- and W-precursors. Adding Na imposed distortion progressively on the W atoms with T_d-symmetry for Na/W molar ratios below 1.6. The catalyst with a Na/W molar ratio of 1.6 exhibited only dispersed Na-WO_4 phase without the formation of α-cristobalite phase. Finally, the catalyst with a Na/W molar ratio of 2 that mimics the stoichiometry of the Na_2WO_4 crystals (irrespective of the precursor choice) exhibited both dispersed Na-WO_4 and crystalline Na_2WO_4 phases along with the formation of the α-cristobalite phase. Dispersed Na-WO_4 species were found to be more geometrically distorted, less basic, and more reducible than the crystalline Na_2WO_4 phase. Furthermore, catalysts only containing Na-WO_4 species (retaining the amorphous silica phase) were more selective to C_2 hydrocarbons. Thus, the presence of the crystalline α-cristobalite and Na_2WO_4 phases may not be relevant for OCM.

The role of the Na has also been associated with the surface composition of W and Mn atoms. JI *et al.* (2002) used a series of trimetallic Xwt.% Na-3.1wt.% W-2wt.% Mn/SiO_2 catalysts ($0 \leq X \leq 7.8$wt. %). The maximum near-surface composition of W (0.8%) and Mn (3.1%) and C_2 yield (19.2%) was observed at X= 1.6wt. %. Higher Na loadings led to a decrease in the near-surface composition of W and Mn atoms while the catalyst surface was mainly covered by Na atoms. Moreover, the substitution of Na in the supported trimetallic X-W-Mn/SiO_2 catalyst (X = Li, Na, K, Ba, Ca, Fe, Co, Ni, or Al) showed that although distorted WO_4 tetrahedra were formed on Li-, Na-, K-, and Ba-promoted catalysts, they were stable only on Na- and K-promoted catalysts, presumably because of the presence of α-cristobalite support (JI *et al.*, 2003).

2.6.3 The proposed role of Mn

Methane activation mechanisms considering two active metal sites have proposed the redox properties of Mn atom to be crucial for the OCM performance of the Mn-Na_2WO_4/SiO_2 catalyst (FLEISCHER *et al.*, 2018, JIANG *et al.*, 1997, LI *et al.*, 2001, WANG *et al.*, 2017a, WANG *et al.*, 2017b). STOBBE *et al.* (1999) studied the redox properties of bulk MnO_x oxides (MnO_2, Mn_2O_3, and Mn_3O_4) using cycles of methane temperature-programmed reduction (CH_4-TPR) and reoxidation. The onset temperature of reduction was determinate by the crystallinity degree of the MnO_x oxides rather than their initial oxidation state. The lowest the crystallinity degree, the lowest onset temperature of reduction. However, subsequent cycles of reduction with methane at 800 ºC and reoxidation at 550 ºC increased the onset temperature of reduction, compromising the oxygen release capacity of these systems. Finally, the authors suggested that using thermostable supports can influence the particle size and crystallinity of supported MnO_x oxides, thus increasing their reducibility. ARENA *et al.* (2001) showed that the onset temperature of reduction for MnO_x oxides decreased after being supported as follows: MnO_x/ZrO_2 (100 ºC) < MnO_x/Al_2O_3 (152 ºC) < MnO_x/TiO_2 (160 ºC) < MnO_x/SiO_2 (202 ºC) ~ MnO_2 (202 ºC) < Mn_2O_3 (250 ºC). This effect was ascribed to the oxide-support interaction, which also controlled the dispersion and the final oxidation state of the cation.

The oxygen release temperature is a critical property of the Mn-Na_2WO_4/SiO_2 catalyst for OCM. GORDIENKO *et al.* (2016) recently showed that gas-phase oxygen can adsorb either weakly or strongly on the catalyst surface, and the adsorption strength is related to the selective activation of methane. Using oxygen temperature-programmed desorption (O_2-TPD) and thermal gravimetric analysis coupled with mass spectrometry (TGA-MS) techniques, the authors observed that strongly and weakly adsorbed oxygen was available to react with methane at high and low temperatures, respectively. The weakly adsorbed oxygen was associated with the selective production of C_2 hydrocarbons, while strongly adsorbed oxygen was associated with the formation of deep oxidation compounds (CO_x). Furthermore, FLEISCHER *et al.* (2016) used temperature-programmed surface reaction (TPSR), O_2-TPD, and both kinetic and thermodynamic calculations to associate the adsorption strength of gas-phase oxygen with its electronic nature. Here, the activation of gas-phase oxygen on the catalyst surface follows a two-step mechanism, starting with the weak adsorption of molecular

species followed by the strong adsorption of dissociated species. In the absence of gas-phase oxygen, weakly adsorbed electrophilic oxygen is responsible for produce C_2 hydrocarbons, while strongly adsorbed nucleophilic oxygen is responsible for CO_x.

The role of Mn has also been related to the molecular and electronic structure of MnO_x species. KOU *et al.* (1998) used XAS at Mn-K and W-$L_{1,3}$ edges and XPS to study fresh and used (100 and 450 h on stream) samples of the Mn-Na_2WO_4/SiO_2 catalyst. The fresh sample contained WO_4 (T_d-symmetry) and MnO_6 (O_h-symmetry) groups. The measured average bond length was 1.77 Å for W-O and 2.00 Å for Mn-O, which are identical to crystalline Na_2WO_4 (W^{6+}) and Mn_2O_3 (Mn^{3+}) phases. The catalyst deactivation evidenced after 450 h was associated with the disappearance of the WO_4 (T_d-symmetry) tetrahedra and the formation of tetrahedrally coordinated Mn^{2+} (T_d-symmetry) groups. The reduction of the Mn cation was also confirmed by XPS, which exhibited an increase in the binding energy (from 641.4 eV of Mn^{3+} to 641.7 eV of Mn^{2+}). Therefore, the authors concluded that for the Mn-Na_2WO_4/SiO_2 catalyst to be active and selective for OCM, two cationic groups with variable oxidation states and site-symmetries, W^{6+} (T_d-symmetry) and Mn^{3+} (O_h-symmetry), are needed. Thus, methane activation takes place on T_d -WO_4 groups, while the gas-phase oxygen activation takes place on O_h –Mn_2O_3, as follows:

$$O_h\text{-}Mn^{3+} \leftrightarrow D_{4h}\text{-}Mn^{2+} \,/\, Mn^{3+} \leftrightarrow T_d\text{-}Mn^{2+} \qquad (2.16)$$

The values of methane conversion and C_2 selectivity, unfortunately, were not informed in this work, and therefore, there is no evidence to propose a structure-activity/selectivity relationship. Finally, the Mn loading affects the formation of both WO_4 tetrahedral sites and the crystalline Mn_2O_3. JI *et al.* (2002) used a series of supported 0.8wt.% Na-3.1wt.% W-Zwt.% Mn/SiO_2 ($0 \leq Z \leq 24.0$wt. %) catalysts. The maximum C_2 yield (19.1%) was observed at Z = 1wt. % in the presence of the Mn_2O_3 and Na_2WO_4 phases. For Mn loadings higher than 6wt. %, the C_2 yield decreased, Raman bands related to WO_4 tetrahedral sites disappeared, and XRD peaks related to the $Na_2W_2O_7$ and $MnMn_6SiO_{12}$ phases emerged. Moreover, the substitution of Mn atoms in the trimetallic Na-W-Z/SiO_2 catalyst (Z = V, Cr, Fe, and Ce) was also explored (GHOLIPOUR *et al.*, 2010, MALEKZADEH *et al.*, 2001). Only the Ce-promoted Na-W/SiO_2 catalyst exhibited comparable OCM performance with the conventional Mn-Na_2WO_4/SiO_2 catalyst, apparently because of the CeO_2 oxygen storage capacity.

2.6.4 The proposed role of W

The molecular and electronic structure of the W atoms has been proposed to play a critical role in the OCM performance of the Mn-Na_2WO_4/SiO_2 catalyst. W atoms with distorted T_d-symmetry (WO_4 tetrahedra) have been associated with the selective production of C_2 hydrocarbons, while W atoms with O_h-symmetry have been associated with the formation of undesirable deep oxidation compounds (CO_x) (KIANI *et al.*, 2020, WU & LI, 1995). Moreover, JI *et al.* (2002) studied the W loading effect on the Mn-Na_2WO_4/SiO_2 catalyst using a series of trimetallic 0.8wt.% Na-Ywt.% W-2wt.% Mn/SiO_2 catalysts ($0 \leq Y \leq 17.8$wt. %). The maximum C_2 yield (~ 18.5%) was observed at Y= 3.1-4.5wt.% in the presence of crystalline Mn_2O_3, $Na_2W_2O_7$, and Na_2WO_4 phases. For W loadings higher than 4.5wt.%, the C_2 yield decreased and XRD peaks of crystalline Mn_2O_3, $Na_2W_2O_7$, and $MnMn_6SiO_{12}$ phases disappeared. Only XRD peaks of the crystalline $MnWO_4$ and Na_2WO_4 phases were observed for Y > 4.5wt.%. Moreover, the substitution of W on the trimetallic Na-Y-Mn/SiO_2 catalyst (Y = W, Mo, Nb, V, or Cr) was explored at 775 ºC and 1 bar with a gas hourly space velocity (GHSV) of 8963 h^{-1} of $CH_4:O_2:N_2$ = 2:1:2 (MAHMOODI *et al.*, 2010). Although the methane conversion remained almost unchanged (32-40%), the C_2 selectivity decreased as follows: W (39.6%) > Mo (37.2%) > Nb (33.2%) > Cr (11.5%) > V (8.0%).

2.6.5 The proposed role of SiO_2 support

As shown in Table 2.2, although amorphous silica is a deep oxidation catalyst, both Mn-Na_2WO_4/SiO_2 and Na_2WO_4/SiO_2 catalysts are active and selective OCM catalysts presumably due to the presence of the crystalline α-cristobalite phase. However, only the presence of the crystalline α-cristobalite phase does not ensure a good OCM performance, since neither Na/SiO_2 nor Mn-Na_2WO_4/α-cristobalite (prepared using α-cristobalite as support precursor) exhibit relevant C_2 yields. Thus, the Na-induced silica phase transition from amorphous to the crystalline α-cristobalite phase during catalyst calcination (at ~ 800 ºC) has been proposed to be critical for stabilizing active sites. The unusual low-temperature silica crystallization occurs in parallel with the collapse of the porous structure of the amorphous silica. Thus, the high surface area of amorphous silica (~ 400 $m^2\ g^{-1}$) drastically decreases (< 10 $m^2\ g^{-1}$) after being coated with Mn-Na-W precursors and calcined (ELKINS & HAGELIN-

WEAVER, 2015, GODINI *et al.*, 2014, JI *et al.*, 2002, MAZZARA *et al.*, 2000, PAK & LUNSFORD, 1998, SIMON *et al.*, 2011, WANG, D.J. *et al.*, 1995, WANG, Huan *et al.*, 2017, WANG, Jiaxin *et al.*, 2006, YILDIZ AKSU *et al.*, 2014).

Several works have attempted to improve the conventional trimetallic catalyst formulation by substituting amorphous silica for other silica materials and oxides or changing the silica properties by doping with a foreign atom. Regarding the substitution of conventional amorphous silica, the use of SiC monolithic foam and ordered mesoporous SBA-15 silica supports were explored to offer a higher specific surface area for the Mn-Na-W phases (LIU YANG *et al.*, 2008, YILDIZ AKSU *et al.*, 2014). However, the increased C_2 yield observed for these systems was related to an enrichment of Mn-Na-W species on the catalyst surface rather than a higher specific surface area. Indeed, the SBA-15 and SiC materials allowed the homogeneous dispersion of Mn-Na-W phases, while the SiC monolithic foam avoided the hot spot formation, which is responsible for the deep oxidation of methane (LIU YANG *et al.*, 2008, YILDIZ *et al.*, 2016).

Changing silica for a reducible or nonreducible oxide as support was also investigated. YU *et al.* (1995) compared the OCM performance of a series of REOs-supported Na_2WO_4 catalysts (REOs= La_2O_3, CeO_2, Pr_6O_{11}, Nd_2O_3, Sm_2O_3, Dy_2O_3, and Yb_2O_3) with that of the silica-supported Na_2WO_4 catalyst. The authors showed that CeO_2 and Pr_6O_{11}, which are known as deep oxidation materials, become reasonably active and selective OCM catalysts after being promoted with Na_2WO_4. In addition, YILDIZ *et al.* (2014) tested a series of MO-supported Mn-Na_2WO_4 catalysts (MO = La_2O_3, CaO, Al_2O_3, ZrO_2, SiO_2, SiC, MgO, Fe_2O_3, Fe_3O_4, SrO, TiO_2-rutile, and TiO_2-anatase) under identical OCM reaction conditions in a parallel reactor. SiC-, TiO_2-, and Fe_2O_3-supported Mn-Na-W catalysts showed similar OCM performances to the conventional silica-supported Mn-Na_2WO_4/SiO_2 catalyst. Regarding the change of the electronic properties of silica by doping with a foreign cation, YUNARTI *et al.* (2017) recently evaluated a series of Mg-Ti-doped silica-supported Mn-Na_2WO_4 catalysts for OCM. The Mn-$Na_2WO_4/Mg_{0.05}Ti_{0.05}Si_{0.90}O_{2-n}$ catalyst exhibited a C_2 yield of 23.1%, while the conventional Mn-Na_2WO_4/SiO_2 catalyst exhibited 17.1% (at 800 ºC; CH_4:O_2 = 3:1 (mol/mol); GHSV = 10,000 h^{-1}). The authors attributed the enhanced C_2 yield to the enrichment of catalyst surface with Na/W/Mn compounds due to the insertion of both Mg and Ti atoms into the crystalline α-cristobalite framework.

To summarize, neither the nature of the active sites nor the individual role of each supported oxide on the Mn-Na_2WO_4/SiO_2 catalyst is still clear in the literature. The literature has proposed that methane activation takes place at either Mn-O-Na or distorted WO_4 tetrahedra, with gas-phase oxygen activation taking place on the Mn^{3+} sites, in the crystalline Mn_2O_3 phase. The presence of distorted tetrahedral WO_4 sites has been associated with the identification of the crystalline Na_2WO_4 phase, which would be stabilized on the catalyst surface because of the Na-induced silica phase transition from amorphous to α-cristobalite. Thus, Na_2WO_4, Mn_2O_3, and α-cristobalite have been proposed to be active phases for OCM. However, recent *in situ/operando* studies have shown that typical high OCM temperatures and reagents flow induce structural changes in the catalyst. In this sense, the association of any catalytic performance with only crystalline phases observed at room temperature may not be adequate.

2.6.6 The dynamic structure of the Mn-Na_2WO_4/SiO_2 catalyst

Although Mn-Na_2WO_4/SiO_2 is a promising catalyst, the industrial deployment of the OCM route requires even more selective catalysts. Elucidating the nature of the active sites on the Mn-Na_2WO_4/SiO_2 catalyst and their structure-activity/selectivity relationship is crucial to rationalize the design of improved formulations. As discussed before, over the past few decades, hundreds of works have proposed active sites, selective methane activation mechanisms, and roles for each supported oxide, but mainly based on *ex situ* experimental evidence. This is a critical issue because recent studies have shown that the Mn-Na_2WO_4/SiO_2 catalyst is a highly dynamic system: high OCM temperatures and reagents flow induce important changes in the catalyst structure (KIANI *et al.*, 2019).

Regarding the temperature-induced structural changes, the proposed active crystalline Na_2WO_4 and α-cristobalite phases identified at room temperature undergo transitions at heating, as evidenced by differential thermal analysis (DTA) (SIMON *et al.*, 2011), differential scanning calorimetry (DSC) (SADJADI *et al.*, 2015), high energy X-ray diffraction computed tomography (XRD-CT) (VAMVAKEROS, A. *et al.*, 2015b, VAMVAKEROS *et al.*, 2020c), and Raman spectroscopy (KIANI *et al.*, 2020). The reversible $\alpha \leftrightarrow \beta$-cristobalite phase transition was observed by DSC through the formation of an endothermic peak at 232 ºC (heating curve) and an exothermic peak at

222 ºC (cooling curve) (SADJADI *et al.*, 2015). In addition, the melting and resolidification transitions of the crystalline Na_2WO_4 phase were observed through the formation of an endothermic peak at 680 ºC (heating curve) and an exothermic peak at 657 ºC (cooling curve) (SADJADI *et al.*, 2015). Therefore, the crystalline phases identified at room temperature cannot be associated with any activity/selectivity for OCM, which occurs at temperatures above 650 ºC.

Regarding the reagents-induced structural changes, the high mobility of Na^+ and WO_4^{2-} ions in the molten Na_2WO_4 phase leads to structural changes once methane is admitted into the reactor (SINEV *et al.*, 2019, VAMVAKEROS *et al.*, 2015a). Indeed, Mn^{3+} species present on the crystalline Mn_2O_3 phase interact with WO_4^{2-} ions, reducing and forming the crystalline $MnWO_4$ phase (VAMVAKEROS *et al.*, 2020). In this phase, Mn ions have an oxidation state of 2+ and W atoms have an O_h-symmetry. Thus, neither W atoms with T_d-symmetry nor Mn^{3+} sites would be not present during the steady-state OCM operation of the Mn-Na_2WO_4/SiO_2 catalyst, making the proposed mechanism for methane activation lacking experimental evidence.

Although fast-developing *in situ*/*operando* studies have brought new insights about the catalyst structure at real OCM reaction conditions, new studies are required to fully understand the nature of the active sites and their structure-activity/selectivity relationship. In this regard, the catalyst structure should be characterized using not only bulk- (XRD, XAS, XPS) but also surface-sensitive (Raman spectroscopy) techniques at *in situ* and *operando* conditions. Indeed, identifying active species only by XRD at ambient conditions is inadequate because it is limited to the observation of crystalline phases, being unable to report the potential presence of other structures such as molecularly dispersed, amorphous, and/or molten phases. Furthermore, XRD is unable to characterize the W sites structure at relevant OCM reaction temperatures (> 700 ºC) because of the Na_2WO_4 melting. Therefore, further studies should elucidate: *i*) the electronic and molecular structure of the Mn and W sites at real OCM reaction temperatures, inspecting their oxidation state, site symmetry, and distortion degree that may change at heating, *ii*) the relevance of the $MnWO_4$ phase at steady-state OCM operation, and *iii*) the nature of the lattice oxygen W and Mn oxides for the selective methane activation.

Chapter 3

"*If I have a thousand ideas a year, and only one turns out to be good, I am satisfied*" – Alfred Nobel

Methodology

3.1 Catalyst synthesis

The conventional 2wt.% Mn-5wt.% Na_2WO_4/SiO_2 catalyst was synthesized via incipient-wetness impregnation (IWI), which is the most widely used method for synthesizing this catalyst in works discussing the nature of its active sites (ES & HAGELIN-WEAVER, 2015, FANG *et al.*, 1992, JIANG *et al.*, 1997, 1993, KIANI *et al.*, 2019, WANG *et al.*, 1995, WU & LI, 1995, WU *et al.*, 1995). The catalyst precursors were those described in such works to minimize variations in the nature and dispersion of the supported phases (ARNDT *et al.*, 2012, KIANI *et al.*, 2019, WANG, Jiaxin *et al.*, 2006). The catalyst was synthesized by dissolving $Na_2WO_4 \cdot 2H_2O$ (Sigma-Aldrich, ACS reagent, ≥99%) and $Mn(NO_3)_2 \cdot 4H_2O$ (Sigma-Aldrich, ACS reagent, ≥97%) in a volume of deionized water equal to the pore volume (1.1 $cm^3\ g^{-1}$) of the silica support (Davisil Grade 646, 35-60 mesh, BET surface area = 401 $m^2\ g^{-1}$). The resulting solution was then added onto the silica under continuous stirring until the onset of incipient wetness. Finally, the sample was dried at 110 ºC overnight and then calcined at 800 ºC (1 ºC min^{-1}) for 5 h in a muffle furnace in static air. Additionally, Mn-free 5wt.% Na_2WO_4/SiO_2 and Mn- and Na-free 3.1wt.% WO_3/SiO_2 catalysts were synthesized by the same IWI method for comparison, mimicking W loading on the conventional Mn-Na_2WO_4/SiO_2 catalyst (~ 3.1 wt.%). The Na_2WO_4/SiO_2 catalyst was synthesized using the same precursors as for the Mn-Na_2WO_4/SiO_2 catalyst, while $(NH_4)_6H_2W_{12}O_{40} \cdot nH_2O$, ammonium meta tungstate (AMT, Sigma-Aldrich, ACS reagent, ≥99.99%), was used as W precursor for the WO_3/SiO_2 catalyst, in agreement with WU & LI (1995). All catalysts were synthesized at the Núcleo de Catálise (NUCAT/COPPE/UFRJ, Rio de Janeiro, Brazil).

3.2 Catalyst characterization

3.2.1 Inductively Coupled Plasma Optical Emission Spectroscopy (ICP-OES)

Elemental analysis via ICP-OES was performed using a PlasmaQuant® PQ 9000 spectrometer (Analytik Jena) at the Institute of Catalysis and Petrochemistry (ICP/CSIC, Madrid, Spain) to ensure that the nominal weight loadings of supported metals (*i.e.*, Mn, Na, and W cations) on the Mn-Na_2WO_4/SiO_2, Na_2WO_4/SiO_2, and WO_3/SiO_2 catalysts corresponds to the conventional 2 wt.% Mn-5 wt.% Na_2WO_4/SiO_2 catalyst. Sample preparation was conducted by adding 10 mg of LiF to 10 mg of each catalyst. The mixture was then dissolved into 10 ml HNO_3 (65%) and heated to 220 °C for 2 h at 45000 mmHg in a microwave furnace (Multiwave 3000 Anton Paar). The resulting solution was filled up to 50 ml with ultra-pure water and diluted again by a factor of ten for analysis.

3.2.2 Ultraviolet-Visible (UV-vis) Spectroscopy

The UV-vis spectra were taken using a Varian Cary 5000 UV-Vis-NIR spectrophotometer at the ICP/CSIC. Typically, 20 mg of each catalyst in finely ground powder form was loaded into an *in situ* environmental cell (Praying Mantis). The spectra were collected in the 200-800 nm range at ambient conditions using a scan rate of 15 nm min^{-1} and a signal averaging time of 0.5 s. The Kubelka-Munk function $F(R\infty)$ was calculated from the absorbance of the UV-vis spectra.

3.2.3 N_2 Physisorption Experiments

The specific surface area was calculated via N_2 physisorption experiments using an ASAP 2020 (Micromeritics ®) instrument at liquid N_2 temperature (~ -196 ºC) at the NUCAT/COPPE/UFRJ. Typically, 500 mg of each catalyst was outgassed at 300 ºC (10 ºC min^{-1}) under vacuum (1.10^{-6} mmHg) for 24 h before the adsorption experiment. The adsorption and desorption isotherms were obtained by plotting the amount of N_2 assimilated by the catalyst as a function of the partial pressure of N_2. The specific surface areas were calculated using the multiple-point Brunauer-Emmett-Teller (BET) method to analyze the N_2 adsorption isotherms in a relative pressure range of 0.05-0.30. All data treatments were performed using the ASAP 2020 Plus V2.00 software package.

3.2.4 X-ray Powder Diffraction (XRD)

The crystalline structure was studied via XRD analysis using a PANalytical X'Pert Pro diffractometer with Ni-filtered CuK_α radiation (λ = 1.5406 Å) generated at 40 kV and 30 mA at the ICP/CSIC. A high-temperature chamber (Anton Paar XRK900) was used for the *in situ* measurements. Crystalline phases were qualitatively identified using the MDI Jade v.5.0.37 (SP1) software by matching the catalyst XRD patterns against the JCPDS (Joint Committee on Powder Diffraction Standards) database.

Room temperature (RT) XRD patterns were collected at ambient conditions in a Bragg angle (2θ) range of 5 - 90° with a step size of 0.02° and a counting time of 50 s per step. For the *in situ* temperature-programmed oxidation (TPO) XRD analysis, each catalyst was heated stepwise from 25 ºC to 800 ºC (10 ºC min^{-1}) under 20% O_2/Ar (50 cm^3 min^{-1}). The *in situ* TPO-XRD patterns were isothermally collected at 25, 50 ºC, and then each 50 ºC until 800 ºC. Measurements conditions were: 2θ range of 5-90°, step size of 0.05°, and counting time of 20 s per step.

3.2.5 Temperature-Programmed Reduction (TPR) studies

For the TPR coupled to mass spectrometry (MS) experiments were used H_2 and CH_4 as chemical probing molecules to measure the amount and reactivity of the lattice oxygen, respectively. Typically, 50 mg of each catalyst was loaded into a U-shape reactor tube (I.D. = 10 mm) between two pieces of quartz wool. The catalyst samples were initially dehydrated under 5% O_2/Ar (50 cm^3 min^{-1}) at 400 °C for 30 min and then cooled down to 100 °C. The H_2-TPR-MS experiments were performed by heating the dehydrated catalysts from 100 to 1000 °C (10 ºC min^{-1}) under H_2 (50 cm^3 min^{-1}). Gaseous effluent was simultaneously recorded with an *online* mass spectrometer (Dymaxicon Dycor, DME200MS). The spectra were normalized against catalyst weight for comparison. The reduction profile was obtained from the *m/z* = 18 (H_2O) signal, which was integrated to calculate the lattice oxygen using calibration curves adjusted from the reduction of a sample pattern (CuO) with the known oxidation state.

The CH_4-TPR-MS experiments were performed by heating the dehydrated catalysts from 100 to 1000 °C (10 ºC min^{-1}) under 10% CH_4/He (50 cm^3 min^{-1}). Before the CH_4-TPR-MS tests, the catalysts were flushed with He (50 cm^3 min^{-1}) at 100 ºC for 30 min. For detection of gases, the following *m/z* values were used: *m/z* = 16 (CH_4), *m/z* = 30 (C_2H_6), *m/z* = 27 (C_2H_4), *m/z* = 28 (CO), and *m/z* = 44 (CO_2).

3.2.6 Raman Spectroscopy

The identification of species by XRD is limited to the observation of crystalline phases, being unable to report molecularly dispersed, amorphous, or molten phases. Fortunately, Raman spectroscopy is sensitive to such species. Raman spectra were taken using a confocal Renishaw inVia Qontor instrument equipped with a liquid N_2-cooled CCD detector and three laser excitations (785, 514, and 405 nm) at the ICP/CSIC. The 405 nm laser was chosen to register Raman spectra at high temperatures. The spectral resolution was near 1.5 cm^{-1}, and the wavenumber calibration was checked using the silica standard band at 520.5 cm^{-1}. The laser was focused on the catalysts with a confocal microscope using an ultralong working distance x20 objective (Olympus LMPlanFL N 20X). Typically, ~ 0.05 g of each catalyst (180 - 250 μm) was loaded into a Linkam reaction cell that consists of a fixed-bed microreactor with a quartz window and O-ring seals, which was cooled by flowing water. The laser power on the catalyst was kept below 5 mW to prevent local heating. The spectra were analyzed using PEAXACT software. Before collecting Raman spectra, each catalyst was dehydrated under 50 cm^3 min^{-1} of O_2:Ar (molar ratio 1:2) at 200 ºC (10 ºC min^{-1}) for 30 min and then cooled down to 25 ºC under the same oxidizing flow.

In situ TPO-Raman spectra of the dehydrated catalysts were collected at heating to 800 ºC (10 ºC min^{-1}) every 25 ºC (1 accumulation of 20 s) under 50 cm^3 min^{-1} of an oxidizing flow (O_2:Ar = 1:2). The TPO-Raman study mimics the heating process typically used in the literature for testing the steady-state OCM performance of the conventional Mn-Na_2WO_4/SiO_2 catalyst (PALERMO *et al.*, 1998, PALERMO *et al.*, 2000, WANG *et al.*, 1995).

Operando temperature-programmed reaction (TPRX) Raman spectra of the dehydrated catalysts were collected at heating to 800 ºC (10 ºC min^{-1}) every 25 ºC (1 accumulation of 20 s) under 50 cm^3 min^{-1} of an OCM gas mixture (CH_4:O_2:Ar = 2:1:4). The gaseous products were simultaneously analyzed *online* with a mass spectrometer (Dymaxicon Dycor, DME200MS). For detection of gases, the following *m/z* values were used: *m/z* = 16 (CH_4), *m/z* = 30 (C_2H_6), *m/z* = 27 (C_2H_4), *m/z* = 28 (CO), and *m/z* = 44 (CO_2).

3.2.7 X-ray Absorption Near-Edge Structure (XANES) Spectroscopy

The electronic structure of the W and Mn sites was monitored by XANES spectroscopy because their redox behavior may participate in the selective activation of methane (*i.e.*, the rate-determining step of the OCM route). XANES spectra at the W-L_3 and Mn-K edges were performed at the XAFS2 beamline at the Brazilian Synchrotron Light Laboratory (LNLS, Campinas, Brazil), using ionization chambers to measure incident and transmitted beam intensities (FIGUEROA *et al.*, 2016). A third ionization chamber was used for energy calibration purposes, measuring a reference (Ga foil or Mn foil, depending on the edge) simultaneously to the catalyst. The XANES spectra at W-L_3 and Mn-K edges were collected in transmission and fluorescence modes, respectively. Each catalyst was loaded in a quartz capillary cell (I.D./O.D.= 0.1/0.2 mm) using a previously reported system (FIGUEROA *et al.*, 2013). Bulk WO_3 (Sigma-Aldrich, 99.995%), Na_2WO_4 (Sigma-Aldrich, 99.995%), WO_2 (Sigma-Aldrich, 99.995%), MnO (Sigma-Aldrich, 99.9%), Mn_3O_4 (Sigma-Aldrich, >99%), Mn_2O_3 (Sigma-Aldrich, 99.99%), and MnO_2 (Sigma-Aldrich, >99%) reference materials were diluted with boron nitride to have a metal loading of 1 - 5 wt.% and measured at ambient conditions. Data processing and analysis were conducted using Athena software (RAVEL & NEWVILLE, 2005).

In situ TPO-XANES spectra were collected by heating each catalyst from 25 to 800 ºC (10 ºC min^{-1}) under 10 cm^3 min^{-1} of 10% O_2/He. *In situ* TPO-XANES spectra at the Mn-K edge were isothermally collected at 25 ºC and then every 100 ºC from 100 ºC up to 800 ºC, while *in situ* TPO-XANES spectra at the W-L_3 were collected at 25, 700, 750, and 800 ºC.

Operando XANES spectra were collected by subjecting each catalyst to a four-step experiment as follows: *i*) heating up to 700 ºC (10 ºC min^{-1}) under an oxidizing flow (10 cm^3 min^{-1} of 10% O_2/He), *ii*) flushing with He (10 cm^3 min^{-1}) for 5 min, *iii*) performing CH_4-XANES by switching to a reducing flow (10 cm^3 min^{-1} of 10% CH_4/He) for 30 min, and *iv*) switching again to the initial oxidizing flow to heating up to the next desired temperature (750 and 800 ºC). Finally, *operando* (CH_4 + O_2)-XANES spectra were also recorded at steady-state OCM operation at 800 ºC after 30 min under an OCM mixture (20 cm^3 min^{-1} of 10% CH_4/He and 10 cm^3 min^{-1} of 10% O_2/He).

3.3 Steady-state OCM Catalytic Tests

Steady-state reaction studies were performed in a fixed-bed catalytic reactor. Typically, 0.1 g of each catalyst (180 – 250 μm) was diluted with 0.4 g of carborundum (SiC, 180–250 μm, Sigma-Aldrich) and supported in a quartz U-shape reactor tube (I.D. = 10 mm) between two pieces of quartz wool. The reactor was placed into an electric furnace, and the reaction temperature was measured and controlled using a thermocouple attached to the outside wall of the reactor in a position corresponding to the middle of the catalyst bed length. Both inlet and outlet gas lines were heated at 120 °C to prevent condensation. Gaseous products were analyzed using an *online* gas chromatograph (Shimadzu GC-2014) equipped with two channels of separation and detection: *i*) a polar carboxen 1010 PLOT capillary column (30 m x 0.32 mm #35789-02A) coupled with thermal conductivity (TCD) and flame ionization (FID) detectors; and *ii*) a CP-Molsieve 5A column (25 m x 0.53 mm #CP7538) coupled with a TCD detector. Before starting the reaction, each catalyst was heated up to reaction temperature under 60 $cm^3\ min^{-1}$ of a mixture O_2:He:N_2 (molar ratio 2:3:1). Such is the heating process typically used before testing the steady-state OCM activity of the Mn-Na_2WO_4/SiO_2 catalyst because increasing temperature under oxidizing conditions has been proposed to enhance the C_2 selectivity.

The reaction started by feeding 100 $cm^3\ min^{-1}$ of an OCM mixture CH_4:O_2:He:N_2 (molar ratio 2:1:1.5:0.5) to the reactor. N_2 was used as a GC internal standard. The OCM catalytic activity was measured at 650, 700, 750, and 800 ºC after 30 min to allow the system to reach the steady-state at each temperature. The water produced was separated from the gaseous products before entering the GC using a condenser trap. The conversion of methane (X_{CH4}) and the selectivity to C_2 hydrocarbons (S_{C2}) were calculated from the mole number of the detected compounds, derived from a carbon balance of the system as follows:

$$X_{CH_4} = \frac{(CH_4)_{in} - (CH_4)_{out}}{(CH_4)_{in}} \cdot 100 \tag{3.1}$$

$$S_{C_2} = \frac{2\,(C_2H_4 + C_2H_6)}{2\,(C_2H_4 + C_2H_6) + CO_2 + CO} \cdot 100 \tag{3.2}$$

Replicate experiments involving reloading catalysts into the reactor resulted in standard deviations near 0.85% for both X_{CH4} and S_{C2}.

Chapter 4

"*Chemical Engineers are not gentle people, they like high temperatures and high pressures*" - Steve LeBlanc

Catalyst structure at real OCM temperatures

4.1 Results and Discussion

In this chapter, the WO_3/SiO_2, Na_2WO_4/SiO_2, and Mn-Na_2WO_4/SiO_2 catalysts are initially characterized at ambient conditions to ensure they correspond to the materials widely reported in the literature. The catalyst structure is then monitored at heating under oxidizing conditions (*i.e.*, typical pretreatment used to test the steady-state OCM performance) to elucidate the W and Mn sites structure at real OCM temperatures. The main results of this chapter can be also found in ORTIZ-BRAVO *et al.* (2021).

4.1.1 Chemical Composition

Table 4.1 lists the chemical composition of the synthesized WO_3/SiO_2, Na_2WO_4/SiO_2, and Mn-Na_2WO_4/SiO_2 catalysts.

Table 4.1 Chemical composition of the WO_3/SiO_2, Na_2WO_4/SiO_2, and Mn-Na_2WO_4/SiO_2 catalysts.

Catalyst	Atom	Nominal concentration [wt.%]	Measured concentration [wt.%]	Standard deviation	RSD [a] [%]	C_f [b]
WO_3/SiO_2	W	3.1	3.28	0.03	1.03	0.09
Na_2WO_4/SiO_2	W	3.1	3.36	0.01	0.32	0.10
	Na	0.9	0.96	0.01	0.98	0.04
Mn-Na_2WO_4/SiO_2	W	3.1	3.38	0.11	0.13	0.10
	Na	0.9	0.86	0.01	0.60	0.04
	Mn	2.0	2.01	0.00	0.20	0.05

[a] Relative standard deviation
[b] Confidence limit with a confidence level of 95.4% (2 sigma)

The nominal weight loadings of the Mn, Na, and W cations agree well with the theoretical value in the conventional 2wt.% Mn-5wt.% Na_2WO_4/SiO_2 catalyst: 2 wt.% of Mn, 0.9 wt.% of Na, and 3.1 wt.% of W. Note that the W loading on the three catalysts and Na loading on the Na_2WO_4/SiO_2, and Mn-Na_2WO_4/SiO_2 catalysts are the same statistically as the variations on the metal loading are inside of the confidence interval.

4.1.2 Specific Surface Area

Figure 4.1 depicts the N_2 adsorption-desorption isotherms and the measured specific surface area of the synthesized WO_3/SiO_2, Na_2WO_4/SiO_2, and Mn-Na_2WO_4/SiO_2 catalysts.

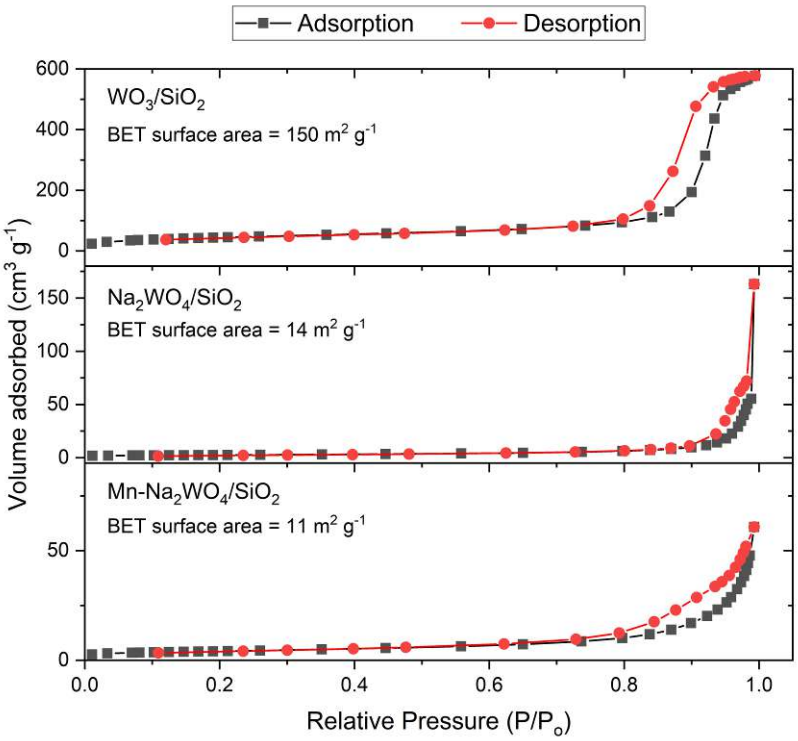

Figure 4.1 N_2 adsorption-desorption isotherm of the synthesized catalysts.

The synthesized catalysts exhibit a significantly lower specific surface area than the amorphous silica used as support (401 $m^2\ g^{-1}$). This can be attributed to the partial plugging of the silica pores by the supported oxides (especially W oxides with high atomic mass) limiting the accessibility of N_2 molecules and the partial collapse of the porous silica structure at the high calcination temperature employed (800 ºC). The Na_2WO_4/SiO_2 and Mn-Na_2WO_4/SiO_2 catalysts exhibited a more dramatic decrease in the specific surface area (14 and 11 $m^2\ g^{-1}_{cat}$, respectively) than the WO_3/SiO_2 catalyst (150 $m^2\ g^{-1}_{cat}$) due to the presence of Na^+ cations, which collapse the porous silica structure during the catalyst calcination. Indeed, Na^+ cations diffuse within the silica framework, cleave the Si-O-Si bridges, and form non-bridging oxygen bonds, which are typical of crystalline silica phases (MAZZARA *et al.*, 2000). The Na-induced silica crystallization with the simultaneous decrease in the specific surface area during catalyst calcination has been extensively reported for the Mn-Na_2WO_4/SiO_2 catalyst (ARNDT *et al.*, 2012, KIANI *et al.*, 2019).

4.1.3 Crystalline Structure

The qualitative phase identification of the synthesized catalysts was performed via XRD analysis at room temperature (RT) and temperature-programmed oxidation (TPO). Figure 4.2 shows the RT-XRD patterns of the WO_3/SiO_2, Na_2WO_4/SiO_2, and Mn-Na_2WO_4/SiO_2 catalysts.

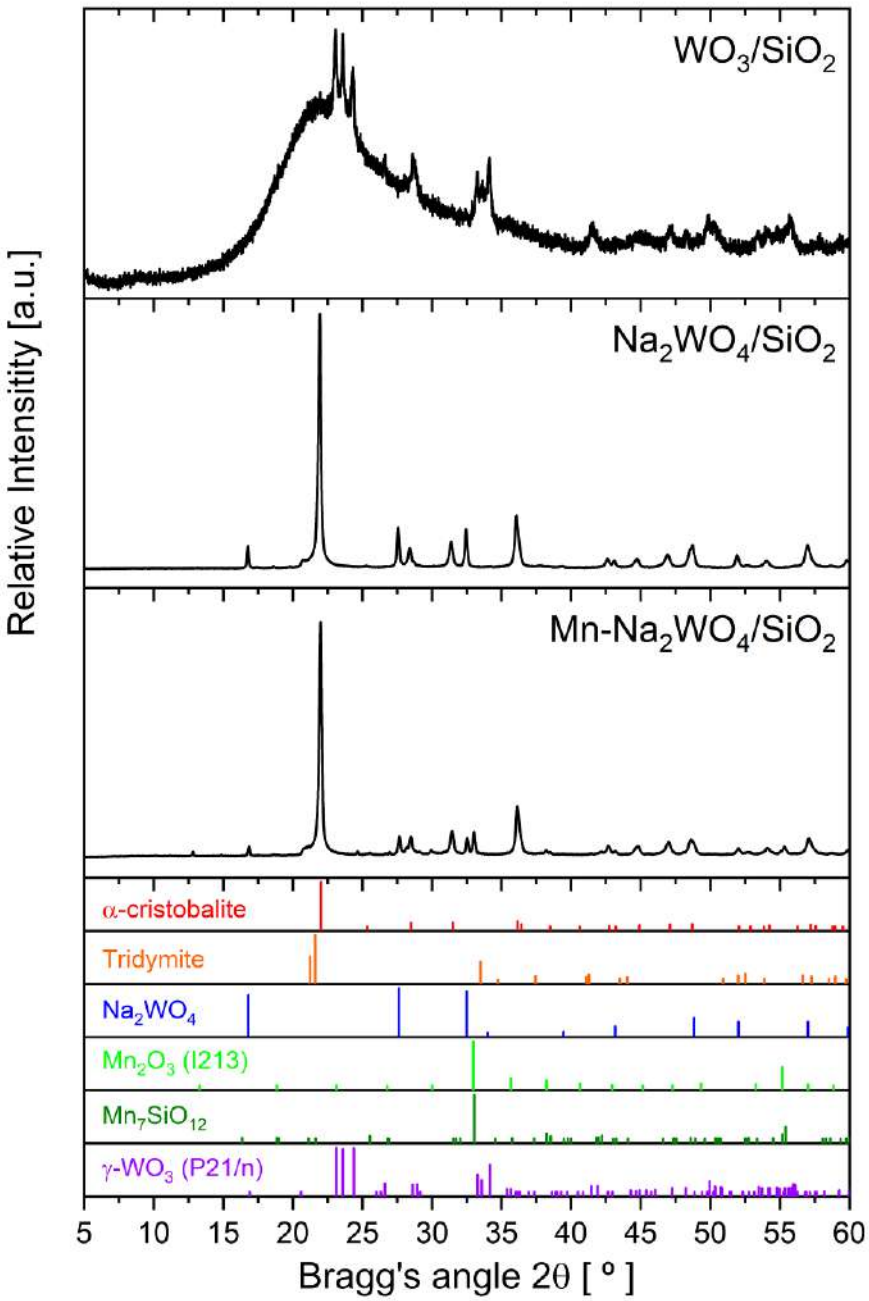

Figure 4.2 RT-XRD patterns of the WO_3/SiO_2, Na_2WO_4/SiO_2, and Mn-Na_2WO_4/SiO_2 catalysts. Diffraction patterns of the identified crystalline phases are also included: α-cristobalite [ICSD 030269] (red tick marks), tridymite [ICSD 038252] (orange tick marks), Na_2WO_4 [ICSD 028474] (blue tick marks), Mn_2O_3 [ICSD 033647] (light green tick marks), Mn_7SiO_{12} [ICSD 012123] (dark green tick marks), and γ-WO_3 [ICSD 016080] (purple tick marks).

The WO_3/SiO_2 catalyst maintains the amorphous silica phase of the support, exhibiting only diffraction peaks related to the crystalline monoclinic (space group P21/n) γ-WO_3 phase. The formation of crystalline WO_3 phase on the catalyst surface occurs by the decrease in the specific surface area produced during calcination to values below those required to maintain the surface density of W atoms lower than the monolayer coverage (~ 0.5 W-atoms nm^{-2}) (ROSS-MEDGAARDEN & WACHS, 2007). The resulting surface density of W atoms on the WO_3/SiO_2 catalyst (~ 0.7 W-atoms nm^{-2}) leads to the formation of 3D WO_3 crystallites, in agreement with Howell *et al.* (HOWELL *et al.*, 2016). However, because the surface density of W atoms is near to the monolayer coverage, the presence of dispersed WO_x species along with WO_3 crystallites cannot be immediately ruled out and needs to be inspected via Raman spectroscopy (*vide infra*).

The catalysts containing Na^+ (*i.e.*, Na_2WO_4/SiO_2 and Mn-Na_2WO_4/SiO_2) exhibit diffraction peaks related to the cubic (Fd-3m) Na_2WO_4 phase and two crystalline silica phases: tetragonal (P41212) α-cristobalite and orthorhombic (I212121) tridymite. Both silica phases were formed by the Na-induced crystallization of the amorphous silica used as support during the catalyst calcination, in agreement with the textural characterization and the literature (ELKINS & HAGELIN-WEAVER, 2015, PALERMO *et al.*, 1998, PALERMO *et al.*, 2000). Additionally, the Mn-Na_2WO_4/SiO_2 catalyst exhibits a low-intensity diffraction peak near $2\theta = 33.02^o$ attributable to either Mn_2O_3 (Bixbyite) or Mn_7SiO_{12} (Braunite). Discriminating between these phases is challenging because both exhibit their highest intensity peak near each other. The (2 2 2) reflection of Mn_2O_3 is at $2\theta = 32.94^o$ and the (2 2 4) reflection of Mn_7SiO_{12} is at $2\theta = 33.04^o$. The crystalline Mn_2O_3 phase was chosen to complete the qualitative identification of the crystalline phases present on the Mn-Na_2WO_4/SiO_2 catalyst, as will be shown with its corresponding Raman spectrum.

The thermal stability of the crystalline phases identified at room temperature was monitored by *in situ* TPO-XRD analysis. Figure 4.3 shows the *in situ* TPO-XRD patterns of the WO_3/SiO_2 catalyst and some diffraction patterns of WO_3 polymorphs that can form at heating. The qualitative phase identification is challenging because of the low resolution of the patterns. This is caused by the low crystallite size of the WO_3 crystallites and the faster step counting time compared with the RT-XRD measurements. However, the crystalline WO_3 phase can be monitored by following two groups of the main diffraction peaks at $22^o < 2\theta < 25^o$ and $32^o < 2\theta < 34^o$.

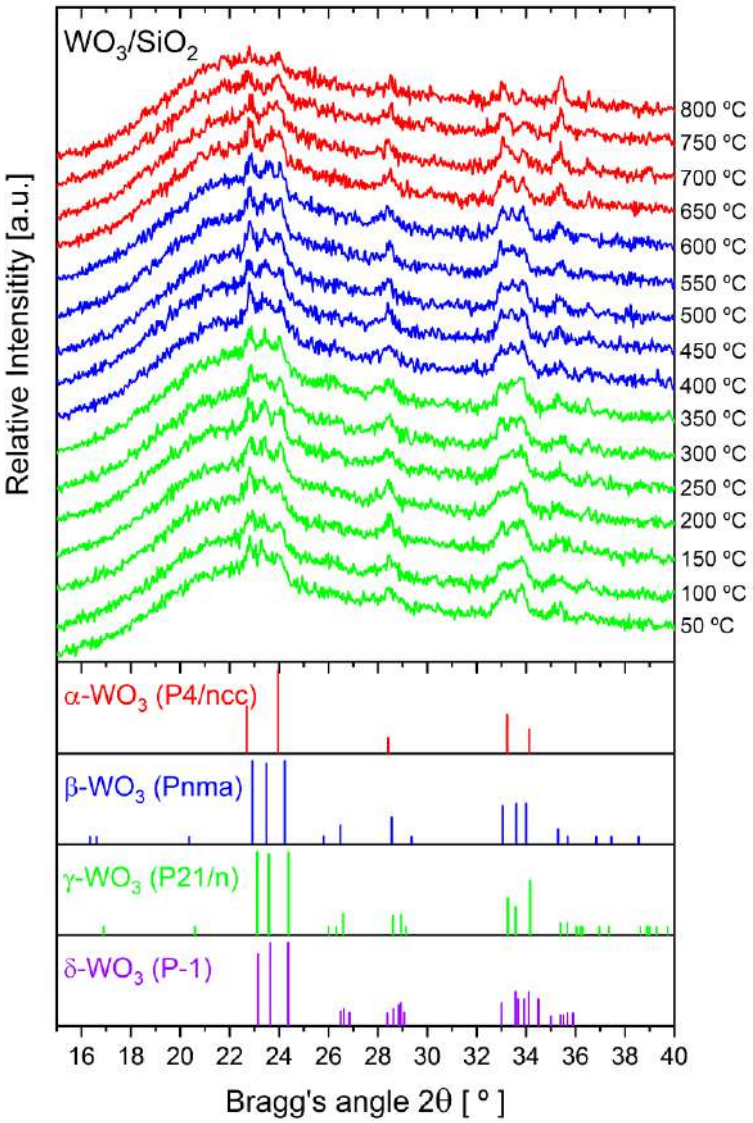

Figure 4.3 *In situ* TPO-XRD patterns of the WO_3/SiO_2 catalyst recorded between 50 ºC and 800 ºC (10 ºC min^{-1}) under O_2:Ar = 1:4 (100 cm^3 min^{-1}). Diffraction patterns of some WO_3 polymorphs are also included: tetragonal (P4/ncc) α-WO_3 [ICSD 027961] (red tick marks), orthorhombic (Pnma) β-WO_3 [ICSD 000836] (blue tick marks), monoclinic (P21/n) γ-WO_3 [ICSD 016080] (green tick marks), and triclinic (P-1) δ -WO_3 [ICSD 080055] (purple marks).

At heating, the diffractograms remain almost unchanged until 400 ºC, when the three diffraction peaks at 32º < 2θ < 34º window exhibit similar intensity, suggesting the presence of the orthorhombic (Pnma) β-WO_3 phase. A distinct diffraction pattern characterized by four peaks at 2θ = 22.88º and 23.87º, and 2θ = 33.23º and 33.84º are observed at 650 ºC, suggesting the presence of the tetragonal (P4/ncc) α-WO_3 phase, which remains stable until 800 ºC. The reversible temperature-induced (monoclinic) γ ↔ (orthorhombic) β ↔ (tetragonal) α-WO_3 phase transition has been previously reported for WO_3 crystallites in the literature (POKHREL *et al.*, 2015, THUMMAVICHAI *et al.*, 2018).

Figure 4.4 shows the *in situ* TPO-XRD patterns of the Na_2WO_4/SiO_2 and Mn-Na_2WO_4/SiO_2 catalysts. Although the diffraction peaks of the tridymite phase of the support do not evolve at heating and are still present at 800 ºC, the α-cristobalite transforms into the β-cristobalite phase. The (1 0 1) (2θ = 22.02º), (1 1 1) (2θ = 28.49º), (1 0 2) (2θ = 31.49º), and (2 0 0) (2θ = 36.16º) diffraction peaks of the α-cristobalite phase vanish, while the (1 1 1) (2θ = 21.46º) and (2 2 0) (2θ = 35.40º) peaks of the cubic (Fd-3m) β-cristobalite phase appear above 200 ºC and remain stable until 800 ºC.

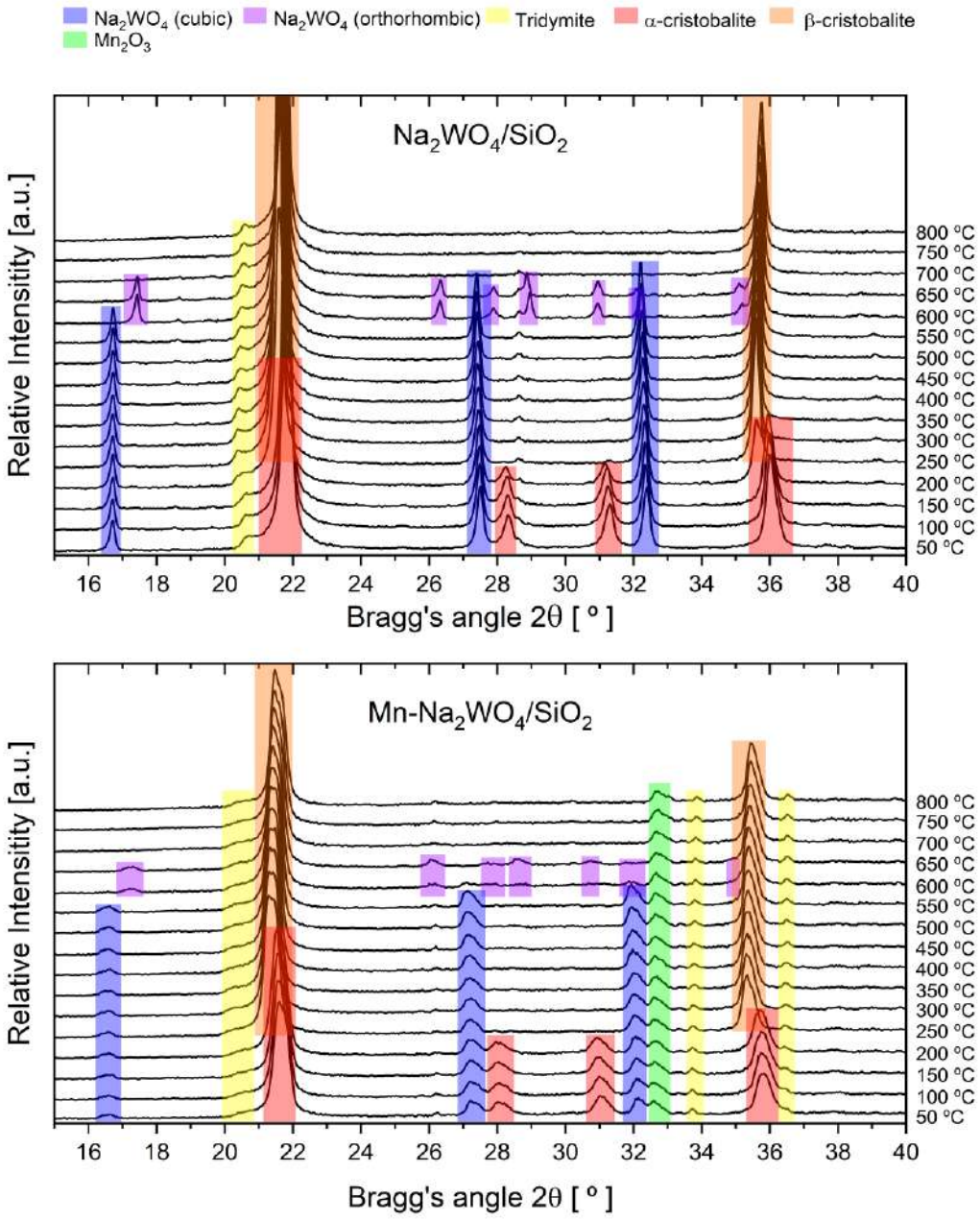

Figure 4.4 *In situ* TPO-XRD patterns of the Na_2WO_4/SiO_2 and Mn-Na_2WO_4/SiO_2 catalysts recorded between 50 ºC and 800 ºC (10 ºC min^{-1}) under O_2:Ar = 1:4 (100 cm^3 min^{-1}). Diffraction patterns of the crystalline phases identified at high temperatures are also included: orthorhombic (Pnam) Na_2WO_4 [ICDD 00-020-1163] (purple box) and cubic (Fd-3m) β-cristobalite [ICSD 034924] (orange box).

The diffraction peaks of the cubic Na_2WO_4 phase disappear at 600 ºC, while the diffraction peaks of the lower symmetry orthorhombic Na_2WO_4 phase arise and remain present until 650 ºC. Further heating leads to the complete disappearance of the Na_2WO_4 reflections, suggesting its melting. Differential scanning calorimetry (DSC) and Raman spectroscopy results reported in the literature show that these transitions are reversible (SADJADI *et al.*, 2015, WERNY *et al.*, 2020). The α ↔ β-cristobalite transition occurs at 232 ºC (α → β) and 222 ºC (β → α) and the orthorhombic ↔ molten Na_2WO_4 transition occurs at 680 ºC (orthorhombic → molten) and 657 ºC (molten → orthorhombic) (SADJADI *et al.*, 2015). The reversibility of these phase transitions explains the importance of conducting *in situ* studies since characterizing either fresh or spent catalysts at room temperature does not provide information about the catalyst structure at real OCM reaction conditions.

The *in situ* TPO-XRD patterns of the Mn-Na_2WO_4/SiO_2 catalyst show that the crystalline Mn_2O_3 phase is stable and remains present at 800 ºC. Although the Mn-Na_2WO_4/SiO_2 catalyst exhibit the same crystalline phases associated with the catalytic activity in the literature at room temperature (*i.e.*, α-cristobalite, Na_2WO_4, and Mn_2O_3) (JI *et al.*, 2002, 2003, PALERMO *et al.*, 1998, PALERMO *et al.*, 2000), it only presents the crystalline Mn_2O_3 phase at relevant OCM reaction temperatures (> 650 ºC). Therefore, the association of any OCM performance with the crystalline phases observed at room temperature is inadequate. On the other hand, the W structure at temperatures above 700 ºC remains, however, incompressible based only on XRD evidence because of the Na_2WO_4 melting. In this regard, Raman spectroscopy is a powerful tool because it provides detailed structural information not only of crystalline phases but also of dispersed, amorphous, and molten ones.

4.1.4 UV-vis Spectroscopy

Figure 4.5 shows the UV-vis spectra of the WO_3/SiO_2, Na_2WO_4/SiO_2, and Mn-Na_2WO_4/SiO_2 catalysts recorded at ambient conditions and their corresponding ligand-to-metal-charge-transfer (LMCT) band positions.

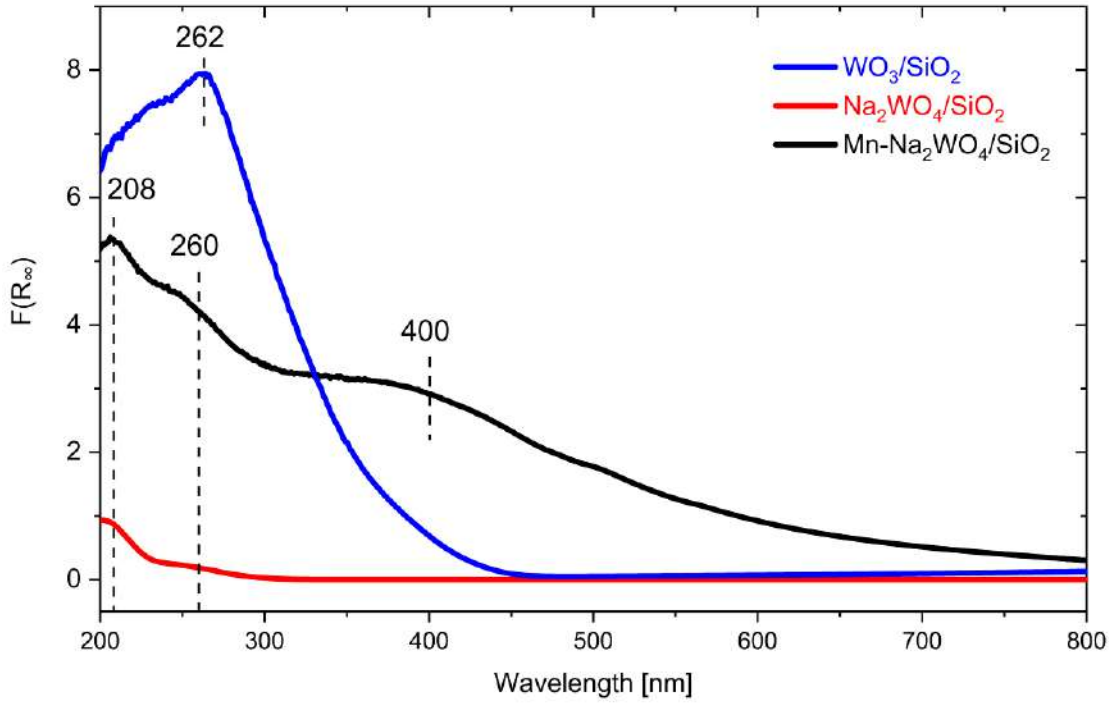

Figure 4.5 UV-vis spectra of the WO_3/SiO_2, Na_2WO_4/SiO_2, and Mn-Na_2WO_4/SiO_2 catalysts.

The WO_3/SiO_2 catalyst exhibits a strong LMCT band at 262 nm that corresponds to the crystalline WO_3 phase, in agreement with the XRD results elsewhere (ROSS-MEDGAARDEN & WACHS, 2007). Conversely, the Na_2WO_4/SiO_2 and Mn-Na_2WO_4/SiO_2 catalysts exhibit two strong LMCT bands at 208 and 260 nm related to the Na_2WO_4 phase (ROSS-MEDGAARDEN & WACHS, 2007). The absence of UV-vis absorption in the 400–700 nm range indicates that the supported tungsten oxide phases are in their fully oxidized state (W^{6+}) (KIANI *et al.*, 2020). Additionally, the Mn-Na_2WO_4/SiO_2 catalyst exhibits an additional band at 400 nm related to Mn oxide species.

4.1.5 *In situ* TPO-Raman Study

The complete identification of species on the synthesized catalysts was performed by Raman spectroscopy at RT and TPO. Figure 4.6 shows the *in situ* TPO-Raman spectra of the dehydrated WO_3/SiO_2, Na_2WO_4/SiO_2, and Mn-Na_2WO_4/SiO_2 catalysts recorded between 25 ºC (RT) and 800 ºC. The spectra were normalized against the Rayleigh band at 0 cm^{-1}, in agreement with the literature (WEI *et al.*, 2018).

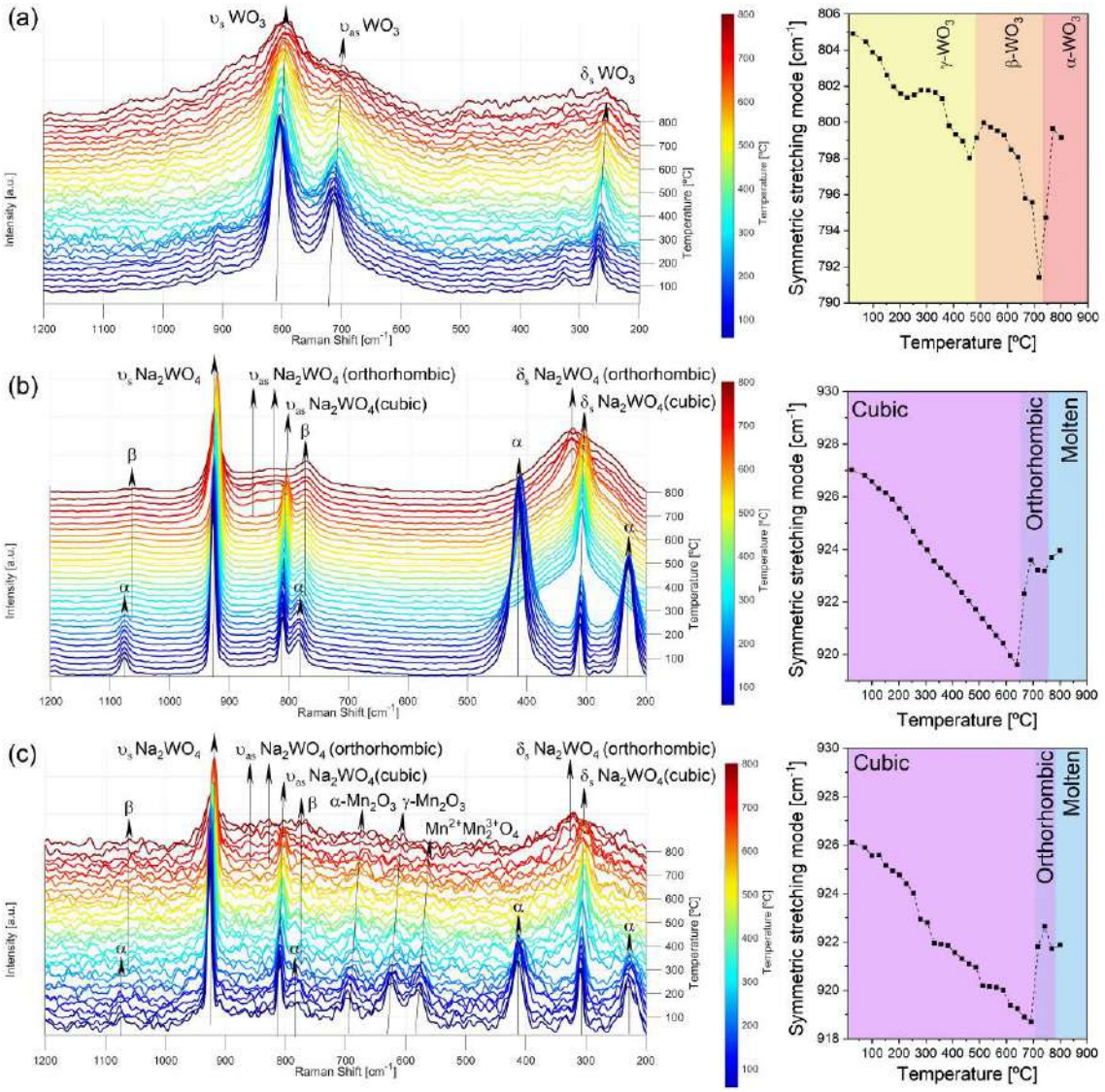

Figure 4.6 *In situ* TPO-Raman spectra (excitation at 405 nm, normalization against Rayleigh band at 0 cm^{-1}), left, and position of the ν_s vibration band (symmetric stretching mode) of tungsten species as a function of temperature, right, of the dehydrated: (a) WO_3/SiO_2, (b) Na_2WO_4/SiO_2, and (c) Mn-Na_2WO_4/SiO_2 catalysts recorded between 25 ºC and 800 ºC (10 ºC min^{-1}) under O_2:Ar = 1:2 (60 cm^3 min^{-1}).

At room temperature, the dehydrated WO_3/SiO_2 catalyst exhibits Raman bands typically ascribed to crystalline WO_3 phase, in agreement with the RT-XRD findings elsewhere (Figure 4.6a, left) (BOULOVA & LUCAZEAU, 2002). The crystalline WO_3 phase has three major Raman bands at 805, 713, and 265 cm^{-1}, corresponding to the symmetrical (ν_s) and asymmetrical (ν_{as}) stretching modes and the bending (δ_s) mode of the bridging W-O-W bond, respectively (ROSS-MEDGAARDEN & WACHS, 2007). Although the surface density of W atoms on the catalyst is close to the monolayer coverage value, the Raman spectra, sensitive to dispersed oxide phases, do not exhibit bands related to WO_x species.

The dehydrated Na_2WO_4/SiO_2 and Mn-Na_2WO_4/SiO_2 catalysts exhibit Raman bands related to the crystalline α-cristobalite and cubic Na_2WO_4 phases (Figure 4.6b-c, left). The α-cristobalite phase gives rise to Raman bands at 1075, 785, 415, and 228 cm^{-1} (BATES, 1972). Meanwhile, the Na_2WO_4 phase exhibits Raman bands at 926, 810, and 309 cm^{-1}, corresponding to the symmetrical (ν_s) and asymmetrical (ν_{as}) stretching modes and the bending (δ_s) mode of the W-O bond, respectively (HARDCASTLE & WACHS, 1995). Dispersed WO_x species on the dehydrated Na_2WO_4/SiO_2 and Mn-Na_2WO_4/SiO_2 catalysts were not observed, in agreement with WERNY *et al.* (2020). Finally, as discussed elsewhere, determining whether Mn_2O_3 (Bixbyite) or Mn_7SiO_{12} (Braunite) or both phases are present on the Mn-Na_2WO_4/SiO_2 catalyst only by XRD analysis is challenging. However, after inspecting the Raman spectrum at room temperature, the Mn_7SiO_{12} phase can be ruled out because of the absence of Raman bands in the 470-550 cm^{-1} window (RRUFF Database: Raman, X-ray, Infrared, and Chemistry). Thus, the Raman bands at 698, 624, and 564 cm^{-1} are associated with the crystalline α-Mn_2O_3, γ-Mn_2O_3, and hausmanite $Mn^{2+}Mn^{3+}{}_2O_4$ phases, respectively (BUCIUMAN *et al.*, 1999, DATA & REFERENCES, 2009).

After XRD, UV-vis, and Raman spectroscopies characterization, one can observe that the W sites on the synthesized catalysts present different local structures: they present different site symmetry. Indeed, the W sites are octahedrally coordinated (O_h-symmetry) on the WO_3/SiO_2 catalyst (O_h-W^{6+} sites in the WO_3 phase) and tetrahedrally coordinated (T_d-symmetry) on the Na_2WO_4/SiO_2 and Mn-Na_2WO_4/SiO_2 catalysts (T_d-W^{6+} sites in the Na_2WO_4 phase) (HORSLEY *et al.*, 1987, ROSS-MEDGAARDEN & WACHS, 2007). Raman spectroscopy is also sensitive to the symmetry of the W sites. The position of the most intense Raman band denotes the highest bond order (shortest W-O bond) of tungsten species (HORSLEY *et al.*, 1987). Thus, the crystalline WO_3 phase (O_h-W^{6+} sites) exhibits the most intense Raman band, related to the symmetrical (ν_s) stretching mode, at lower wavenumber (805 cm^{-1}) than the crystalline Na_2WO_4 phase (T_d-W^{6+} sites) (~ 926 cm^{-1}) due to the lower bond order of the former (HORSLEY *et al.*, 1987, ROSS-MEDGAARDEN & WACHS, 2007).

The different symmetry of the W sites on the synthesized catalysts is due to the presence of Na^+ cations. WU & LI (1995) studied the role of Na^+ in the W sites symmetry by adding 1.2wt.% Na (using $NaNO_3$) into the 3wt.% WO_3/SiO_2 catalyst (synthesized from $(NH_4)_6H_2W_{12}O_{40}\cdot nH_2O$, AMT). The resulting catalyst exhibited Raman bands related to T_d-W^{6+} sites in the crystalline Na_2WO_4 phase, which was also

identified by XRD analysis. Furthermore, KIANI *et al.* (2020) recently studied the molecular and electronic structure of the W sites on model SiO_2-supported Na-promoted tungsten oxide catalysts using various Na- and W-precursors. The W sites presented T_d symmetry on the dispersed Na-WO_4 and crystalline Na_2WO_4 phases, irrespective of the precursor used for catalysts with a Na/W molar ratio of 2, which mimicked the stoichiometry of the Na_2WO_4 phase. Using AMT and NaOH as precursors led to the exclusive formation of dispersed highly distorted pseudo-tetrahedral WO_4 units coordinated to Na^+ cations for Na/W molar ratios lower than 1.6 with distortion in tetrahedral geometry decreased with the Na/W molar ratio. However, replacing Na precursor with other with lower pH (*i.e.*, $NaNO_3$) led to the formation of the crystalline WO_3 phase with O_h-W^{6+} sites even at a low Na/W molar ratio (0.4).

The temperature-induced structural modifications of the W sites can be followed by measuring the position of the ν_s vibration band because changes in the oxidation state and/or distortion degree impose variations on the bond order of tungsten species (HORSLEY *et al.*, 1987). Figure 4.6, right, shows the position of the ν_s vibration band of the crystalline WO_3 phase on the WO_3/SiO_2 catalyst (a) and the crystalline Na_2WO_4 phase on the Na_2WO_4/SiO_2 (b) and Mn-Na_2WO_4/SiO_2 (c) catalysts as a function of temperature in the TPO-Raman study. The ν_s vibration band in the WO_3/SiO_2 catalyst red shifts with increasing temperature but undergoes two sharp blue shifts near 450 and 700 ºC, suggesting the temperature-induced γ (monoclinic) → β (orthorhombic) → α-WO_3 (tetragonal) phase transitions, respectively (Figure 4.6a, right). The overall red shift indicates a decrease in the bond order of the O_h-W^{6+} sites with increasing temperature. This is due to an elongation of the W-O bond resulting from a variation in the oxidation state and/or distortion degree of the W sites. The sequential γ → β → α-WO_3 phase transitions are corroborated by following the δ_s vibration band, which monotonically red shifts with temperature up to ~ 700 ºC and then vanish. Furthermore, the presence of the crystalline α-WO_3 phase at 800 ºC is confirmed by the broadening of the ν_{as} vibration band (Figure 4.6a, left) (BOULOVA & LUCAZEAU, 2002).

The TPO-Raman study of the dehydrated Na_2WO_4/SiO_2 catalyst also uncovers the α → β-cristobalite and cubic → orthorhombic → molten Na_2WO_4 transitions observed via TPO-XRD analysis elsewhere. Regarding the α → β-cristobalite phase transition, the band at 1075 cm^{-1} broadens, weakens, and slightly red shifts to 1073 cm^{-1}, the band at 785 cm^{-1} slightly red shifts to 782 cm^{-1}, and the bands at 415 and 228 cm^{-1} vanish above 250 ºC. Thus, the crystalline β-cristobalite phase gives rise to Raman bands at

1073, 782, and 292 cm^{-1}, which remain constant until 800 ºC (Figure 4.6b, left) (BATES, 1972). Note that the δ_s vibration band of the cubic Na_2WO_4 phase (~309 cm^{-1}) overlaps the β-cristobalite band at 292 cm^{-1} above 250 ºC, in agreement with the literature (KIANI *et al.*, 2020). Concerning the Na_2WO_4 phase transitions: the ν_s vibration band of the Na_2WO_4/SiO_2 catalyst red shifts with temperature but undergoes two sharp blue shifts near 650 and 750 ºC, suggesting the temperature-induced cubic → orthorhombic → molten Na_2WO_4 transitions, respectively. The cubic → orthorhombic Na_2WO_4 transition is also corroborated by the blue shift of the δ_s vibration from 309 to 319 cm^{-1} and the split of the ν_{as} vibration band at 810 cm^{-1} into two smaller ones at 847 and 820 cm^{-1}, as shown in Figure 4.6b, left (LIMA *et al.*, 2011, WANG, Jian *et al.*, 2018). The new two bands related to the ν_{as} vibration band of the orthorhombic Na_2WO_4 phase lose intensity with a further temperature increase and the ν_s band blue shifts, suggesting the melting of the Na_2WO_4 phase near 750 ºC (Fig 4.6b, right).

The temperature-induced γ → β → α-WO_3, α → β-cristobalite, and cubic → orthorhombic → molten Na_2WO_4 transitions observed by the TPO-Raman study take place at higher temperatures than those observed by the TPO-XRD analysis. This is due to the different temperature-programmed ramping used. The TPO-Raman study used a continuous ramping, whereas the TPO-XRD analysis used a stepwise ramping, pausing each 50 ºC to cover the 2θ window measured. The phase transitions mentioned elsewhere takes some minutes to become completed. For instance, the complete formation of the orthorhombic Na_2WO_4 phase is a thermal event lasting ~ 4 min or ~ 40 ºC in a continuous heating ramp of 10 ºC min^{-1} under oxidizing conditions, as reported in the literature from DSC measurements (WERNY *et al.*, 2020).

Monitoring the structure of the W sites on the conventional Mn-Na_2WO_4/SiO_2 catalyst during the heating via Raman spectroscopy is challenging due to the broadness of the bands (Figure 4.6c, left). The UV-vis spectra of the WO_3/SiO_2, Na_2WO_4/SiO_2, and Mn-Na_2WO_4/SiO_2 catalysts (Figure 4.5) show that the addition of Mn increased the radiation absorption, as a broad band appears near 400 nm. The sequential cubic → orthorhombic → molten Na_2WO_4 transitions evidenced in the Na_2WO_4/SiO_2 catalyst can also be observed on the dehydrated Mn-Na_2WO_4/SiO_2 catalyst. The ν_s vibration shows an overall red shift with increasing temperature up to near 700 ºC, and then, two sudden blue shifts above 700 and 780 ºC, associated with the cubic → orthorhombic → molten Na_2WO_4 transitions, respectively (Figure 4.6c, right).

These transitions take place at higher temperatures than on the Na_2WO_4/SiO_2 catalyst (above 650 and 750 ºC, respectively), suggesting that the presence of Mn may alter the temperature dependence of the bond order of the W sites. Finally, the α → β-cristobalite phase transition and the presence of the crystalline Mn_2O_3 phase on the dehydrated Mn-Na_2WO_4/SiO_2 catalyst throughout the heating was elucidated by chemometric component analysis of a hard model using PEAXACT software, as shown in Figure 4.7). The α → β-cristobalite phase transition occurs near 250 ºC, as in the Na_2WO_4/SiO_2 catalyst, while the crystalline Mn_2O_3 phase remains stable up to 800 ºC, in agreement with the *in situ* TPO-XRD findings elsewhere.

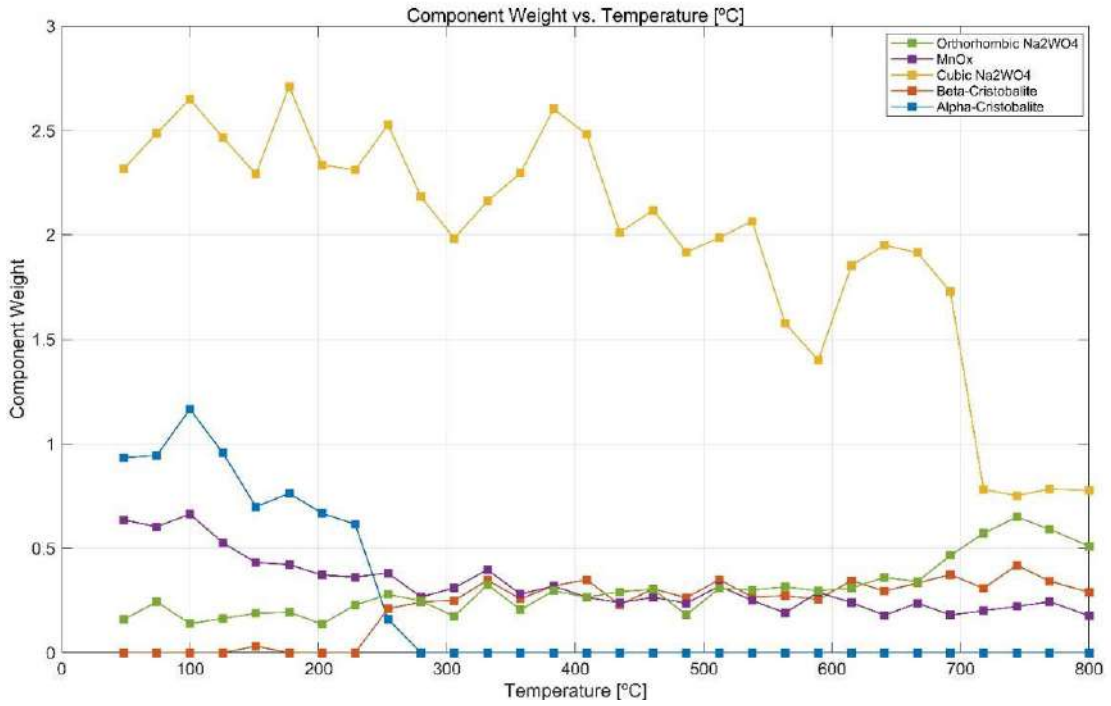

Figure 4.7 Chemometric component analysis of the *in situ* TPO-Raman spectra for the Mn-Na_2WO_4/SiO_2 catalyst. Showing the component weight of the Raman bands related to the orthorhombic Na_2WO_4 (green line), Mn_2O_3 (violet), cubic Na_2WO_4 (yellow), β-cristobalite (red), and α-cristobalite (blue) phases.

Although the cubic → orthorhombic → molten Na_2WO_4 phase transitions have already been reported in the literature, the TPO-Raman study reveals new insights about the structural changes of the W sites. Indeed, the ν_s vibration band shift indicates that the bond order of the W sites changes, but it is unclear if this is due to a temperature-induced change in the oxidation state and/or the distortion degree. Understanding the structure of the W sites in the molten Na_2WO_4 phase is crucial because this phase is present at temperatures where the OCM reactions are thermodynamically relevant (*i.e.*, > 650 ºC).

4.1.6 *In situ* TPO-XANES spectroscopy

The electronic and molecular structure of the W and Mn sites on the synthesized catalysts was also studied via *in situ* TPO-XANES spectroscopy to elucidate if the shift of the ν_s vibration band observed in the *in situ* TPO-Raman study is due to a change in the oxidation state or distortion degree of the W sites or both. Figure 4.8 depicts the XANES spectra at the W-L_3 edge of the bulk WO_3, Na_2WO_4, and WO_2 reference materials recorded at 25 ºC and the *in situ* TPO-XANES spectra at the W-L_3 edge of the WO_3/SiO_2, Na_2WO_4/SiO_2, and Mn-Na_2WO_4/SiO_2 catalysts recorded at 25, 700, 750, and 800 ºC. Insets in the upper right-hand corner show a more detailed view of the edge region.

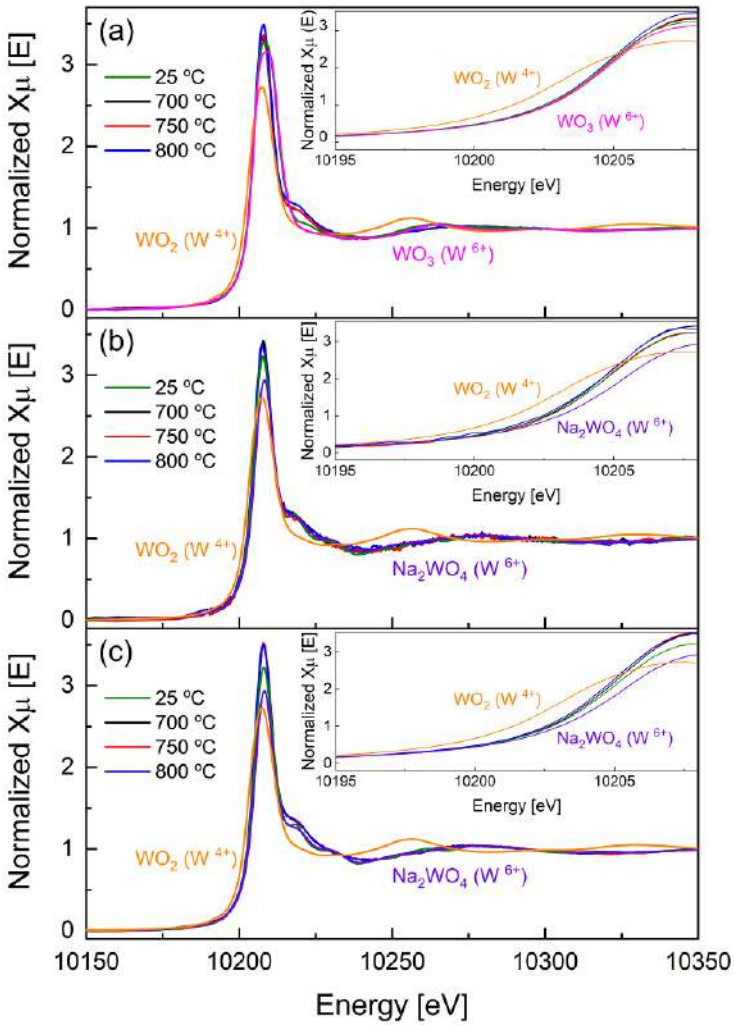

Figure 4.8 *In situ* TPO-XANES spectra at the W-L_3 edge of the: (a) WO_3/SiO_2, (b) Na_2WO_4/SiO_2, and (c) Mn-Na_2WO_4/SiO_2 catalysts recorded at 25, 700, 750, and 800 ºC flowing 10% O_2/He (10 cm^3 min^{-1}). Insets show a detailed view of the edge region. XANES spectra at the W-L_3 edge of the bulk WO_3 (W^{6+}), Na_2WO_4 (W^{6+}), and WO_2 (W^{4+}) reference materials recorded at 25 ºC are also included.

The electron transition from the $2p_{3/2}$ state to a vacant 5*d* state appears as an intense dipole-allowed peak in the absorbance curve, known as the "white line" (IWASAWA et al., 2017). To calculate the mean oxidation state of the W atoms, the W-L_3 edge position (*i.e.*, the absorption threshold) for the bulk WO_3, Na_2WO_4, and WO_2 reference materials and the WO_3/SiO_2, Na_2WO_4/SiO_2, and Mn-Na_2WO_4/SiO_2 catalysts was initially determined. Certainly, the energy shift on the W-L_3 edge position in tungsten species is due to differences in the mean oxidation state of the W atoms (GARCIA-GARCIA et al., 2015, KHYZHUN, 2000). The W-L_3 edge position was determined by using the intersection with the energy axis of the second derivative with respect to the energy of the normalized XANES curve.

The W-L_3 edge position measured for the bulk WO_3, Na_2WO_4, and WO_2 reference materials was 10205.3, 10205.6, and 10203.3 eV, respectively. Thus, the W-L_3 edge position depends not only on the mean oxidation state, WO_3 (W^{6+}) *vs.* WO_2 (W^{4+}), but also on the local structure of the W atom, WO_3 (O_h-W^{6+}) *vs.* Na_2WO_4 (T_d-W^{6+}), in agreement with the literature (IWASAWA et al., 2017). The W-L_3 edge position measured for the WO_3/SiO_2 catalyst at each temperature was interpolated to a straight line between the edge values recorded for the bulk WO_3 (O_h-W^{6+}) and WO_2 (O_h-W^{4+}) reference materials to estimate the mean oxidation state of the W sites, as shown in Figure 4.9a. Because the W-L_3 edge position also depends on the local structure of the W atoms, the mean oxidation state of the W sites on the Na_2WO_4/SiO_2 and Mn-Na_2WO_4/SiO_2 catalysts was calculated using the bulk Na_2WO_4 (T_d-W^{6+}) reference material instead of the WO_3 (O_h-W^{6+}), as shown in Figure 4.9b.

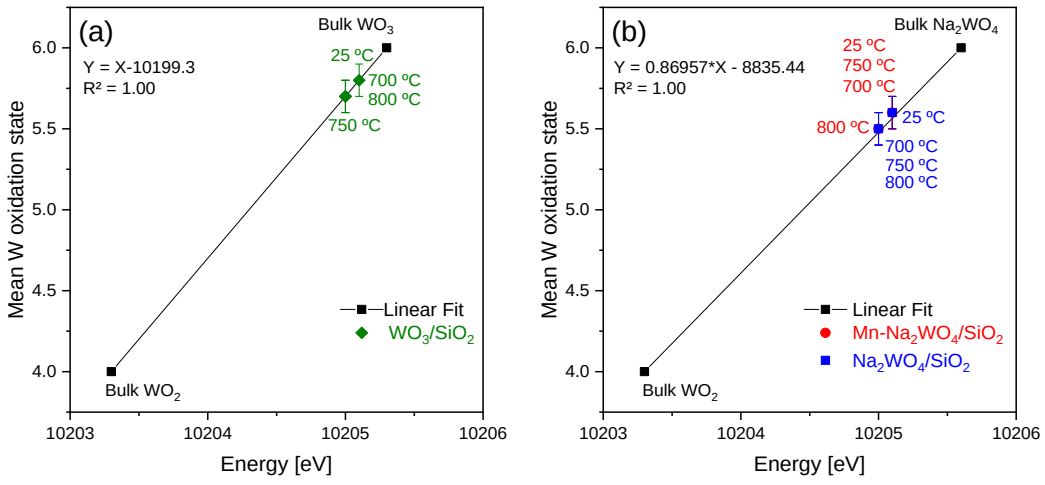

Figure 4.9 Energy positions at the W-L_3 edge *vs.* mean oxidation state of W sites on the catalysts: (a) WO_3/SiO_2 (green) between WO_3 (O_h-W^{6+}) - WO_2 (O_h-W^{4+}) and (b) Na_2WO_4/SiO_2 (red) and Mn-Na_2WO_4/SiO_2 (blue) between Na_2WO_4 (T_d-W^{6+}) - WO_2 (O_h-W^{4+}).

Table 4.2 summarizes the edge position and mean oxidation state of the W sites on each catalyst at 25, 700, 750, and 800 ºC.

Table 4.2 W-L_3 edge position according to the zero-crossing of the second derivative and mean W oxidation state obtained by interpolating the *in situ* TPO-XANES spectra at the W-L_3 edge of the WO_3/SiO_2, Na_2WO_4/SiO_2, and Mn-Na_2WO_4/SiO_2 catalysts.

Temperature [ºC]	WO_3/SiO_2		Na_2WO_4/SiO_2		Mn-Na_2WO_4/SiO_2	
	Edge position [eV]	Mean W oxidation state	Edge position [eV]	Mean W oxidation state	Edge position [eV]	Mean W oxidation state
25	10205.0	5.7 ± 0.1	10205.1	5.6 ± 0.1	10205.1	5.6 ± 0.1
700	10205.0	5.7 ± 0.1	10205.0	5.5 ± 0.1	10205.1	5.6 ± 0.1
750	10205.1	5.8 ± 0.1	10205.0	5.5 ± 0.1	10205.1	5.6 ± 0.1
800	10205.0	5.7 ± 0.1	10205.0	5.5 ± 0.1	10205.0	5.5 ± 0.1

All synthesized catalysts exhibit a lower W-L_3 edge position than the bulk WO_3 and Na_2WO_4 reference materials at room temperature, suggesting that the mean oxidation state of the W sites is lower than 6+, in line with the known chemistry of WO_3: its polymorphic nature, and tendency to form Magnéli phases, which stabilize cations with oxidation states below W^{6+} (GREENWOOD & EARNSHAW, 1998). Thus, the WO_3/SiO_2, Na_2WO_4/SiO_2, and Mn-Na_2WO_4/SiO_2 catalysts have W^{6+} sites with some electron polarons (*i.e.*, W^{5+} at a W^{6+} site). On the other hand, heating under oxidizing conditions did not shift the W-L_3 edge position out of the error in the energy resolution for any catalyst. Thus, the electronic state of the W sites remains as W^{5+}-W^{6+} at relevant OCM reaction temperatures. To summarize, the *in situ* TPO-XANES spectra indicate that the temperature-induced shift of the ν_s vibration band observed in the *in situ* TPO-Raman study is related to a variation in the distortion degree of the W sites instead of a variation in the oxidation state.

The intensity and shape of the white line also provide information about the oxidation state and symmetry/distortion of the W sites, respectively. The intensity is associated with the density of unoccupied states, and therefore with the oxidation state. Thus, the white line intensity of the WO_3 (W^{6+}) is higher than that of the WO_2 (W^{4+}) (IWASAWA *et al.*, 2017), Figure 4.8a. However, the higher intensity evidenced for the synthesized catalysts compared with the bulk WO_3 and Na_2WO_4 reference materials (even at room temperature) cannot be associated with a higher oxidation state of the W sites since the edge position remained unchanged. This effect is actually related to the

interaction of the WO_3 and Na_2WO_4 crystallites with the support. GARCÍA-LÓPEZ *et al.* (2019) recently showed that the white line intensity of the silica-supported Keggin $[PW_{12}O_{40}]^{3-}$ and Wells-Dawson $[P_2W_{18}O_{62}]^{6-}$ heteropolyanions were higher than that of the unsupported heteropolyanions. On the other hand, the white line shape depends on the symmetry/distortion of the W atoms. Although both WO_3 and Na_2WO_4 have the same oxidation state (W^{6+}, d^0), they present different white line shapes. The crystalline WO_3 phase (O_h-W) exhibits a broad peak with an indistinct top (Figure 4.8a), whereas the Na_2WO_4 (T_d-W) exhibits a sharper, more asymmetrical peak (Figure 4.8b-c). These differences are due to the splitting of the W 5*d* state by the ligand field. Thus, the broad white line of the O_h-W sites consists of two peaks related to the t_{2g} and e_g orbitals, whereas the narrow white line of the T_d-W sites is due to a smaller splitting of the W 5*d* state and consists of two peaks related to the *e* and t_g orbitals (ASAKURA *et al.*, 2011, YAMAZOE *et al.*, 2008).

To analyze the temperature-induced changes in the symmetry and distortion degree of the W sites, the white line shape of the synthesized catalysts at each temperature was interpreted by considering the final state of the 5*d* orbitals following a methodology proposed by YAMAZOE *et al.* (2008). The white line was deconvoluted by representing each electron transition to a vacant 5*d* split orbital with a Lorentz function and the vacuum level with an arctangent function. Thus, two Lorentz peaks, at lower and higher energy, related to the t_{2g} and e_g orbitals for the O_h-W^{6+} sites or the *e* and t_g orbitals for the T_d-W^{6+} sites, were adjusted. The two peaks in the second derivative of the bulk WO_3 and Na_2WO_4 materials in Figure 4.10 were considered as the input center values for the Lorentz peaks in catalysts with O_h-W^{6+} and T_d-W^{6+} sites, respectively. The $t_{2g}/e_g = 3/2$ and $e/t_g = 2/3$ peak ratios were considered as constraints. The arctangent functions adjusted for WO_3 and Na_2WO_4 were used to deconvolute the white line of the WO_3/SiO_2 catalyst and Na_2WO_4/SiO_2 and Mn-Na_2WO_4/SiO_2, irrespective of the temperature because the oxidation state of the samples was the same. The energy gap between both peak centers reflects the 5*d* state splitting. This analysis is similar to that carried out in previous works in the literature (ASAKURA *et al.*, 2011, BALERNA *et al.*, 1991, GARCÍA-LÓPEZ *et al.*, 2019, LIMAYE *et al.*, 2014, YAMAZOE *et al.*, 2008). Figure 4.11 shows a representative example of the fit performed for the bulk WO_3 material. The results of all the spectra deconvolutions are reported in Table 4.3, and Figure 4.12 contrasts the measured energy gap values with the phases identified by the *in situ* TPO-XRD analysis at each temperature window.

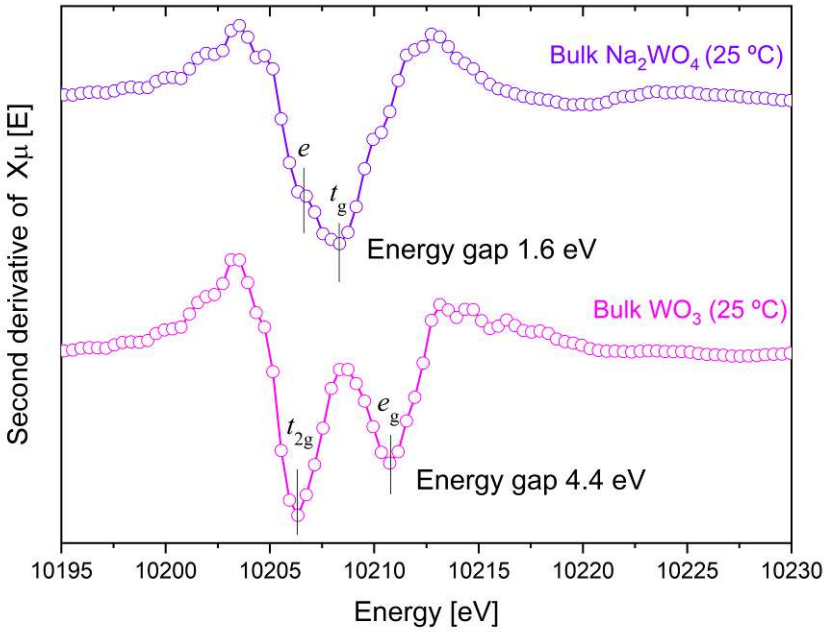

Figure 4.10 Second derivatives of the XANES spectra at the W-L_3 edge of the bulk Na_2WO_4 and WO_3 reference materials recorded at 25 ºC.

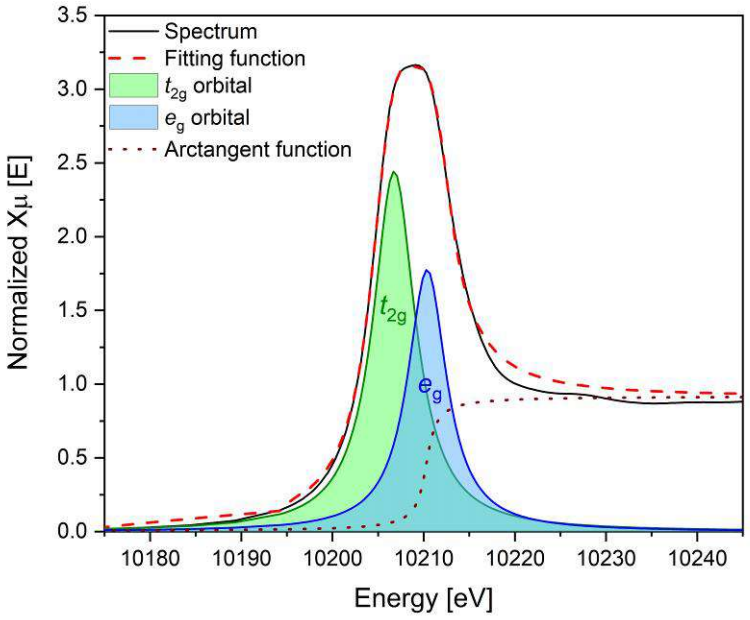

Figure 4.11 Deconvolution of XANES spectrum at the W-L_3 edge of the bulk WO_3 reference material. The black curve is the experimental XANES spectrum. The dashed red line is the fitting spectrum. Blue and green lines are the Lorentzian function adjusted to represent the t_{2g} and e_g orbitals, respectively. The dotted line is the arctangent function representing the vacuum level.

Table 4.3 Deconvolution of XANES spectra at the W-L_3 edge of the bulk WO_3 and Na_2WO_4 reference materials recorded at 25 ºC and the *in situ* TPO-XANES spectra at the W-L_3 edge of catalysts recorded at 25, 700, 750, and 800 ºC.

Catalyst	Temperature [ºC]	Lorentzian	Area	Center [eV]	Energy gap [eV]	Adjust quality R-factor
Bulk WO_3	25	Peak 1	19.69	10206.34	4.4 ±0.1	0.00059
		Peak 2	13.13	10210.74		
WO_3/SiO_2	25	Peak 1	20.39	10206.36	4.2 ±0.1	0.00037
		Peak 2	13.6	10210.59		
	700	Peak 1	17.85	10206.31	2.8 ±0.2	0.00021
		Peak 2	11.9	10209.13		
	750	Peak 1	17.8	10206.25	2.9 ±0.2	0.00017
		Peak 2	11.87	10209.11		
	800	Peak 1	18.64	10206.26	3.0 ±0.2	0.00028
		Peak 2	12.43	10209.22		
Bulk Na_2WO_4	25	Peak 1	11.03	10206.74	1.6 ±0.1	0.0002
		Peak 2	16.55	10208.34		
Na_2WO_4/SiO_2	25	Peak 1	12.34	10206.26	1.9 ±0.2	0.00050
		Peak 2	18.52	10208.19		
	700	Peak 1	11.78	10206.4	1.5 ±0.2	0.00074
		Peak 2	17.68	10207.88		
	750	Peak 1	11.66	10206.39	1.6 ±0.2	0.00061
		Peak 2	17.49	10207.98		
	800	Peak 1	12.42	10206.38	1.6 ±0.1	0.00051
		Peak 2	18.63	10207.94		
Mn-Na_2WO_4/SiO_2	25	Peak 1	12.25	10206.63	1.8 ±0.2	0.00016
		Peak 2	18.35	10208.45		
	700	Peak 1	12.86	10206.26	2.4 ±0.2	0.00023
		Peak 2	19.29	10208.61		
	750	Peak 1	13.09	10206.34	2.2 ±0.2	0.00051
		Peak 2	19.64	10208.53		
	800	Peak 1	13.05	10206.33	2.2 ±0.2	0.00041
		Peak 2	19.57	10208.51		

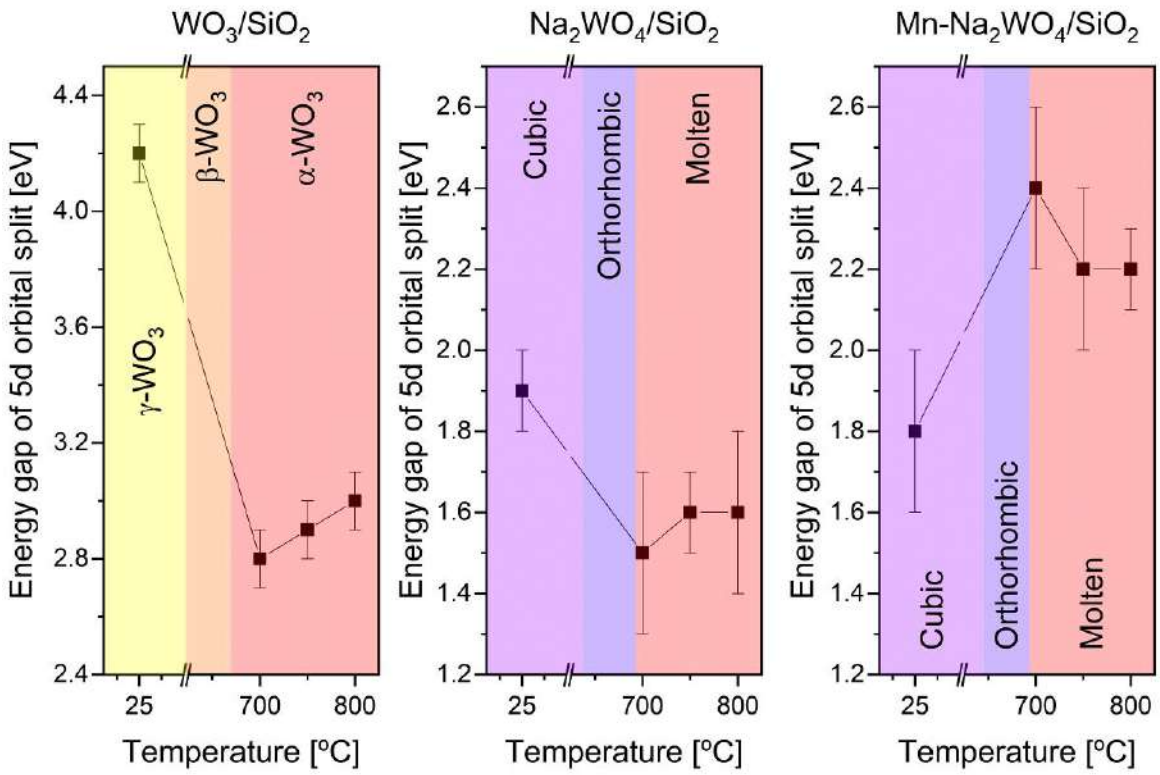

Figure 4.12 Energy gap of the 5*d* split orbitals at the W-L_3 edge (XANES) as a function of temperature for the WO_3/SiO_2, Na_2WO_4/SiO_2, and Mn-Na_2WO_4/SiO_2 catalysts.

The energy gap for the bulk WO_3 and Na_2WO_4 reference materials at room temperature is 4.4 and 1.6 eV, respectively (Table 4.3), in agreement with the literature (LIMAYE *et al.*, 2014, YAMAZOE *et al.*, 2008). Thus, the O_h-W sites exhibit a larger splitting of the W 5*d* state than the T_d-W sites, as discussed before. Regarding the general decrease of this parameter observed with temperature, some works attribute the decrease in the energy gap to an increase in the distortion degree of the O_h- and T_d-W sites (GARCÍA-LÓPEZ *et al.*, 2019, YAMAZOE *et al.*, 2008). In the WO_3/SiO_2 catalyst, the temperature-induced phase transitions of the crystalline WO_3 phase observed in our *in situ* TPO-XRD and -Raman studies suggest changes in the distortion degree of the O_h-W sites. The transition from the distorted monoclinic γ-WO_3 phase at room temperature to the ideal undistorted cubic WO_3 phase at very high temperatures (~ 1500 ºC) in the sequence γ (monoclinic) → β (orthorhombic) → α (tetragonal) → (cubic) is associated with changes in the W-O bond length, octahedral tilt, and/or displacement of the W atom out of the center of the octahedron (VOGT *et al.*, 1999, WANG, Y. C. *et al.*, 2016). The literature recognizes that the tetragonal α-WO_3 phase is less distorted than the monoclinic γ-WO_3 system because it presents lower tetrahedron tilting and W displacement from the octahedra center (VOGT *et al.*, 1999). However,

Wang *et al.* recently observed that the distortion imposed on the O_h-W sites by doping WO_3 with Rb atoms resulted in a larger W-O bond in the z-axis (WANG, Y. C. *et al.*, 2016). Therefore, the decrease in the energy gap observed throughout the $\gamma \rightarrow$ α-WO_3 phase transition can be explained by the elongation of the W-O bond in the z-axis.

The energy gap of the T_d-W^{6+} sites narrows after the Na_2WO_4 melting (> 698 ºC) in the Na_2WO_4/SiO_2 catalyst and widens in the Mn-Na_2WO_4/SiO_2 catalyst. Thus, although both catalysts have equal T_d-symmetry, the T_d-W sites on the Mn-Na_2WO_4/SiO_2 exhibit a wider energy gap (2.2 *vs.* 1.6 eV at 800 ºC, respectively), and therefore, a lower distortion degree. After comparing the chemical, textural, and structural properties of these catalysts, one can observe that the exclusive presence of the O_h-Mn^{3+} sites in the molten Na_2WO_4 phase is related to the lower distortion degree of the T_d-W sites. Recent studies have shown that the Na^+ and WO_4^{2-} ions are unstable, mobile, and interact with other materials after the Na_2WO_4 melting (VAMVAKEROS *et al.*, 2020). Thus, the interaction between the O_h-Mn^{3+} and WO_4^{2-} ions (T_d-W^{6+} sites) will most likely be present on the catalyst surface wetted with the molten Na_2WO_4 phase.

To confirm the presence of the O_h-Mn^{3+} sites and fully understand the molecular and electronic structure of the Mn-Na_2WO_4/SiO_2 catalyst at real OCM reaction temperatures, we also performed *in situ* TPO-XANES at the Mn-K edge. Figure 4.13 depicts the XANES spectra at the Mn-K edge of the bulk MnO, Mn_3O_4, Mn_2O_3, and MnO_2 reference materials recorded at 25 ºC (Figure 4.13a) and the *in situ* TPO-XANES spectra at the Mn-K edge of the Mn-Na_2WO_4/SiO_2 catalyst at heating under oxidizing conditions (Figure 4.13b).

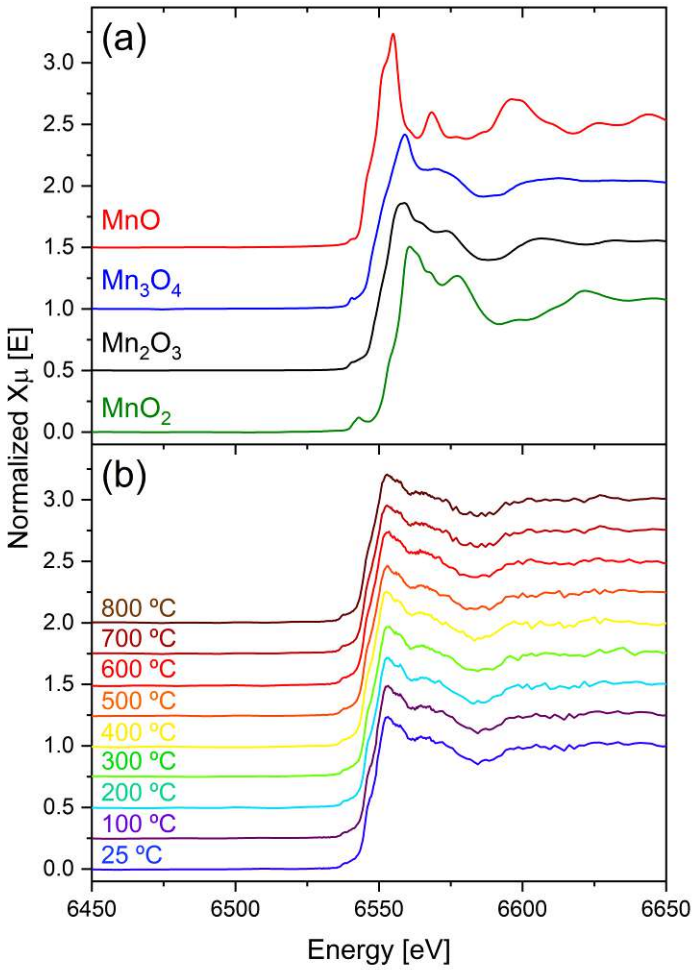

Figure 4.13 (a) XANES spectra at the Mn-K edge of the bulk MnO, Mn_3O_4, Mn_2O_3, and MnO_2 reference materials recorded at 25 ºC and (b) *In situ* TPO-XANES spectra at the Mn-K edge of the Mn-Na_2WO_4/SiO_2 catalyst recorded between 25 ºC and 800 ºC (10 ºC min^{-1}) flowing 10% O_2/He (10 cm^3 min^{-1}).

We can easily observe that the *in situ* TPO-XANES spectra at the Mn-K edge of the Mn-Na_2WO_4/SiO_2 catalyst resemble the spectra of bulk Mn_2O_3 reference material at 25 ºC. Although the *in situ* TPO-Raman spectra of the Mn-Na_2WO_4/SiO_2 catalyst exhibits a band related to the mixed-valent hausmanite $Mn^{2+}Mn^{3+}{}_2O_4$ phase, the Mn^{3+} sites dominate the XANES spectrum. At heating, the Mn-K edge XANES spectra of the Mn-Na_2WO_4/SiO_2 catalyst keep almost unchanged, showing that the Mn atoms are mostly present as O_h-Mn^{3+} sites at relevant OCM temperatures, in agreement with the *in situ* TPO-XRD findings elsewhere and the literature (VAMVAKEROS *et al.*, 2020). Therefore, the O_h-Mn^{3+} and T_d-W^{6+} electronic states are the most likely cation configuration of the Mn and W sites on the conventional Mn-Na_2WO_4/SiO_2 catalyst under real OCM reaction temperatures, just before methane admission into the reactor.

4.2 Steady-State OCM Catalytic Tests

Because the most dramatic structural variations under oxidizing conditions of the T_d-W^{6+} sites were observed above 650 ºC, the steady-state OCM catalytic tests were performed at 650, 700, 750, and 800 ºC. Figure 4.14 depicts the steady-state OCM performance in terms of methane conversion (X_{CH4}) and selectivity to C_2 hydrocarbons (S_{C2}) of the WO_3/SiO_2, Na_2WO_4/SiO_2, and Mn-Na_2WO_4/SiO_2 catalysts and the blank test (an empty reactor with no catalyst under the same conditions), together with the phase transitions of W sites evidenced by the *in situ* TPO-XRD analysis.

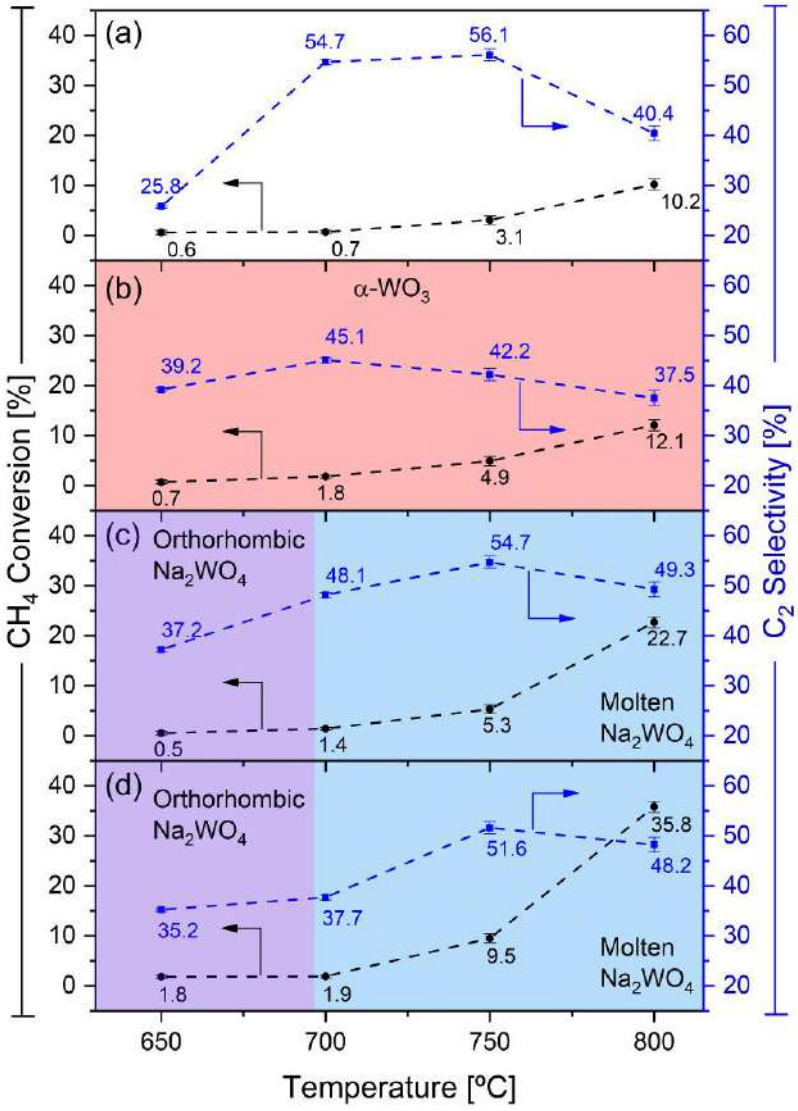

Figure 4.14 Steady-state OCM performance tests using: (a) an empty reactor without catalyst (blank test) and the (b) WO_3/SiO_2, (c) Na_2WO_4/SiO_2, and (d) Mn-Na_2WO_4/SiO_2 catalysts. Results acquired at 650, 700, 750, and 800 ºC flowing 100 $cm^3\,min^{-1}$ of a mixture CH_4:O_2:He:N_2 (molar ratio 2:1:2:0.5) through ~ 0.1 g of catalyst diluted with 0.4 g of carborundum (180 – 250 μm).

The blank test (*i.e.*, homogeneous reactions) is selective, albeit not very active; the presence of catalytic materials affords higher conversions, being selectivity dependent on the specific catalyst composition. At 650 ºC, all catalysts exhibit higher S_{C2} and similar X_{CH4} than the blank test (X_{CH4} = 0.6% and S_{C2} = 25.8%), excluding the Mn-Na_2WO_4/SiO_2 catalyst that exhibits a X_{CH4} = 1.8%, which is out of the error in the conversion data at this temperature (~ ± 0.4%). At 700 ºC, the S_{C2} in the blank test increases to 54.7%, but the X_{CH4} remains almost negligible (0.7%), Figure 4.14a; the WO_3/SiO_2 and Na_2WO_4/SiO_2 catalysts exhibit an increase in X_{CH4} (1.8 and 1.4%, respectively) and S_{C2} (45.1 and 48.1%, respectively), Figure 4.14b-c; and the Mn-Na_2WO_4/SiO_2 catalyst exhibits a slight increase in S_{C2} (37.7%), while the X_{CH4} remains unchanged (1.9%), Figure 4.14d. The S_{C2} of the WO_3/SiO_2 and Na_2WO_4/SiO_2 catalysts is lower than in the homogeneous reactions due to the higher X_{CH4}, leading to sequential reactions towards undesired but more thermodynamically stable CO_x compounds (FARRELL *et al.*, 2016). The X_{CH4} of the Mn-Na_2WO_4/SiO_2 and Na_2WO_4/SiO_2 catalysts are similar (within the experimental error at this temperature, ~ ± 0.3%), but the S_{C2} of the Na_2WO_4/SiO_2 catalyst is significantly higher.

As the temperature reaches 750 ºC, the blank test shows an increase in both X_{CH4} (3.1%) and S_{C2} (56.1%), Figure 4.14a; the WO_3/SiO_2 catalyst shows an increase in X_{CH4} (4.9%) and a decrease in S_{C2} (42.2%), Figure 4.14b; and the Na_2WO_4/SiO_2 and Mn-Na_2WO_4/SiO_2 catalysts exhibit an increase in both X_{CH4} (5.3 and 9.5%, respectively) and S_{C2} (54.7 and 51.6%, respectively), Figure 4.14c-d. The use of the WO_3/SiO_2 catalyst, compared to the blank test, results in a slightly higher X_{CH4} (from 3.1% to 4.9%) but a dramatic decrease in S_{C2} (from 56.1% to 42.2%). Thus, the WO_3/SiO_2 sample is a poorly selective OCM catalyst, in agreement with the literature (WU & LI, 1995). Certainly, the octahedral coordination (O_h) of the W^{6+} sites in the crystalline WO_3 phase has been associated with deep oxidation reactions. This feature is even more evident at 800 ºC (*i.e.*, at higher X_{CH4}), Figure 4.14b. Finally, all the catalysts and the blank test show higher X_{CH4} and lower S_{C2} at 800 ºC. The Na_2WO_4/SiO_2 and Mn-Na_2WO_4/SiO_2 catalysts exhibit a similar S_{C2} (49.3 and 48.2%, respectively), within experimental error at this temperature (~ ± 1.2%), but the X_{CH4} of the Mn-Na_2WO_4/SiO_2 is significantly higher (35.8% *vs.* 22.7%).

Note that the Mn-Na_2WO_4/SiO_2 catalyst exhibits higher X_{CH4} than Na_2WO_4/SiO_2 at all the evaluated temperatures. The only structural difference between these materials is the lower distortion degree of the T_d-W^{6+} sites on the Mn-Na_2WO_4/SiO_2 catalyst that

is caused by the presence of the O_h-Mn^{3+} sites. Thus, the distortion degree of the T_d-W^{6+} sites is related to their activity to convert methane at steady-state OCM reaction conditions. However, we cannot rule out the potential participation of the sites O_h-Mn^{3+} sites in the methane activation.

The direct correlation of the catalyst structure elucidated at heating under oxidation conditions (just before feeding methane into the reactor) with its OCM performance at steady-state (flowing $CH_4 + O_2$) should be made considering the potential effect of the methane flow on the T_d-W^{6+} and O_h-Mn^{3+} sites structure. Indeed, the Mn-Na_2WO_4/SiO_2 catalyst performs OCM at *i*) steady-state (flowing $CH_4 + O_2$) over several hours on stream by $W^{6+}\leftrightarrow W^{5+/4+}$ and $Mn^{2+}\leftrightarrow Mn^{3+}$ redox cycles (JIANG *et al.*, 1997, WU *et al.*, 1995) or *ii*) transient state (flowing CH_4) via Mars-van Krevelen mechanism by involving lattice oxygen (FLEISCHER *et al.*, 2016, KIANI *et al.*, 2019, LOMONOSOV & SINEV, 2016). Deep catalyst reduction/deactivation caused by several hours of stream in the steady-state operation or lattice oxygen depletion in the transient operation leads to the formation of the crystalline $MnWO_4$ phase, which presents O_h-Mn^{2+} and O_h-W^{6+} sites (*i.e.*, wolframite structure) (WANG, Pengwei ZHAO WANG *et al.*, 2017, WERNY *et al.*, 2020). Very high temperatures and reducing conditions (*i.e.*, high CH_4/O_2 molar ratios) accelerate the $MnWO_4$ phase formation (WANG, Pengwei ZHAO WANG *et al.*, 2017).

The T_d-W^{6+} and O_h-Mn^{3+} sites observed at temperatures above 650 ºC under oxidizing conditions are expected to be also present in the evaluated steady-state OCM operation (flowing $CH_4 + O_2$) because *i*) catalyst reduction/deactivation (associated with $MnWO_4$ formation) is slower than the catalyst re-oxidation at the evaluated temperatures (GORDIENKO *et al.*, 2016), *ii*) the CH_4/O_2 ratio used was low (*i.e.*, 2), *iii*) the Mn_2O_3 phase has been observed during *operando* OCM studies even at CH_4/O_2 ratios as high as 10 (WANG, Pengwei ZHAO WANG *et al.*, 2017), and *iv*) the Mn-Na_2WO_4/SiO_2 catalyst has been reported to be stable for extended time on stream (450 − 1000 h) under $CH_4 + O_2$ flow (KIANI *et al.*, 2019). However, the catalyst structure should be also characterized at *operando* conditions (at steady-state and dynamic operation) to ensure the stability of the characterized catalyst structure during OCM. The catalyst structure elucidated at *operando* conditions is presented in the next chapter.

4.3 Concluding Remarks

The structure of the Mn-Na_2WO_4/SiO_2 catalyst is highly dynamic, thus associating its OCM performance with crystalline phases identified at ambient temperature is inadequate. *In situ* TPO-XRD analysis shows that the crystalline phases identified at ambient conditions in the Mn-Na_2WO_4/SiO_2, Mn-free Na_2WO_4/SiO_2, and Mn- and Na-free WO_3/SiO_2 catalysts do not exist at relevant OCM temperatures (> 650 ºC). The $\gamma \rightarrow \beta \rightarrow \alpha$-$WO_3$, $\alpha \rightarrow \beta$-cristobalite, and cubic → orthorhombic → molten Na_2WO_4 phase transitions occur at heating under oxidizing conditions. *In situ* TPO-Raman study shows that the O_h-W^{6+} sites in the WO_3/SiO_2 catalyst and the T_d-W^{6+} sites in the Na_2WO_4/SiO_2 and Mn-Na_2WO_4/SiO_2 catalysts undergo significant structural changes during such phase transitions, as evidenced by the shift of the symmetric stretching (ν_s) vibration band. The ν_s vibration band shift suggests variations in the bond order of the W sites by changes in their oxidation state and/or distortion degree. *In situ* TPO-XANES spectra at the W-L_3 edge indicate that the ν_s vibration band shift is due to changes in the distortion degree instead of in the oxidation state, which remains unchanged (mainly W^{6+} valence) for all catalysts at heating. Additionally, *in situ* TPO-XANES spectra at the Mn-K edge confirm the presence of O_h-Mn^{3+} sites in Mn-Na_2WO_4/SiO_2 catalyst even at relevant OCM temperatures (> 650 ºC), which reduce the distortion degree of the T_d-W^{6+} sites in the molten Na_2WO_4 phase. Steady-state OCM tests show that the O_h-W^{6+} sites are inactive for OCM and the presence of the O_h-Mn^{3+} sites, and thus less distorted T_d-W^{6+} sites, makes the Mn-Na_2WO_4/SiO_2 catalyst more reactive towards methane activation. The presence of the T_d-W^{6+} and O_h-Mn^{3+} sites at real OCM reaction conditions (under an OCM gas mixture and at high temperatures, > 650 ºC) is studied in the next chapter.

Chapter 5

"No se trata sólo de operando, sino también de cooperando" – Miguel A. Bañares

Catalyst structure in *operando* conditions

5.1 Results and Discussion

Once catalyst structure was elucidated at heating under oxidizing conditions, it was also inspected under methane flow, mimicking the genuine OCM reaction conditions at transient and steady states. This is critical to understand the nature of the W and Mn sites and establish their structure-activity relationship for OCM since methane flow can introduce variations on their symmetry and oxidation state. In this chapter, only the Na_2WO_4/SiO_2 and Mn-Na_2WO_4/SiO_2 catalysts were studied because the WO_3/SiO_2 catalyst was observed to be inactive and unselective for OCM in the steady-state tests.

5.1.1 *Operando* TPRX-Raman Study

The catalyst structure is monitored at heating under an OCM gas mixture (CH_4:O_2:Ar = 2:1:4) to observe if methane flow modifies the behavior previously observed in the *in situ* TPO-Raman study. In this chapter, *operando* temperature-programmed reaction (TPRX) XRD analysis was not conducted because of limitations in the equipment. Fortunately, crystalline phases measurables by XRD along with dispersed, amorphous, and molten phases can be followed by Raman spectroscopy, as discussed elsewhere. Figure 5.1 shows the *operando* TPRX-Raman spectra of the (a) Na_2WO_4/SiO_2 and (b) Mn-Na_2WO_4/SiO_2 catalysts along with their contour surface (c and d, respectively) and simultaneous MS spectra for main products (e and f, respectively). The spectra were recorded from 25 to 800 ºC (10 ºC min^{-1}) and normalized against the Rayleigh band at 0 cm^{-1}, in agreement with the literature (WEI *et al.*, 2018). Before collecting the *operando* TPRX-Raman spectra, each catalyst was dehydrated under 50 cm^3 min^{-1} of O_2:Ar (molar ratio 1:2) at 200 ºC (10 ºC min^{-1}) for 30 min and then cooled down to 25 ºC under the same oxidizing flow.

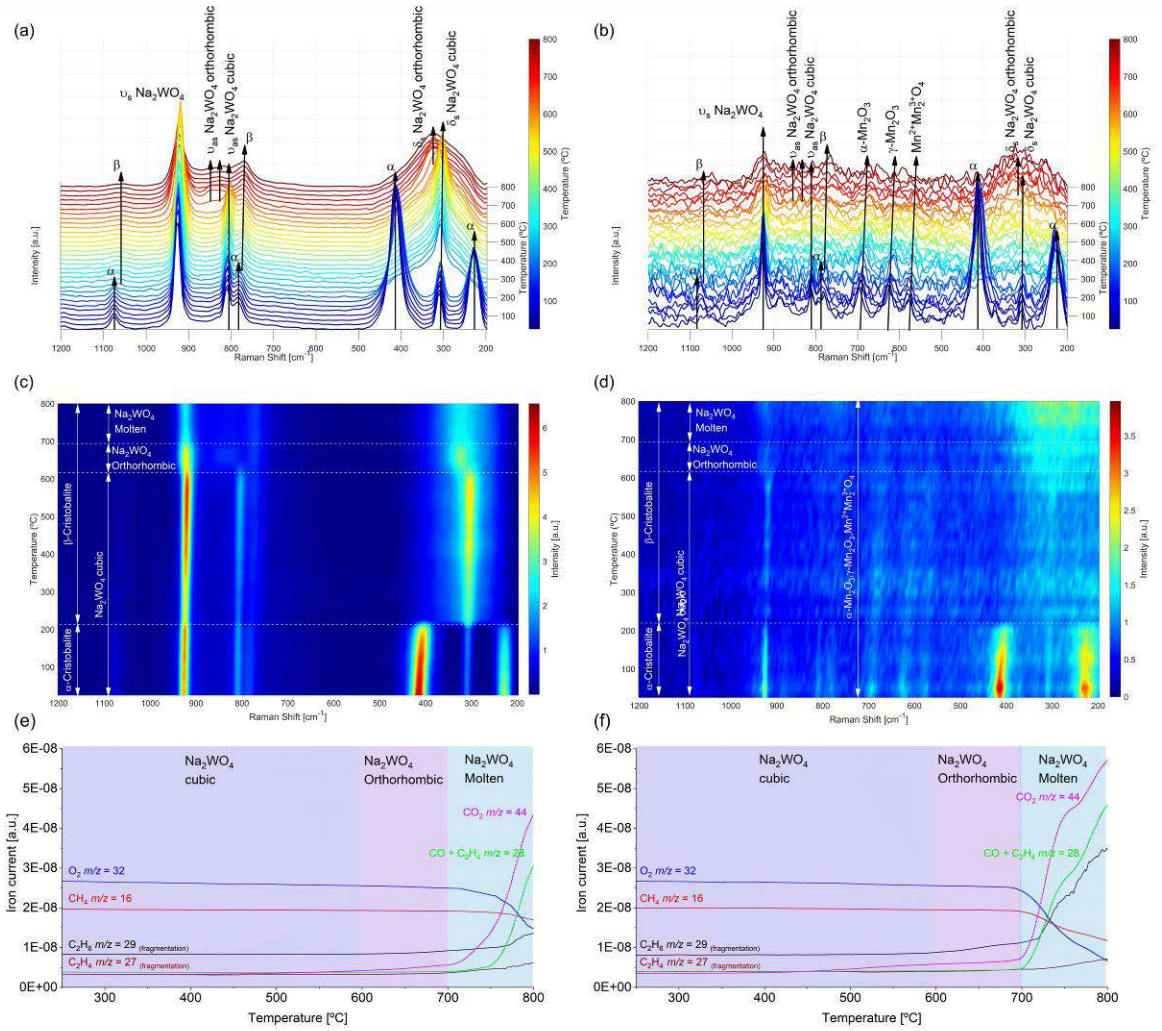

Figure 5.1 *Operando* TPRX-Raman spectra (excitation at 405 nm, normalization against Rayleigh band at 0 cm^{-1}) of the Na_2WO_4/SiO_2 (a) and Mn-Na_2WO_4/SiO_2 (b) catalysts along with their contour surface (c and d, respectively) and simultaneous MS spectra for main products (e and f, respectively) recorded between 25 and 800 ºC (10 ºC min^{-1}) under 50 cm^3 min^{-1} of CH_4:O_2:Ar (2:1:4).

At room temperature, the spectra in flowing O_2:Ar and CH_4:O_2:Ar (before heating) are equal, and only the last is evident in Figure 5.1a-b. The dehydrated Na_2WO_4/SiO_2 and Mn-Na_2WO_4/SiO_2 catalysts exhibit Raman bands related to the crystalline α-cristobalite and cubic Na_2WO_4 phases. The α-cristobalite phase gives rise to Raman bands at 1075, 785, 415, and 228 cm^{-1} (BATES, 1972) and the cubic Na_2WO_4 phase exhibits Raman bands at 926, 810, and 309 cm^{-1} (HARDCASTLE & WACHS, 1995). Dispersed WO_x species were not observed, in agreement with the literature (WERNY *et al.*, 2020). The Mn-Na_2WO_4/SiO_2 catalyst exhibits additional Raman bands at 698, 624, and 564 cm^{-1} related to the crystalline α-Mn_2O_3, γ-Mn_2O_3, and hausmanite $Mn^{2+}Mn^{3+}{}_2O_4$ phases, respectively (Figure 5.1b) (BUCIUMAN *et al.*, 1999, DATA & REFERENCES, 2009).

The structural evolution of the Na_2WO_4/SiO_2 and Mn-Na_2WO_4/SiO_2 catalysts at heating under an OCM gas mixture (CH_4:O_2:Ar) is similar to that previously observed in the *in situ* TPO-Raman study (Chapter 4). The α-cristobalite transforms into β-cristobalite near 200 ºC, exhibiting Raman bands at 1073, 782, and 292 cm^{-1}, which remain constant until 800 ºC (Figure 5.1c-d) (BATES, 1972). The δ_s vibration band of the cubic Na_2WO_4 phase (~ 309 cm^{-1}) overlaps the β-cristobalite band at 292 cm^{-1} after the phase transition (KIANI *et al.*, 2020). The cubic Na_2WO_4 phase transforms to orthorhombic Na_2WO_4 near 600 ºC, exhibiting Raman bands at 923, 847, 820, and 319 cm^{-1} (Figure 5.1c-d) (LIMA *et al.*, 2011, WANG, Jian *et al.*, 2018). Such bands lose intensity with a further temperature increase, suggesting the melting of the Na_2WO_4 phase near 700 ºC. Finally, Raman bands associated with the α-Mn_2O_3, γ-Mn_2O_3, and hausmanite $Mn^{2+}Mn^{3+}{}_2O_4$ phases on the Mn-Na_2WO_4/SiO_2 catalyst remain stable at heating (Figure 5.1d). Therefore, molten Na_2WO_4 and Mn_2O_3 phases with T_d-W^{6+} and O_h-Mn^{3+} sites, respectively, are present at real OCM reaction conditions.

The simultaneous MS spectra of the *operando* TPRX-Raman study show the formation of selective (C_2H_6 and C_2H_4) and combustion (CO and CO_2) products from methane conversion over both catalysts at heating. Methane starts to react near 550 ºC, forming CO_2 (*m/z* = 44) and C_2H_6 (*m/z* = 29). At 700 ºC, methane and oxygen conversion become more evident, selective products (C_2H_6 (*m/z* = 29) and C_2H_4 (*m/z* = 27)) appear, and combustion products (CO (*m/z* = 28) and CO_2 (*m/z* = 44)) exhibit a steeper increase. Note that the MS spectra for the Mn-Na_2WO_4/SiO_2 catalyst show a stronger drop feature of the *m/z* = 16 signal than the Na_2WO_4/SiO_2 catalyst, which suggests a higher methane conversion, in agreement with steady-state OCM results previously discussed in Chapter 4.

The environmental conditions (oxidizing, reducing, or inert flow) have been reported to drastically change the Mn-Na_2WO_4/SiO_2 catalyst structure during activation and reaction (WANG *et al.*, 2017, WERNY *et al.*, 2020). In this regard, methane flow would transform T_d-W^{6+} and O_h-Mn^{3+} sites of the Na_2WO_4 and Mn_2O_3 phases, respectively, into O_h-W^{6+} and O_h-Mn^{2+} of the $MnWO_4$ phase (*i.e.*, wolframite structure) (VAMVAKEROS *et al.*, 2020, WERNY *et al.*, 2020). However, this phase was not observed during the *operando* TPRX-Raman study due to the simultaneous CH_4 + O_2 feeding. Indeed, the $MnWO_4$ phase formation occurs by the deep reduction/deactivation of the catalyst (GORDIENKO *et al.*, 2016), which is slower than its oxidation (GORDIENKO *et al.*, 2016) at typical high OCM reaction temperatures.

5.1.2 *Operando* XANES spectroscopy.

The electronic structure of the W and Mn sites was also verified at steady-state and 800 ºC by XANES spectroscopy. Figure 5.2 shows the XANES spectra at the W-L_3 edge of the bulk Na_2WO_4 and WO_2 reference materials with known W oxidation state (6+ and 4+, respectively) recorded at 25 ºC and the *operando* (CH_4 + O_2)-XANES spectra at the W-L_3 edge of the Na_2WO_4/SiO_2 and Mn-Na_2WO_4/SiO_2 catalysts performing OCM at steady-state and 800 ºC.

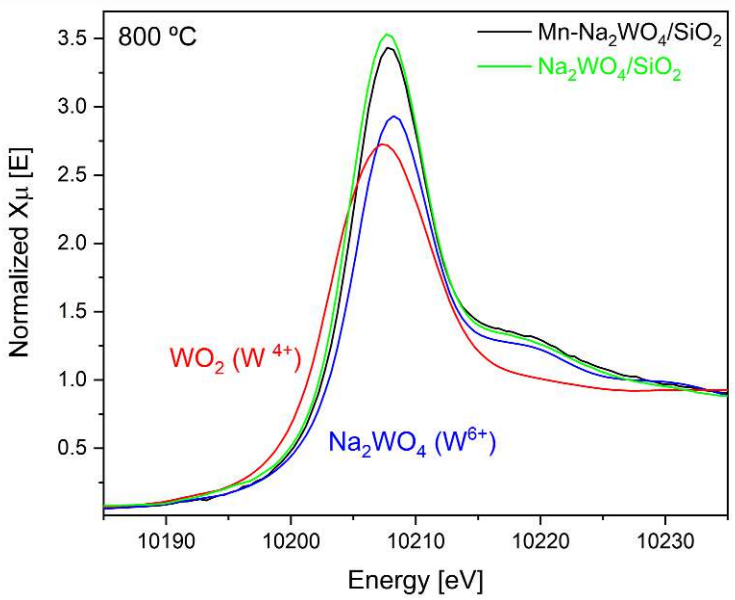

Figure 5.2 *Operando* (CH_4 + O_2)-XANES spectra at the W-L_3 edge of the Na_2WO_4/SiO_2 and Mn-Na_2WO_4/SiO_2 catalysts at 800 ºC under an OCM mixture (20 cm^3 min^{-1} of 10% CH_4/He and 10 cm^3 min^{-1} of 10% O_2/He). XANES spectra at the W-L_3 edge of the bulk Na_2WO_4 (W^{6+}) and WO_2 (W^{4+}) reference materials recorded at 25 ºC are also included.

The mean oxidation state of the W sites was calculated following the methodology described in Chapter 4. The W-L_3 edge position measured for each catalyst was interpolated to a straight line between the W-L_3 edge positions recorded for the bulk Na_2WO_4 (W^{6+}) and WO_2 (W^{4+}) reference materials (Figure 4.9). Note that the *operando* (CH_4 + O_2)-XANES spectra were acquired after 30 min of operation to allow the system to reach the steady-state. The Na_2WO_4/SiO_2 and Mn-Na_2WO_4/SiO_2 catalysts present equal W-L_3 edge position (10205.1 eV) and therefore mean W oxidation state (5.6) at steady-state operation and 800 ºC. This suggests that both catalysts have W^{6+} sites with some electron polarons (*i.e.*, W^{5+} at a W^{6+} site). The presence of W^{5+} polarons is due to the oxygen-deficient nature of the W oxides rather than methane-induced reduction reactions since similar values of the W-L_3 edge position were previously calculated for the same catalysts under oxidizing conditions (Table 4.2).

The mean oxidation state of the Mn sites on the Mn-Na_2WO_4/SiO_2 catalyst was measured at steady-state and 800 ºC. Figure 5.3 shows the XANES spectra at the Mn-K edge of the bulk MnO, Mn_3O_4, Mn_2O_3, and MnO_2 reference materials recorded at 25 ºC and the *operando* ($CH_4 + O_2$)-XANES spectra at the Mn-K edge of the Mn-Na_2WO_4/SiO_2 catalyst performing OCM at steady-state and 800 ºC.

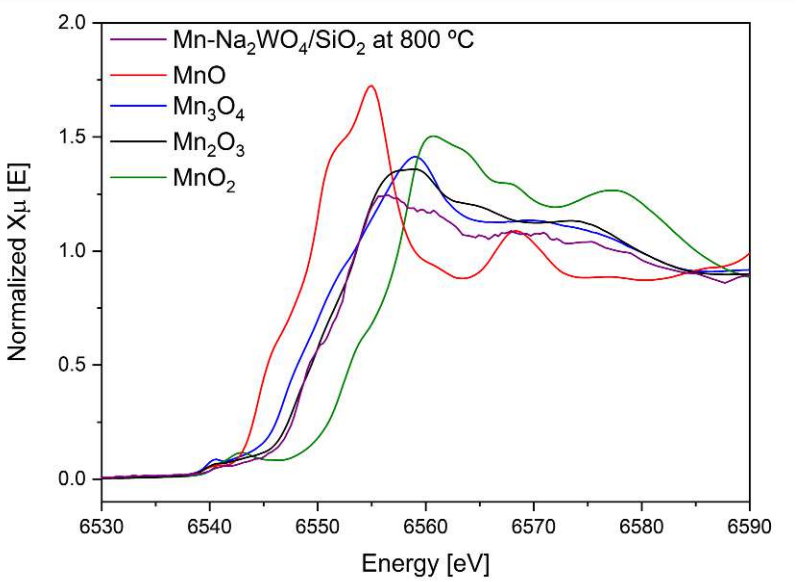

Figure 5.3 *Operando* ($CH_4 + O_2$)-XANES spectra at the Mn-K edge of the Mn-Na_2WO_4/SiO_2 catalyst at 800 ºC under an OCM mixture (20 $cm^3\ min^{-1}$ of 10% CH_4/He and 10 $cm^3\ min^{-1}$ of 10% O_2/He). XANES spectra at the Mn-K edge of the bulk MnO, Mn_3O_4, Mn_2O_3, and MnO_2 reference materials recorded at 25 ºC are included.

The *operando* ($CH_4 + O_2$)-XANES spectrum at the Mn-K edge of the Mn-Na_2WO_4/SiO_2 catalyst resembles the XANES spectrum of the bulk Mn_2O_3 reference material at 25 ºC. Furthermore, the Mn-K edge position of the Mn sites on the catalyst and the bulk MnO, Mn_3O_4, Mn_2O_3, and MnO_2 reference materials was determined by using the intersection with the energy axis of the second derivative with respect to the energy of the normalized XANES curve. The Mn-Na_2WO_4/SiO_2 catalyst presents the same Mn-K edge position as the bulk Mn_2O_3 reference material at 6551 eV. Therefore, despite the presence of the mixed-valent hausmanite $Mn^{2+}Mn^{3+}{}_2O_4$ phase (Figure 5.1) and methane flow, the Mn^{3+} sites dominate the XANES spectrum.

After inspecting the *operando* TPRX-Raman and ($CH_4 + O_2$)-XANES spectra at transient and steady-state, respectively, we can state that the O_h-Mn^{3+} and T_d-W^{6+} sites are still present on the conventional Mn-Na_2WO_4/SiO_2 catalyst under real OCM reaction conditions (*i.e.*, under both CH_4 and O_2 flow). In this regard, we confirm that methane-induced reduction reactions are irrelevant for the catalyst structure at low CH_4/O_2 ratios, as hypothesized in the steady-state OCM catalytic tests in Chapter 4.

Because changes in the catalyst structure are appreciable only at very reducing conditions (*i.e.*, high CH_4/O_2 ratios) (WERNY *et al.*, 2020) or after several hours on stream (~ 450 − 1000 h) (KIANI *et al.*, 2019), we studied the catalyst structure only under methane flow. Note that the Mn-Na_2WO_4/SiO_2 catalyst can also perform OCM reactions only under methane flow by involving its lattice oxygen via Mars-van Krevelen mechanism (FLEISCHER *et al.*, 2016, KIANI *et al.*, 2019, LOMONOSOV & SINEV, 2016). In this regard, the reducibility of the T_d-W^{6+} and O_h-Mn^{3+} sites is a critical parameter since it participates in the methane activation, the rate-determining step of the OCM route, (KIANI *et al.*, 2019) via $W^{6+}\leftrightarrow W^{4+}$ or $W^{6+}\leftrightarrow W^{4+}$ and $Mn^{2+}\leftrightarrow Mn^{3+}$ redox cycles (JIANG et al., 1997, WU et al., 1995). Therefore, considering only the reduction reactions, we inspected the electronic structure of the W and Mn sites via XANES spectroscopy.

Figure 5.4 shows the *operando* CH_4-XANES spectra at the W-L_3 edge of the Na_2WO_4/SiO_2 and Mn-Na_2WO_4/SiO_2 catalysts after 30 min of reduction in 10% CH_4/He (10 cm^3 min^{-1}) at 700, 750, and 800 ºC and the XANES spectra at the W-L_3 edge of the bulk Na_2WO_4 and WO_2 reference materials with known W oxidation state (6+ and 4+, respectively) recorded at 25 ºC.

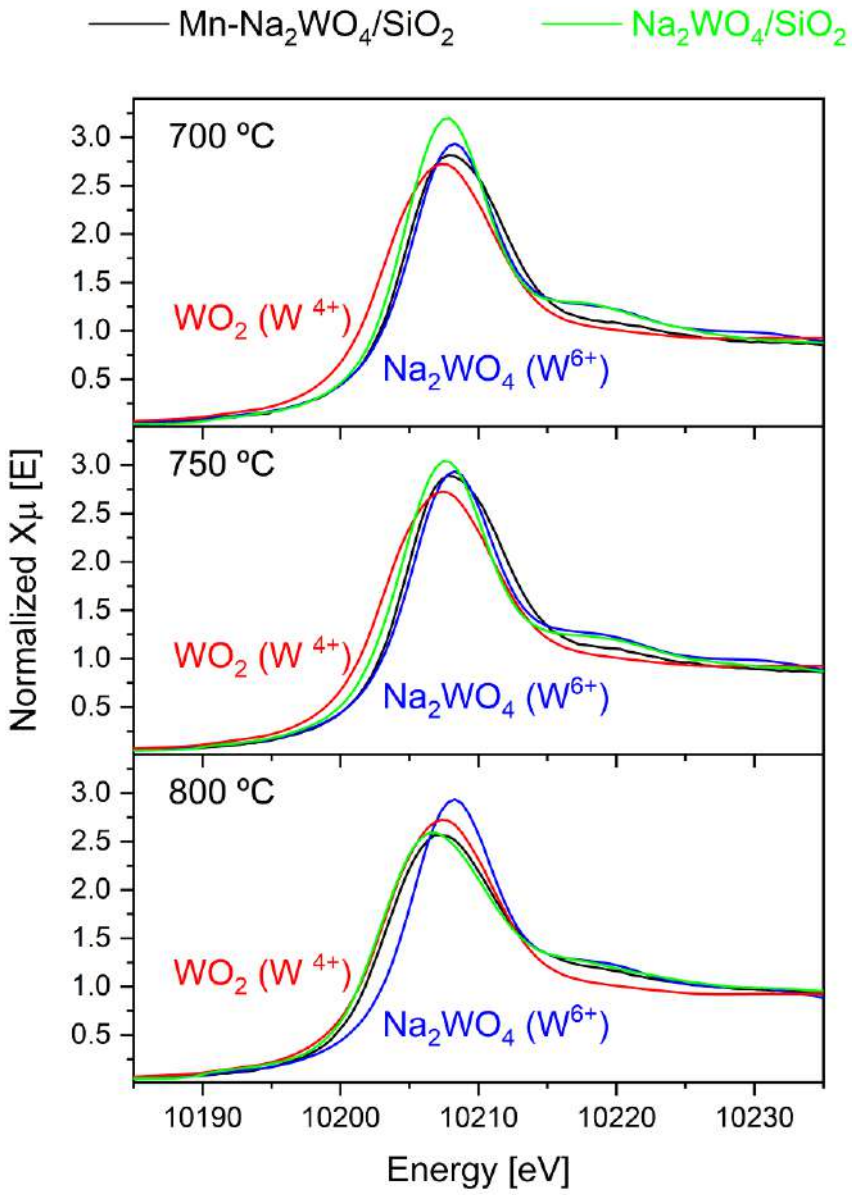

Figure 5.4 *Operando* CH_4-XANES spectra at the W-L_3 edge of the Na_2WO_4/SiO_2 and Mn-Na_2WO_4/SiO_2 catalysts recorded after 30 min of reduction in 10% CH_4/He (10 $cm^3\,min^{-1}$) at 700, 750, and 800 ºC. XANES spectra at the W-L_3 of the reference bulk Na_2WO_4 (W^{6+}) and WO_2 (W^{4+}) reference materials recorded at 25 ºC are included.

The CH_4-XANES spectra after 30 min of treatment of the Na_2WO_4/SiO_2 and Mn-Na_2WO_4/SiO_2 catalysts exhibit a white line with lower intensity than the spectra recorded at heating under oxidizing conditions (Figure 4.8) and steady-state OCM operation (Figure 5.2), suggesting the reduction of the mean W oxidation state. Indeed, the white line intensity is associated with the density of unoccupied 5*d* states and therefore with the mean W oxidation state. The quantification of the mean W oxidation state was conducted according to the zero-crossing of the second derivative (Figure 4.9) and the results are listed in Table 5.1.

Table 5.1 W-L_3 edge position according to the zero-crossing of the second derivative and mean W oxidation state obtained by interpolating the *operando* CH_4-XANES spectra at the W-L_3 edge of the Na_2WO_4/SiO_2 and Mn-Na_2WO_4/SiO_2 catalysts.

Temperature [ºC]	Na_2WO_4/SiO_2		Mn-Na_2WO_4/SiO_2	
	Edge position [eV]	Mean W oxidation state	Edge position [eV]	Mean W oxidation state
700	10204.7	5.3 ± 0.1	10204.9	5.4 ± 0.1
750	10204.7	5.3 ± 0.1	10204.7	5.3 ± 0.1
800	10203.4	4.1 ± 0.1	10203.4	4.1 ± 0.1

The W^{6+} sites on both catalysts exhibit a similar reduction degree, depending only on the temperature treatment. Therefore, the different OCM performance of the Na_2WO_4/SiO_2 and Mn-Na_2WO_4/SiO_2 is not associated with a different redox behavior of the W sites. On the other hand, the mean Mn oxidation state on the Mn-Na_2WO_4/SiO_2 catalyst was also measured. Figure 5.5 shows the *operando* CH_4-XANES spectra at the Mn-K edge of the Mn-Na_2WO_4/SiO_2 catalyst at 700,750, and 800 ºC and the XANES spectra at the Mn-K edge of the bulk MnO, Mn_3O_4, Mn_2O_3, and MnO_2 reference materials recorded at 25 ºC.

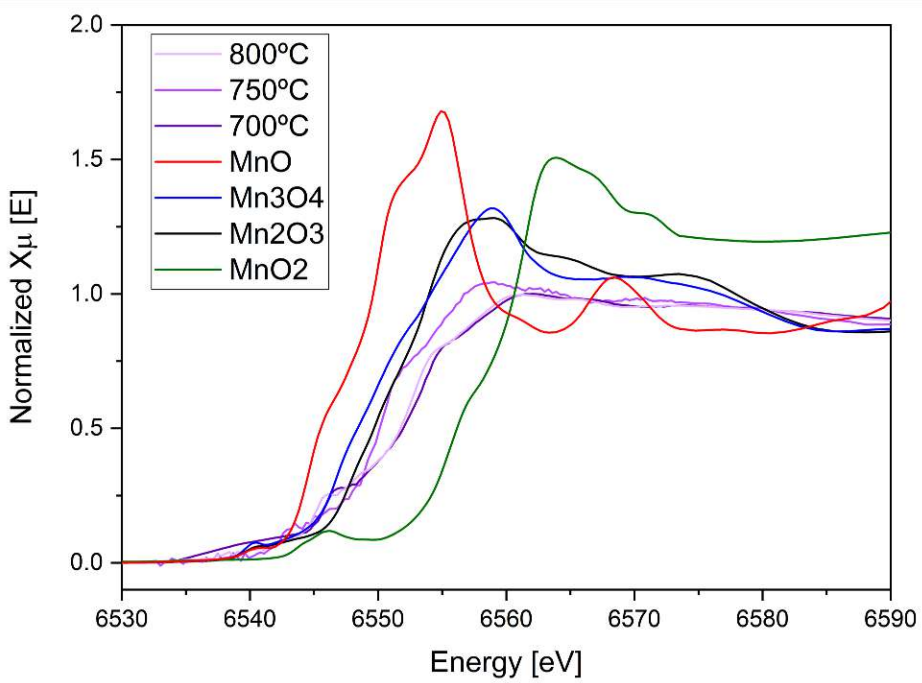

Figure 5.5 *Operando* CH_4-XANES spectra at the Mn-K edge of the Mn-Na_2WO_4/SiO_2 catalyst recorded after 30 min of reduction in 10% CH_4/He (10 $cm^3 min^{-1}$) at 700, 750, and 800 ºC. Spectra of the reference bulk Na_2WO_4 (W^{6+}) and WO_2 (W^{4+}) reference materials recorded at 25 ºC are included.

Although the *operando* CH_4-XANES spectra at the Mn-K edge of the Mn-Na_2WO_4/SiO_2 catalyst at 700, 750, and 800 ºC resemble the spectra of bulk Mn_2O_3 reference material at 25 ºC, they present variations on the edge position, suggesting a reduction in the mean Mn oxidation state. To calculate the mean oxidation state of the Mn sites on the Mn-Na_2WO_4/SiO_2 catalyst at each temperature, the Mn-K edge position measured for the Mn-Na_2WO_4/SiO_2 catalyst was interpolated to a straight line between the edge values recorded for the bulk MnO, Mn_2O_3, and MnO_2 reference materials, as shown in Figure 5.6. Table 5.2 summarizes the edge position and mean oxidation state of the Mn sites at 700, 750, and 800 ºC.

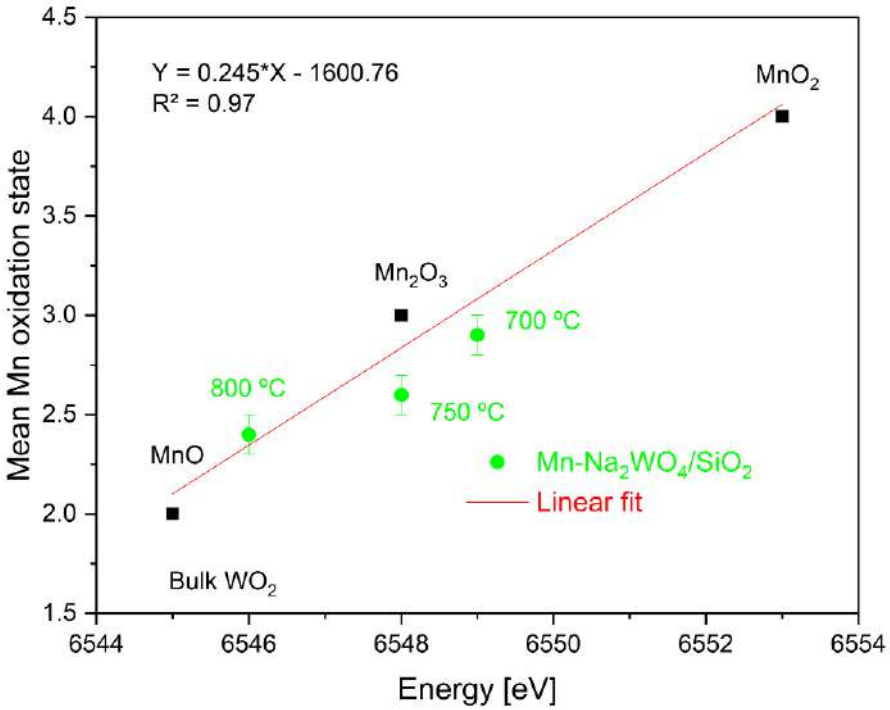

Figure 5.6 Energy positions at the Mn-K edge *vs.* mean oxidation state of Mn sites on the Mn-Na_2WO_4/SiO_2 catalyst and the bulk MnO, Mn_3O_4, Mn_2O_3, and MnO_2 reference materials.

Table 5.2 Mn-K edge position according to the zero-crossing of the second derivative and mean Mn oxidation state obtained by interpolating the *operando* CH_4-XANES spectra of the Mn-Na_2WO_4/SiO_2 catalysts at 700, 750, and 800 ºC.

Temperature [ºC]	Mn-Na_2WO_4/SiO_2	
	Edge position [eV]	Mean Mn oxidation state
700	6549	2.9 ± 0.1
750	6548	2.6 ± 0.1
800	6546	2.4 ± 0.1

The Mn^{3+} sites reduce as a function of the temperature treatment. Therefore, both T_d-W^{6+} and O_h-Mn^{3+} sites reduce in the presence of methane and are relevant for the OCM performance of the Mn-Na_2WO_4/SiO_2 catalyst. Note that the W and Mn sites reduction implies the lattice oxygen release during the methane activation. The involvement of the lattice oxygen from the W and Mn sites was evaluated by the TPR test, as shown in the next section.

5.1.3 TPR studies

The amount and reactivity of the lattice oxygen in the Na_2WO_4/SiO_2 and Mn-Na_2WO_4/SiO_2 catalysts were analyzed via temperature-programmed reduction (TPR) tests coupled to mass spectrometry (MS) using H_2 and CH_4 as chemical probing molecules. Figure 5.7 depicts the H_2-TPR-MS profile for each catalyst drawn using the *m/z* = 18 (H_2O) signal.

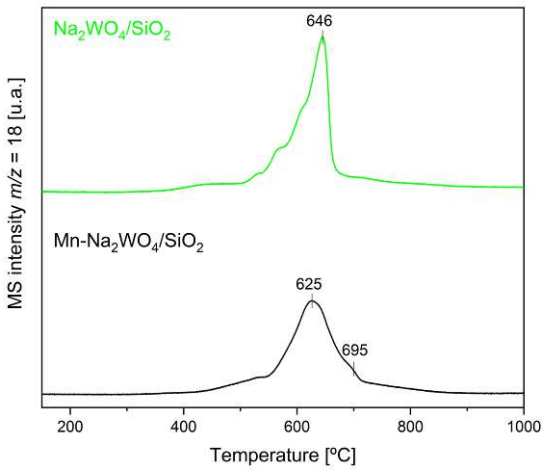

Figure 5.7 H_2-TPR-MS profiles of the Na_2WO_4/SiO_2 and Mn-Na_2WO_4/SiO_2 catalysts.

The lattice oxygen amount of the Na_2WO_4/SiO_2 and Mn-Na_2WO_4/SiO_2 catalysts is 339 and 365 µmolO_2 g_{cat}^{-1}, respectively. Thus, the W^{6+} sites would completely reduce to W^0 and the Mn^{3+} to $Mn^{2+/3+}$, as suggested in the literature (GORDIENKO *et al.*, 2016). The Na_2WO_4/SiO_2 catalyst exhibits a reduction peak at 646 ºC that is related to the reduction of the Na_2WO_4 crystallites. The Mn-Na_2WO_4/SiO_2 catalyst exhibits the reduction peak of the Na_2WO_4 crystallites at a lower temperature (625 °C) because it presents Na_2WO_4 crystallites with smaller sizes (375 *vs.* 533 nm), as shown in Appendix B. Additionally, the Mn-Na_2WO_4/SiO_2 catalyst exhibits a small reduction shoulder at ~ 700 °C attributed to the reduction of the Mn sites ($Mn^{3+} \rightarrow Mn^{2+/3+}$). The lattice oxygen reactivity of the Na_2WO_4/SiO_2 Mn-Na_2WO_4/SiO_2 catalysts was evaluated by CH_4-TPR-MS and the results are shown in Figure 5.8.

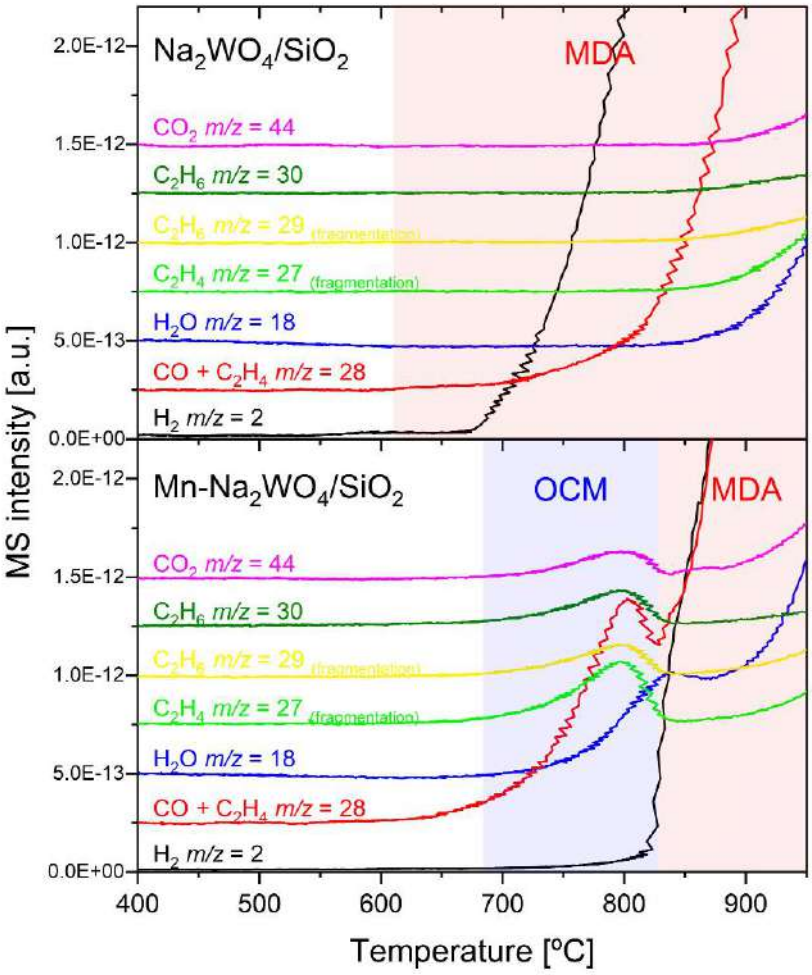

Figure 5.8 CH_4-TPR-MS patterns of the Na_2WO_4/SiO_2 and Mn-Na_2WO_4/SiO_2 catalysts.

The Na_2WO_4/SiO_2 catalyst reduces, exhibiting products of methane activation. CO (m/z = 28) and H_2 (m/z = 2) signals appear at 600 and 740 ºC, respectively, increasing sharply with temperature. Additionally, C_2H_6 (m/z = 30, 29); C_2H_4 (m/z = 27); H_2O (m/z = 18), and CO_2 (m/z = 44) signals appear above 850 ºC. Note that m/z = 28 signal is exclusively associated with CO (and not with C_2H_4) below 850 ºC because it does not correspond to the C_2H_4 fragmentation signal at m/z = 27. The oxygen in the combustion products (*i.e.*, CO and CO_2) comes from the lattice oxygen released during W^{6+} cations reduction. The high H_2 production is caused by the presence of W carbides formed from reduced $W^{6-\alpha}$ sites in the presence of methane. Indeed, silica-supported W metal and its carbides are known to catalyze non-oxidative methane conversion (GORDIENKO *et al.*, 2016, WECKHUYSEN *et al.*, 1998, ZENG *et al.*, 1998). Thus, H_2, C_2H_6, and C_2H_4 production results from methane dehydrogenation reactions, and therefore, the Na_2WO_4/SiO_2 catalyst is unable to perform OCM in the absence of gas-phase oxygen (SCHWACH *et al.*, 2017).

The Mn-Na_2WO_4/SiO_2 catalyst presents a two-step CH_4-TPR-MS pattern, in agreement with the literature (GORDIENKO *et al.*, 2016). Typical OCM products (C_2H_6 (*m/z* = 30, 29), C_2H_4 (*m/z* = 27, 28), and H_2O (*m/z* = 18)) are observed in the first step (700 - 820 ºC). Here, the *m/z* = 28 signal is associated not only with CO but also with C_2H_4, as suggested by the presence of the *m/z* = 27 signal. Products of non-oxidative methane conversion (CO (*m/z* = 28) and H_2 (*m/z* = 2)) are observed in the second step at temperatures above 820 ºC. The two-step CH_4-TPR-MS pattern has been associated in the literature with weakly- and strongly-bonded (lattice) oxygen, with the former being linking to the selective production of C_2 hydrocarbons (GORDIENKO *et al.*, 2016). However, the source of oxygen has not been completely elucidated as both T_d-W^{6+} and O_h-Mn^{3+} sites can reduce at relevant OCM reaction conditions.

5.2 Concluding Remarks

Operando TPRX-Raman spectra show that the structural evolution of the Na_2WO_4/SiO_2 and Mn-Na_2WO_4/SiO_2 catalysts at heating under an OCM gas mixture (CH_4 + O_2 +Ar) is equal to that previously observed in the *in situ* TPO-Raman study. The α→β-cristobalite and cubic→orthorhombic→molten-Na_2WO_4 phase transitions occur at heating. Furthermore, the catalyst structure remains stable performing OCM at 800 ºC and steady-state. *Operando* (CH_4+O_2)-XANES spectra at the W-L_3 and Mn-K edges confirm that the oxidation state of the W and Mn sites at steady-state and 800 ºC remains as 6+ and 3+, respectively. Flowing O_2 simultaneously with CH_4 is likely to avoid changes in the catalyst structure at steady-stable and heating. The lattice oxygen nature of the catalysts was evaluated at transient state. The Mn-Na_2WO_4/SiO_2 catalyst has two types of lattice oxygen: weakly and strongly bound, which react with methane at temperatures between 650-820 ºC and higher than 820 ºC, respectively. Mn is likely to be responsible for the presence of weakly bound structural oxygen, which is the only one that can selectively oxidize methane in the absence of gas-phase oxygen, forming typical OCM products. *Operando* CH_4-XANES spectroscopy shows that W sites reduce to the same degree on both Na_2WO_4/SiO_2 and Mn-Na_2WO_4/SiO_2 catalysts and the reduction of Mn sites on the last may be responsible for the selective formation of C_2 hydrocarbons.

Chapter 6

"*Chemistry is necessarily an experimental science: its conclusions are drawn from data, and its principles supported by evidence from facts*" - Michael Faraday

Conclusions

The structure of the Mn-Na_2WO_4/SiO_2 catalyst is highly dynamic and therefore the association of any OCM activity with crystalline phases observed at ambient temperature is inadequate. *In situ* TPO-XRD analysis shows that the crystalline phases identified on the Mn-Na_2WO_4/SiO_2, Mn-free Na_2WO_4/SiO_2, and Mn- and Na-free WO_3/SiO_2 catalysts at ambient conditions do not exist at relevant OCM temperatures (> 650 ºC). The γ → β → α-WO_3, α → β-cristobalite, and cubic → orthorhombic → molten Na_2WO_4 phase transitions occur at heating under oxidizing conditions. *In situ* TPO-Raman study shows that the O_h-W^{6+} sites in the WO_3/SiO_2 catalyst and the T_d-W^{6+} sites in the Na_2WO_4/SiO_2 and Mn-Na_2WO_4/SiO_2 catalysts undergo significant structural changes during such phase transitions, as evidenced by the shift of the symmetric stretching (ν_s) vibration band. The ν_s vibration band shift suggests variations in the bond order of the W sites by changes in their oxidation state and/or distortion degree. *In situ* TPO-XANES spectra at the W-L_3 edge indicate that the ν_s vibration band shift is due to changes in the distortion degree instead of in oxidation state, which remains unchanged (mainly W^{6+}) for all catalysts at heating. Additionally, *in situ* TPO-XANES spectra at the Mn-K edge confirm the presence of O_h-Mn^{3+} sites in Mn-Na_2WO_4/SiO_2 catalyst even at relevant OCM temperatures (> 650 ºC), which reduce the T_d-W^{6+} sites distortion in the molten Na_2WO_4 phase compared with the Na_2WO_4/SiO_2 catalyst. Steady-state OCM tests show that the O_h-W^{6+} sites are not active and the presence of the O_h-Mn^{3+} sites, and thus less distorted T_d-W^{6+} sites, makes the Mn-Na_2WO_4/SiO_2 catalyst more reactive towards methane activation.

Flowing CH_4 through the catalyst at high temperatures (> 650 ºC) has been reported to be responsible for the $MnWO_4$ phase formation, which presents O_h-W^{6+} and O_h-Mn^{2+} sites. *Operando* TPRX-Raman spectra show that the structural evolution of the Na_2WO_4/SiO_2 and Mn-Na_2WO_4/SiO_2 catalysts at heating under an OCM gas mixture (CH_4 + O_2 +Ar) is equal to that previously observed in the TPO-Raman study: the α-cristobalite transforms to β-cristobalite and the cubic Na_2WO_4 transforms to the

orthorhombic and then to molten Na_2WO_4. Furthermore, the catalyst structure remains stable performing OCM at 800 ºC and steady-state. *Operando* (CH_4+O_2)-XANES spectra at the W-L_3 and Mn-K edges confirm that the oxidation state of the W and Mn sites at steady-state remains as 6+ and 3+, respectively. Flowing O_2 simultaneously with CH_4 may avoid changes in the catalyst structure at steady-stable. The lattice oxygen nature of the catalysts was evaluated at transient state. The Mn-Na_2WO_4/SiO_2 catalyst has two types of lattice oxygen: weakly and strongly bound, which react with methane at temperatures between 650-820 ºC and higher than 820 ºC, respectively. Mn would be responsible for the presence of weakly bound structural oxygen, which is the only one that can selectively oxidize methane in the absence of gas-phase oxygen, forming typical OCM products. *Operando* CH_4-XANES spectroscopy shows that W sites reduce to the same degree on both Na_2WO_4/SiO_2 and Mn-Na_2WO_4/SiO_2 catalysts and the reduction of Mn sites on the last may be responsible for the selective formation of C_2 hydrocarbons.

Suggestions for Upcoming Works

Developing improved formulations of the Mn-Na_2WO_4/SiO_2 catalyst still requires a deep understanding of the Mn and W sites structure at real OCM reaction conditions and their catalytic participation in the CH_4 activation. In this regard, further studies should:

(i) To explain by computational works the lowering distortion effect of the Mn sites on the W sites in the molten Na_2WO_4 phase.

(ii) To elucidate the relevance of the W and Mn redox kinetics by correlating the rates of reduction, oxidation, and symmetry change the W and Mn sites with the rates of C_2 hydrocarbons formation using transient oxygen cutoff experiments (cycling between a mixture of CH_4:O_2:Ar and one of CH_4:Ar) and methane cutoff experiments (cycling between a mixture of CH_4:O_2:Ar and one of O_2:Ar) coupled with *operando* XAS measurements.

(iii) To establish the catalytic contribution of each supported oxide by determining simultaneously the steady-state OCM activity and the molecular and electronic structure of mono- (Mn/SiO_2, Na/SiO_2, W/SiO_2), bi- (Mn-Na/SiO_2, Mn-W/SiO_2, Na-W/SiO_2), and tri-metallic oxide Mn−W−Na/SiO_2 catalysts.

Appendix A

Thermodynamic calculations.

The thermodynamic limitations of the MDA and OCM routes were studied by determining the thermodynamic properties of a set of potential individual reactions that can occur as follows:

Potential reactions that can occur in the MDA route:

$$CH_{4(g)} \rightarrow 1/6\ C_6H_{6(g)} + 3/2\ H_{2(g)} \quad \Delta G_r^{25\,^{o}C} = 75\ kJ\ mol^{-1} \quad \Delta H_r^{25\,^{o}C} = 89\ kJ\ mol^{-1} \qquad (2.1)$$

$$CH_{4(g)} \rightarrow 1/10\ C_{10}H_{8(g)} + 8/5\ H_{2(g)} \quad \Delta G_r^{25\,^{o}C} = 75\ kJ\ mol^{-1} \quad \Delta H_r^{25\,^{o}C} = 90\ kJ\ mol^{-1} \qquad (2.2)$$

$$CH_{4(g)} \rightarrow 1/2\ C_2H_{6(g)} + 1/2\ H_{2(g)} \quad \Delta G_r^{25\,^{o}C} = 50\ kJ\ mol^{-1} \quad \Delta H_r^{25\,^{o}C} = 33\ kJ\ mol^{-1} \qquad (2.3)$$

$$CH_{4(g)} \rightarrow 1/2\ C_2H_{4(g)} + H_{2(g)} \quad \Delta G_r^{25\,^{o}C} = 85\ kJ\ mol^{-1} \quad \Delta H_r^{25\,^{o}C} = 101\ kJ\ mol^{-1} \qquad (2.4)$$

Potential reactions that can occur in the OCM route:

$$CH_{4(g)} + 1/4\ O_{2(g)} \rightarrow 1/2\ C_2H_{6(g)} + 1/2\ H_2O_{(g)} \qquad (A.1)$$

$$CH_{4(g)} + 1/2\ O_{2(g)} \rightarrow 1/2\ C_2H_{4(g)} + H_2O_{(g)} \qquad (A.2)$$

$$CH_{4(g)} + 3/2\ O_{2(g)} \rightarrow CO_{(g)} + 2\ H_2O_{(g)} \qquad (A.3)$$

$$CH_{4(g)} + 2\ O_{2(g)} \rightarrow CO_{2(g)} + 2\ H_2O_{(g)} \qquad (A.4)$$

The partial molal enthalpies are equal to the molal enthalpies of the pure components, neglecting any enthalpy changes on mixing. The molal enthalpy of a species i ($H_i(T)$) at a particular temperature T and pressure P is expressed in terms of enthalpy of formation of the species i ($H_i^o(T_r)$) at some reference temperature T_r plus the change in the enthalpy (ΔH_{Qi}) that results when the temperature is raised from the reference temperature T_r to some reaction temperature T as follows:

$$H_i(T) = H_i^o(T_r) + \Delta H_{Qi} \quad \text{(A.5)}$$

The $H_i^o(T_r)$ is usually reported at 298.15 K and is found in the literature (CHASE, 1998). For any substance *i* that is being heated from T_r to T in the absence of phase change, the change in the enthalpy (ΔH_{Qi}) is as follows:

$$\Delta H_{Qi} = \int_{T_r}^{T} C_{pi}\, dT \quad \text{(A.6)}$$

In which, C_{pi} is the heat capacity at constant pressure that is expressed as a function of temperature. For instance, for the ethylene, the heat capacity model in J mol^{-1} K^{-1} was taken from NIST library as follows:

$$C_{pi} = A + BT + CT^2 + DT^3 + E/T^2 \quad \text{(A.7)}$$

In which, the values of the A, B, C, D, and E constants of some availed species are reported in Table A.1:

Table A.1 Constants for Gas Phase Heat Capacity C_{pi}

Compound	Range (K)	A	B	C	D	E	F	G	H
CH_4	298-1300	-0.70	108.48	-42.52	5.86	0.68	-76.84	158.72	-74.87
CO	298-1300	25.57	6.10	4.05	-2.67	0.13	-118.01	227.37	-110.53
CO_2	298-1200	25.00	55.19	-33.69	7.95	-0.14	-403.61	228.24	-393.52
H_2O	100-1200	30.09	6.83	6.79	-2.53	0.08	-250.88	223.40	-241.83
O_2	700-2000	30.03	8.77	-3.99	0.79	-0.74	-11.32	236.17	0.00
	100-700	31.32	-20.24	57.87	-36.51	-0.01	-8.90	246.79	0.00
C_2H_4	298-1200	-6.39	184.40	-112.97	28.50	0.32	48.17	163.16	52.47
H_2	1000-2000	18.56	12.26	-2.86	0.27	1.98	-1.15	156.29	0.00
	298-1000	33.07	-11.36	11.43	-2.77	-0.16	-9.98	172.71	0.00
C	298-6000	21.18	-0.81	0.45	-0.04	-0.01	710.35	183.87	716.67

Once each molal enthalpy was availed at a determined temperature *T* of reaction, the heat of a certain reaction *r* at a temperature *T* (Equation A.8) is given in terms of the enthalpy of each species at temperature *T* as described in Equation A.9:

$$A + B \rightarrow C + D \quad \text{(A.8)}$$

$$\Delta H_r(T) = \left[\sum_i v_i H_i(T)\right]_{products} - \left[\sum_i v_i H_i(T)\right]_{reactives} \quad \text{(A.9)}$$

In which, $\Delta H_r(T)$ is the change in the enthalpy at a reaction temperature *T*, in a certain reaction *r* and v_i is the stoichiometric coefficient of the species *i*. The reaction enthalpy as a function of temperature for a set of potential reactions that can occur on the OCM route at 1 atm is presented in Figure A.1.

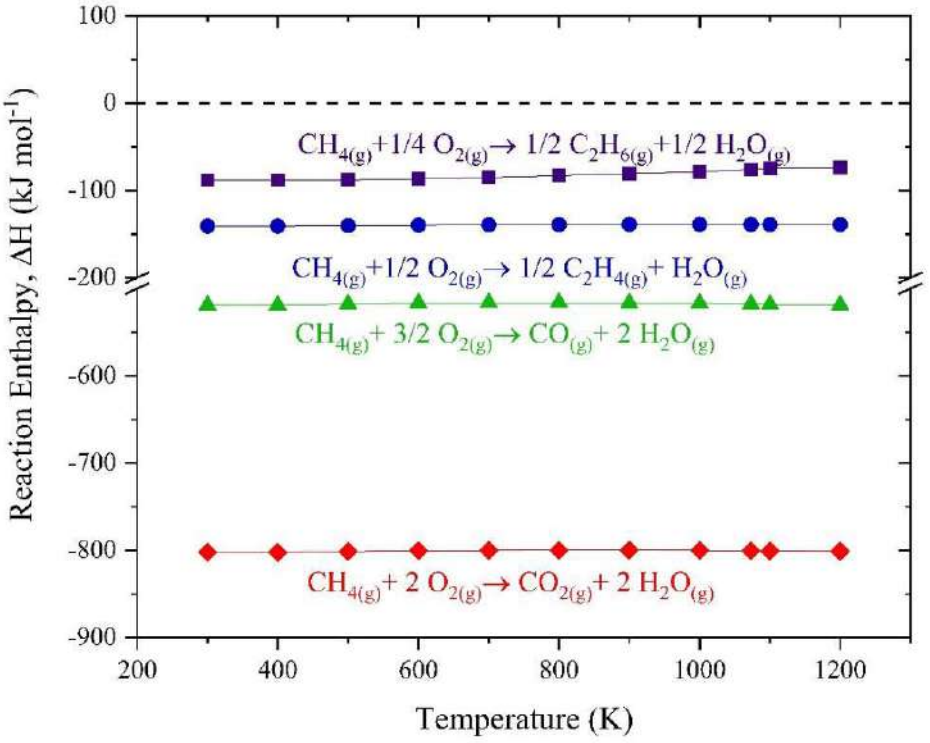

Figure A.1 Reaction Enthalpy as a function of temperature for a set of potential reactions that can occur on the OCM route at 1 atm.

Analogously, the entropy value (S_i) of a species *i* at a particular temperature *T* and pressure *P* is usually expressed in terms of entropy of formation of the species *i* ($S_i^{\circ}(T_r)$) at some reference temperature T_r plus the change in the entropy (ΔS_{Qi}) that results when the temperature is raised from the reference temperature T_r to the reaction temperature *T*, as follows:

$$S_i(T) = S_i^o(T_r) + \Delta S_{Qi} \quad \text{(A.10)}$$

The $S_i^o(T_r)$ is usually reported at 298.15 K and is found in the literature. For any species *i* that is being heated from T_r to *T* in absence of phase change, the change in the entropy (ΔS_{Qi}) is as follows:

$$\Delta S_{Qi} = \int_{T_r}^{T} \frac{C_{pi}}{T}\, dT \tag{A.11}$$

Substituting Equation A.11 in A.10, the entropy value ($S_i(T)$) of a species *i* at a particular reaction temperature *T* and a pressure *P* is:

$$S_i(T) = S_i^{\circ}(T_r) + \int_{T_r}^{T} \frac{C_{pi}}{T}\, dT \tag{A.12}$$

The entropy values of a reaction *r* described in Equation A.8 at temperature *T* is calculated as follows:

$$\Delta S_r(T) = \left[\sum_i v_i S_i(T)\right]_{products} - \left[\sum_i v_i S_i(T)\right]_{reactives} \tag{A.13}$$

Finally, the Gibbs free reaction energy is associated with a set of individual reactions at different temperatures by Equation 2.5.

$$\Delta G_r^T = \sum_i \upsilon_i \bullet \Delta H_r(T) \; - \; T \sum_i \upsilon_i \bullet \Delta S_r(T) \tag{2.5}$$

In which, ΔG_r^T is the Gibbs free reaction energy at a temperature *T*, in a certain reaction *r*, υ_i is the stoichiometric coefficient of the *i* species, and $\Delta H_r(T)$ and $\Delta S_r(T)$ are the change in the enthalpy and entropy of the *i* species at a temperature *T*, respectively.

Appendix B

Size of the Na_2WO_4 crystallites.

The size of the Na_2WO_4 crystallites supported on the Na_2WO_4/SiO_2 and Mn-Na_2WO_4/SiO_2 catalysts was determined by the X-ray line broadening method using the Scherrer equation, as follows:

$$D = \frac{k\lambda}{\beta_{hkl}\cos\theta} \tag{B.1}$$

In which, D is the crystallite size in nanometers, λ is the wavelength of the radiation (1.5406 Å for CuK_α radiation), k is the shape factor (~ 0.9 considering spherical shape), β_{hkl} is the peak full width at half-maximum (FWHM) intensity in radians, and θ is the peak position for the corresponding *hkl* peak in radians. Note that although the Bragg peak breadth is a combination of both instrument- and sample-induced effects, the former effects were neglected for the present estimation.

The three first reflections of the Na_2WO_4 phase on each catalyst, (1 1 1), (2 2 0), and (3 1 1), were adjusted by plotting $1/\beta_{hkl}$ on the x-axis and $\cos\theta$ along the y-axis, as follows:

$$\cos\theta = \frac{k\lambda}{D}\cdot\frac{1}{\beta_{hkl}} \tag{B.2}$$

The crystallite size was estimated from the slope of the fit lines in Figures B.1-B.2. The crystalline size of the Na_2WO_4 on the Na_2WO_4/SiO_2 and Mn-Na_2WO_4/SiO_2 catalysts is 533 and 375 nm, respectively.

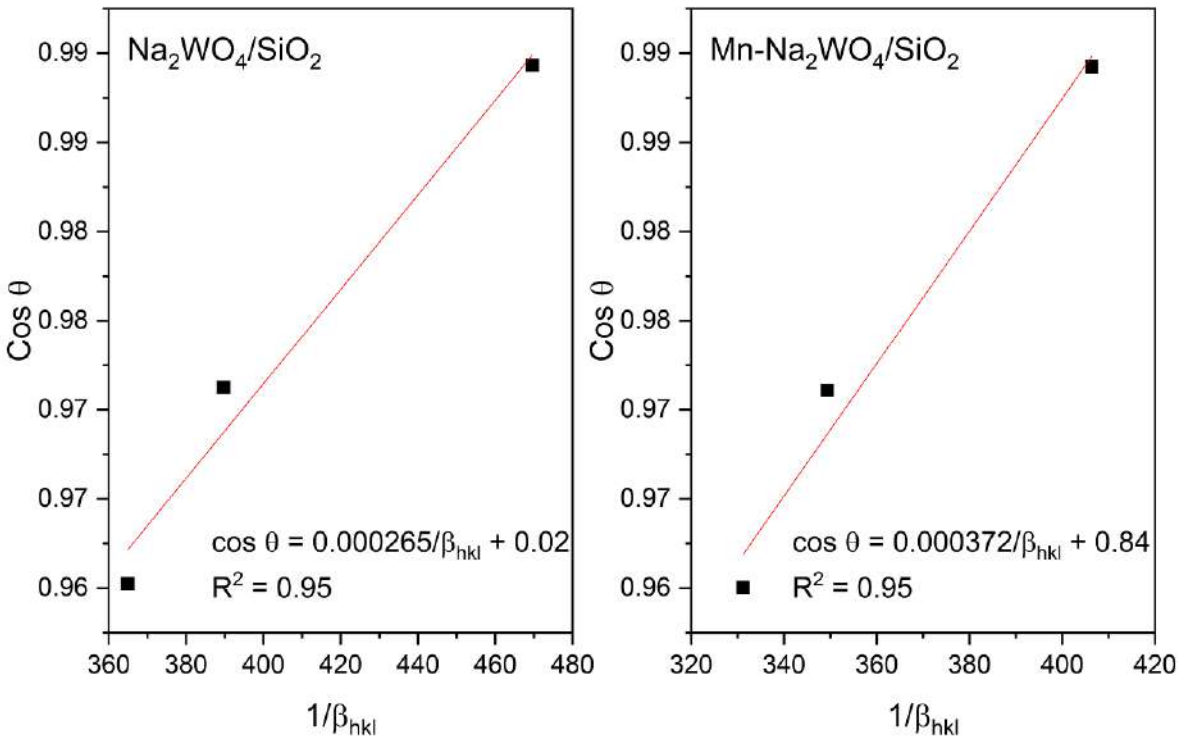

Figure B.1 Sherrer plot of Na_2WO_4 crystallites on the Na_2WO_4/SiO_2 and Mn-Na_2WO_4/SiO_2 catalysts. The crystallite size D is extracted from the slope of the fit lines.

Annex A

Licenses for Images Publication

Table 2.1

This Agreement between Dr. Carlos Ortiz Bravo ("You") and Elsevier ("Elsevier") consists of your license details and the terms and conditions provided by Elsevier and Copyright Clearance Center.

License Number	5114321194903
License date	Jul 22, 2021
Licensed Content Publisher	Elsevier
Licensed Content Publication	Fuel Processing Technology
Licensed Content Title	Kinetic modeling of oxidative coupling of methane over Mn/Na2WO4/SiO2 catalyst
Licensed Content Author	Mahdi Daneshpayeh,Abbasali Khodadadi,Navid Mostoufi,Yadolah Mortazavi,Rahmate Sotudeh-Gharebagh,Alireza Talebizadeh
Licensed Content Date	Mar 1, 2009
Licensed Content Volume	90
Licensed Content Issue	3
Licensed Content Pages	8
Start Page	403
End Page	410
Type of Use	reuse in a thesis/dissertation
Portion	figures/tables/illustrations
Number of figures/tables/illustrations	1
Format	both print and electronic
Are you the author of this Elsevier article?	No
Will you be translating?	No
Title	STRUCTURE OF THE Mn-Na2WO4/SiO2 CATALYST FOR OXIDATIVE COUPLING OF

	METHANE (OCM) AT REAL REACTION CONDITIONS
Institution name	Federal University of Rio de Janeiro - UFRJ
Expected presentation date	Aug 2021
Portions	Table 1
Requestor Location	Dr. Carlos Ortiz Bravo AVENIDA PRINCESA ISABEL 134, Ap 802 Rio de Janeiro, RJ 22011010 Brazil Attn: Dr. Carlos A. Ortiz-Bravo
Publisher Tax ID	GB 494 6272 12
Total	0.00 USD

Figure 2.6

This Agreement between Dr. Carlos Ortiz Bravo ("You") and Elsevier ("Elsevier") consists of your license details and the terms and conditions provided by Elsevier and Copyright Clearance Center.

License Number	5114340234711
License date	Jul 22, 2021
Licensed Content Publisher	Elsevier
Licensed Content Publication	Applied Catalysis A: General
Licensed Content Title	Mechanistic study of oxidative coupling of methane over Mn 2O3□Na 2 WO 4 SiO 2 catalyst
Licensed Content Author	Jingang Wu,Shuben Li,Jianzhong Niu,Xueping Fang
Licensed Content Date	Mar 30, 1995
Licensed Content Volume	124
Licensed Content Issue	1
Licensed Content Pages	10
Start Page	9
End Page	18
Type of Use	reuse in a thesis/dissertation
Portion	figures/tables/illustrations
Number of figures/tables/illustrations	1

Format	both print and electronic
Are you the author of this Elsevier article?	No
Will you be translating?	No
Title	STRUCTURE OF THE Mn-Na2WO4/SiO2 CATALYST FOR OXIDATIVE COUPLING OF METHANE (OCM) AT REAL REACTION CONDITIONS
Institution name	Federal University of Rio de Janeiro - UFRJ
Expected presentation date	Aug 2021
Portions	Fig. 5
Requestor Location	Dr. Carlos Ortiz Bravo AVENIDA PRINCESA ISABEL 134, Ap 802 Rio de Janeiro, RJ 22011010 Brazil Attn: Dr. Carlos A. Ortiz-Bravo
Publisher Tax ID	GB 494 6272 12
Total	0.00 USD

Bibliography

ALJAMA, H., NØRSKOV, J. K., ABILD-PEDERSEN, F. "Tuning Methane Activation Chemistry on Alkaline Earth Metal Oxides by Doping", **Journal of Physical Chemistry C**, v. 122, n. 39, pp. 22544–22548, 2018.

AMOS, R. D. "An accurate ab initio study of the multipole moments and polarizabilities of methane", **Molecular Physics**, v. 38, n. 1, pp. 33–45, 1979.

ANSHITS, A. G., VOSKRESENSKAYA, E. "Role of defect structure of active oxides in oxidative coupling of methane", **Catalysis Letters**, v. 6, n. 1, pp. 67–75, 1990.

ANSHITS, Alexander G., BAYUKOV, O. A., KONDRATENKO, E. V., *et al.* "Catalytic properties and nature of active centers of ferrospheres in oxidative coupling of methane", **Applied Catalysis A: General**, v. 524, pp. 192–199, 2016.

ARENA, F., TORRE, T., RAIMONDO, C., *et al.* "Structure and redox properties of bulk and supported manganese oxide catalysts", **Physical Chemistry Chemical Physics**, v. 3, n. 10, pp. 1911–1917, 2001.

ARNDT, S., OTREMBA, T., SIMON, U., *et al.* "Mn–Na2WO4/SiO2 as catalyst for the oxidative coupling of methane. What is really known?", **Applied Catalysis A: General**, v. 425–426, pp. 53–61, 2012.

ARNDT, S., SIMON, U., HEITZ, S., *et al.* "Li-doped MgO From Different Preparative Routes for the Oxidative Coupling of Methane", **Topics in Catalysis**, v. 54, n. 16–18, pp. 1266–1285, 2011.

ASAKURA, H., SHISHIDO, T., YAMAZOE, S., *et al.* "Structural Analysis of Group V, VI, and VII Metal Compounds by XAFS", **The Journal of Physical Chemistry C**, v. 115, n. 48, pp. 23653–23663, 2011.

BALERNA, A., BERNIERI, E., BURATTINI, E., *et al.* "EXAFS studies of MeO3−x (Me = W, Mo, Re, Ir) crystalline and amorphous oxides", **Nuclear Instruments and Methods in Physics Research Section A: Accelerators, Spectrometers, Detectors and Associated Equipment**, v. 308, n. 1–2, pp. 234–239, 1991.

BATES, J. B. "Raman Spectra of α and β Cristobalite", **The Journal of Chemical Physics**, v. 57, n. 9, pp. 4042–4047, 1972.

BERKOWITZ, J., GREENE, J. P., CHO, H., *et al.* "The ionization potentials of CH 4 and CD 4", **The Journal of Chemical Physics**, v. 86, n. 2, pp. 674–676, 1987.

BOULOVA, M., LUCAZEAU, G. "Crystallite Nanosize Effect on the Structural Transitions of WO3 Studied by Raman Spectroscopy", **Journal of Solid State Chemistry**, v. 167, n. 2, pp. 425–434, 2002.

BUCIUMAN, F., PATCAS, F., CRACIUN, R., *et al.* "Vibrational spectroscopy of bulk and supported manganese oxides", **Physical Chemistry Chemical Physics**, v. 1, n. 1, pp. 185–190, 1999.

CANT, N. W., KENNEDY, E. M., NELSON, P. F. "Magnitude and origin of the deuterium kinetic isotope effect during methane coupling and related reactions over lithium/magnesium oxide catalysts", **The Journal of Physical Chemistry**, v. 97, n. 7, pp. 1445–1450, 1993.

CANT, Noel W, LUKEY, C. A., NELSON, P. F., *et al.* "The rate controlling step in the oxidative coupling of methane over a lithium-promoted magnesium oxide catalyst", **Journal of the Chemical Society, Chemical Communications**, n. 12, pp. 766, 1988.

CHASE, M. W. . J. "NIST-JANAF Themochemical Tables, Fourth Edition", **J. Phys. Chem. Ref. Data, Monograph 9**, pp. 1–1951, 1998.

CHIESA, M., GIAMELLO, E., CHE, M. "EPR characterization and reactivity of surface-localized inorganic radicals and radical ions", **Chemical Reviews**, v. 110, n. 3, pp. 1320–1347, 2010.

CHRÉTIEN, S., METIU, H. "Acid–Base Interaction and Its Role in Alkane Dissociative Chemisorption on Oxide Surfaces", **The Journal of Physical Chemistry C**, v. 118, n. 47, pp. 27336–27342, 2014.

CHUA, Y. T., MOHAMED, A. R., BHATIA, S. "Oxidative coupling of methane for the production of ethylene over sodium-tungsten-manganese-supported-silica catalyst (Na-W-Mn/SiO2)", **Applied Catalysis A: General**, v. 343, n. 1–2, pp. 142–148, 2008.

CRUELLAS, A., BAKKER, J. J., VAN SINT ANNALAND, M., *et al.* "Techno-economic analysis of oxidative coupling of methane: Current state of the art and future perspectives", **Energy Conversion and Management**, v. 198, n. April, pp. 111789, 2019.

DATA, S. S., REFERENCES, S. "Search Sample Data Us Search References About RRUFF Contact Natrolite R060561", **Cell**, pp. 1–2, 2009.

DEBOY, J. "Kinetics of the oxidative coupling of methane over 1 wt% Sr/La2O3", **Journal of Catalysis**, v. 113, n. 2, pp. 517–524, 1988.

DOOLEY, S., BURKE, M. P., CHAOS, M., *et al.* "Methyl formate oxidation: Speciation data, laminar burning velocities, ignition delay times, and a validated chemical kinetic model", **International Journal of Chemical Kinetics**, v. 42, n. 9, pp. 527–549, 2010.

DRISCOLL, D. J., MARTIR, W., WANG, J.-X., *et al.* "Formation of gas-phase methyl radicals over MgO", **Journal of the American Chemical Society**, v. 107, n. 1, pp. 58–63, 1985.

DUBOIS, J.-L., CAMERON, C. J. "Common features of oxidative coupling of methane cofeed catalysts", **Applied Catalysis**, v. 67, n. 1, pp. 49–71, 1990.

ELKINS, T. W., HAGELIN-WEAVER, H. E. "Characterization of Mn–Na2WO4/SiO2 and Mn–Na2WO4/MgO catalysts for the oxidative coupling of methane", **Applied Catalysis A: General**, v. 497, pp. 96–106, 2015.

FAN, D., DAI, D. J., WU, H. S. "Ethylene formation by catalytic dehydration of ethanol with industrial considerations", **Materials**, v. 6, n. 1, pp. 101–115, 2013.

FANG, X., LI, S., LIN, J., *et al.* "Oxidative Coupling of Methane on W-Mn Catalysts", **Journal of Molecular Catalysis (China)**, v. 6, n. 6, pp. 427–433, 1992.

FARRELL, B. L., IGENEGBAI, V. O., LINIC, S. "A Viewpoint on Direct Methane Conversion to Ethane and Ethylene Using Oxidative Coupling on Solid Catalysts", **ACS Catalysis**, v. 6, n. 7, pp. 4340–4346, 2016.

FIGUEROA, S J A, MAURICIO, J. C., MURARI, J., *et al.* "Upgrades to the XAFS2

beamline control system and to the endstation at the LNLS", **Journal of Physics: Conference Series**, v. 712, n. 1, pp. 012022, 2016.

FIGUEROA, Santiago J. A., GIBSON, D., MAIRS, T., *et al.* "Innovative insights in a plug flow microreactor for operando X-ray studies", **Journal of Applied Crystallography**, v. 46, n. 5, pp. 1523–1527, 2013.

FLEISCHER, V., SIMON, U., PARISHAN, S., *et al.* "Investigation of the role of the Na2WO4/Mn/SiO2catalyst composition in the oxidative coupling of methane by chemical looping experiments", **Journal of Catalysis**, v. 360, pp. 102–117, 2018.

FLEISCHER, V., STEUER, R., PARISHAN, S., *et al.* "Investigation of the surface reaction network of the oxidative coupling of methane over Na2WO4/Mn/SiO2catalyst by temperature programmed and dynamic experiments", **Journal of Catalysis**, v. 341, pp. 91–103, 2016.

GAMBO, Y., JALIL, A. A., TRIWAHYONO, S., *et al.* "Recent advances and future prospect in catalysts for oxidative coupling of methane to ethylene: A review", **Journal of Industrial and Engineering Chemistry**, v. 59, pp. 218–229, 2018.

GARCIA-GARCIA, F. J., GIL-ROSTRA, J., YUBERO, F., *et al.* "“In Operando” X-ray Absorption Spectroscopy Analysis of Structural Changes During Electrochemical Cycling of WO3 and WxSiyOz Amorphous Electrochromic Thin Film Cathodes", **The Journal of Physical Chemistry C**, v. 119, n. 1, pp. 644–652, 2015.

GARCÍA-LÓPEZ, E. I., MARCÌ, G., KRIVTSOV, I., *et al.* "Local Structure of Supported Keggin and Wells-Dawson Heteropolyacids and Its Influence on the Catalytic Activity", **Journal of Physical Chemistry C**, v. 123, n. 32, pp. 19513–19527, 2019.

GARRONE, E., ZECCHINA, A., STONE, F. S. "Anionic intermediates in surface processes leading to O2-; formation on magnesium oxide", **Journal of Catalysis**, v. 62, n. 2, pp. 396–400, 1980.

GHOLIPOUR, Z., MALEKZADEH, A., HATAMI, R., *et al.* "Oxidative coupling of methane over (Na2WO4+Mn or Ce)/SiO2 catalysts: In situ measurement of electrical conductivity", **Journal of Natural Gas Chemistry**, v. 19, n. 1, pp. 35–42, 2010.

GODINI, H. R., GILI, A., GÖRKE, O., *et al.* "Sol–gel method for synthesis of Mn–Na2WO4/SiO2 catalyst for methane oxidative coupling", **Catalysis Today**, v. 236, n. PART A, pp. 12–22, 2014.

GORDIENKO, Y., USMANOV, T., BYCHKOV, V., *et al.* "Oxygen availability and catalytic performance of NaWMn/SiO2 mixed oxide and its components in oxidative coupling of methane", **Catalysis Today**, v. 278, pp. 127–134, 2016.

GREENWOOD, N. N., EARNSHAW, A. **Chemistry of the elements**. 2 n.d. ed. Oxford, Butterworth-Heinemann, 1998.

GUO, X., FANG, G., LI, G., *et al.* "Direct, Nonoxidative Conversion of Methane to Ethylene, Aromatics, and Hydrogen", **Science**, v. 344, n. 6184, pp. 616–619, 2014.

HARDCASTLE, F. D., WACHS, I. E. "Determination of the molecular structures of tungstates by Raman spectroscopy", **Journal of Raman Spectroscopy**, v. 26, n. 6, pp. 397–405, 1995.

HORN, R., SCHLÖGL, R. "Methane Activation by Heterogeneous Catalysis", **Catalysis Letters**, v. 145, n. 1, pp. 23–39, 2015.

HORSLEY, J. A., WACHS, I. E., BROWN, J. M., *et al.* "Structure of surface tungsten oxide species in the tungsten trioxide/alumina supported oxide system from x-ray absorption near-edge spectroscopy and Raman spectroscopy", **The Journal of Physical Chemistry**, v. 91, n. 15, pp. 4014–4020, 1987.

HOWELL, J. G., LI, Y. P., BELL, A. T. "Propene Metathesis over Supported Tungsten Oxide Catalysts: A Study of Active Site Formation", **ACS Catalysis**, v. 6, n. 11, pp. 7728–7738, 2016.

HUANG, K., MILLER, J. B., HUBER, G. W., *et al.* "A General Framework for the Evaluation of Direct Nonoxidative Methane Conversion Strategies", **Joule**, v. 2, n. 2, pp. 349–365, 2018.

IULIANELLI, A., LIGUORI, S., WILCOX, J., *et al.* "Advances on methane steam reforming to produce hydrogen through membrane reactors technology: A review", **Catalysis Reviews - Science and Engineering**, v. 58, n. 1, pp. 1–35, 2016.

IWASAWA, Y., ASAKURA, K., TADA, M. **XAFS Techniques for Catalysts, Nanomaterials, and Surfaces**. Cham, Springer International Publishing, 2017. Disponível em: http://link.springer.com/10.1007/978-3-319-43866-5.

JANG, W. J., SHIM, J. O., KIM, H. M., *et al.* "A review on dry reforming of methane in aspect of catalytic properties", **Catalysis Today**, pp. 15–26, 2019.

JI, S. F., XIAO, T. C., LI, S. B., *et al.* "Surface WO4 tetrahedron: the essence of the oxidative coupling of methane over M-W-Mn/SiO2 catalysts", **Journal of Catalysis**, v. 220, n. 1, pp. 47–56, 2003.

JI, S. F., XIAO, T. C., LI, S. B., *et al.* "The relationship between the structure and the performance of Na-W-Mn/SiO2 catalysts for the oxidative coupling of methane", **Applied Catalysis A: General**, v. 225, n. 1–2, pp. 271–284, 2002.

JIANG, Z. C., GONG, H., LI, S. B. "Methane activation over Mn2O3-Na2WO4/SiO2 catalyst and oxygen spillover", **Stud. Surf. Sci. Catal.**, v. 112, pp. 481–490, 1997.

JIANG, Z. C., YU, C. J., FANG, X, *et al.* "Oxide/support interaction and surface reconstruction in the sodium tungstate(Na2WO4)/silica system", **The Journal of Physical Chemistry**, v. 97, n. 49, pp. 12870–12875, 1993.

JONES, C. A., LEONARD, J. J., SOFRANKO, J. A. "The oxidative conversion of methane to higher hydrocarbons over alkali-promoted Mn SiO2", **Journal of Catalysis**, v. 103, n. 2, pp. 311–319, 1987.

KARAKAYA, C., KEE, R. J. "Progress in the direct catalytic conversion of methane to fuels and chemicals", **Progress in Energy and Combustion Science**, v. 55, pp. 60–97, 2016.

KELLER, G. E., BHASIN, M. M. "Synthesis of ethylene via oxidative coupling of methane I. Determination of active catalysts", **Journal of Catalysis**, v. 73, n. 1, pp. 9–19, 1982.

KERR, R. A. "Natural gas from shale bursts onto the scene", **Science**, v. 328, n. 5986, pp. 1624–1626, 2010.

KHYZHUN, O. Y. "XPS, XES and XAS studies of the electronic structure of tungsten

oxides", **Journal of Alloys and Compounds**, v. 305, n. 1–2, pp. 1–6, 2000.

KIANI, D., SOURAV, S., BALTRUSAITIS, J., *et al.* "Oxidative Coupling of Methane (OCM) by SiO2-Supported Tungsten Oxide Catalysts Promoted with Mn and Na", **ACS Catalysis**, v. 9, n. 7, pp. 5912–5928, 2019.

KIANI, D., SOURAV, S., WACHS, I. E., *et al.* "Synthesis and molecular structure of model silica-supported tungsten oxide catalysts for oxidative coupling of methane (OCM)", **Catalysis Science & Technology**, v. 10, n. 10, pp. 3334–3345, 2020.

KOU, Y., ZHANG, B., NIU, J., *et al.* "Amorphous Features of Working Catalysts: XAFS and XPS Characterization of Mn/Na2WO4/SiO2 as used for the Oxidative Coupling of Methane", **Journal of Catalysis**, v. 173, n. 2, pp. 399–408, 1998a.

KUO, J. C. W., KRESGE, C. T., PALERMO, R. E. "Evaluation of direct methane conversion to higher hydrocarbons and oxygenates", **Catalysis Today**, v. 4, n. 3–4, pp. 463–470, 1989.

LACOMBE, S., DURJANOVA, Z., MLECZKO, L., *et al.* "Kinetic modelling of the oxidative coupling of methane over lanthanum oxide in connection with mechanistic studies", **Chemical Engineering & Technology**, v. 18, n. 3, pp. 216–223, 1995.

LEE, J. Y., JEON, W., CHOI, J. W., *et al.* "Scaled-up production of C2 hydrocarbons by the oxidative coupling of methane over pelletized Na2WO4/Mn/SiO 2 catalysts: Observing hot spots for the selective process", **Fuel**, v. 106, pp. 851–857, 2013.

LEE, M. R., PARK, M. J., JEON, W., *et al.* "A kinetic model for the oxidative coupling of methane over Na2WO4/Mn/SiO2", **Fuel Processing Technology**, v. 96, pp. 175–182, 2012.

LI, C., YAN, W., XIN, Q. "Interaction of methane with surface of alumina studied by FT-IR spectroscopy", **Catalysis Letters**, v. 24, n. 3–4, pp. 249–256, 1994.

LIMA, C. L., SARAIVA, G. D., FREIRE, P. T. C., *et al.* "Temperature-induced phase transformations in Na2WO4 and Na2MoO4 crystals", **Journal of Raman Spectroscopy**, v. 42, n. 4, pp. 799–802, 2011.

LIMAYE, M. V, CHEN, J. S., SINGH, S. B., *et al.* "Correlation between

electrochromism and electronic structures of tungsten oxide films", **RSC Advances**, v. 4, n. 10, pp. 5036–5045, 2014.

LIN, C.-H., CAMPBELL, K. D., WANG, J.-X., *et al.* "Oxidative dimerization of methane over lanthanum oxide", **The Journal of Physical Chemistry**, v. 90, n. 4, pp. 534–537, 1986.

LIU, H., WANG, X., YANG, D., *et al.* "Scale up and stability test for oxidative coupling of methane over Na2WO4-Mn/SiO2 catalyst in a 200 ml fixed-bed reactor", **Journal of Natural Gas Chemistry**, v. 17, n. 1, pp. 59–63, 2008.

LIU, H., YANG, D., GAO, R., *et al.* "A novel Na2WO4–Mn/SiC monolithic foam catalyst with improved thermal properties for the oxidative coupling of methane", **Catalysis Communications**, v. 9, n. 6, pp. 1302–1306, 2008.

LOMONOSOV, V. I., SINEV, M. Y. "Oxidative coupling of methane: Mechanism and kinetics", **Kinetics and Catalysis**, v. 57, n. 5, pp. 647–676, 2016.

LUNSFORD, J. H. "The role of surface-generated gas-phase radicals in catalysis", **Langmuir**, v. 5, n. 1, pp. 12–16, 1989.

MAHMOODI, S., EHSANI, M. R., GHOREISHI, S. M. "Effect of promoter in the oxidative coupling of methane over synthesized Mn/SiO2 nanocatalysts via incipient wetness impregnation", **Journal of Industrial and Engineering Chemistry**, v. 16, n. 6, pp. 923–928, 2010.

MAITRA, A. M. "Critical performance evaluation of catalysts and mechanistic implications for oxidative coupling of methane", **Applied Catalysis A: General**, v. 104, n. 1, pp. 11–59, 1993.

MALEKZADEH, A., KHODADADI, A., ABEDINI, M., *et al.* "Correlation of electrical properties and performance of OCM MOx/Na2WO4/SiO2catalysts", **Catalysis Communications**, v. 2, n. 8, pp. 241–247, 2001.

MAZZARA, C., JUPILLE, J., FLANK, A.-M., *et al.* "Stereochemical Order around Sodium in Amorphous Silica", **The Journal of Physical Chemistry B**, v. 104, n. 15, pp. 3438–3445, 2000.

MCFARLAND, E. "Unconventional Chemistry for Unconventional Natural Gas", **Science**, v. 338, n. 6105, pp. 340–342, 2012.

NIST. **NIST Chemistry WebBook**. NIST Chemistry WebBook. Disponível em: https://webbook.nist.gov/cgi/cbook.cgi?ID=C74851&Units=SI&Mask=1&Type=JANAFG&Table=on#JANAFG. Acesso em: 29 out. 2019.

OLSBYE, U., DESGRANDCHAMPS, G., JENS, K.-J., *et al.* "A kinetic study of the oxidative coupling of methane over a BaCO3 / La2On(CO3)3-n catalyst", **Catalysis Today**, v. 13, n. 2–3, pp. 209–218, 1992.

ORTIZ-BRAVO, C. A., FIGUEROA, S. J. A., PORTELA, R., *et al.* "Elucidating the structure of the W and Mn sites on the Mn-Na2WO4/SiO2 catalyst for the oxidative coupling of methane (OCM) at real reaction temperatures", **Journal of Catalysis**, n. in press, 2021.

ORTIZ-ESPINOZA, A. P., NOURELDIN, M. M. B., EL-HALWAGI, M. M., *et al.* "Design, simulation and techno-economic analysis of two processes for the conversion of shale gas to ethylene", **Computers and Chemical Engineering**, v. 107, pp. 237–246, 2017.

PAGANINI, M. C., CHIESA, M., MARTINO, P., *et al.* "EPR Study of the Surface Basicity of Calcium Oxide. 2: The Interaction with Alkanes", **The Journal of Physical Chemistry B**, v. 107, n. 11, pp. 2575–2580, 2003.

PAK, S., LUNSFORD, J. H. "Thermal effects during the oxidative coupling of methane over Mn/Na2WO4/SiO2 and Mn/Na2WO4/MgO catalysts", **Applied Catalysis A: General**, v. 168, n. 1, pp. 131–137, 1998.

PAK, S., QIU, P., LUNSFORD, J. H. "Elementary Reactions in the Oxidative Coupling of Methane over Mn/Na 2 WO 4 /SiO 2 and Mn/Na 2 WO 4 /MgO Catalysts", **Journal of Catalysis**, v. 179, n. 1, pp. 222–230, 1998a.

PAK, S., QIU, P., LUNSFORD, J. H. "Elementary Reactions in the Oxidative Coupling of Methane over Mn/Na 2 WO 4 /SiO 2 and Mn/Na 2 WO 4 /MgO Catalysts", **Journal of Catalysis**, v. 179, pp. 222–230, 1998b.

PALERMO, A, HOLGADO VAZQUEZ, J. P., LEE, A. F., *et al.* "Critical influence of the amorphous silica-to-cristobalite phase transition on the performance of Mn/Na2WO4/SiO2 catalysts for the oxidative coupling of methane", **Journal of Catalysis**, v. 177, n. 2, pp. 259–266, 1998.

PALERMO, Alejandra, HOLGADO VAZQUEZ, J. P., LAMBERT, R. M. "New efficient catalysts for the oxidative coupling of methane", **Catalysis Letters**, v. 68, n. 3–4, pp. 191–196, 2000.

POKHREL, S., BIRKENSTOCK, J., DIANAT, A., *et al.* "In situ high temperature X-ray diffraction, transmission electron microscopy and theoretical modeling for the formation of WO3 crystallites", **CrystEngComm**, v. 17, n. 36, pp. 6985–6998, 2015.

R090057 - RRUFF Database: Raman, X-ray, Infrared, and Chemistry. [S.d.]. Disponível em: https://rruff.info/general=Braunite/display=default/R090057. Acesso em: 3 abr. 2021.

RAVEL, B., NEWVILLE, M. "ATHENA , ARTEMIS , HEPHAESTUS : data analysis for X-ray absorption spectroscopy using IFEFFIT", **Journal of Synchrotron Radiation**, v. 12, n. 4, pp. 537–541, 2005.

RICHET, P., MYSEN, B. O. "High-temperature dynamics in cristobalite (SiO2) and carnegieite (NaAlSiO4): A Raman spectroscopy study", **Geophysical Research Letters**, v. 26, n. 15, pp. 2283–2286, 1999.

ROSS-MEDGAARDEN, E. I., WACHS, I. E. "Structural Determination of Bulk and Surface Tungsten Oxides with UV−vis Diffuse Reflectance Spectroscopy and Raman Spectroscopy", **The Journal of Physical Chemistry C**, v. 111, n. 41, pp. 15089–15099, 2007.

RYTTER, E., HOLMEN, A. "Deactivation and regeneration of commercial type fischer-tropsch co-catalysts—A mini-review", **Catalysts**, v. 5, n. 2, pp. 478–499, 2015.

SADJADI, S., JAŠO, S., GODINI, H. R., *et al.* "Feasibility study of the Mn-Na2WO4/SiO2 catalytic system for the oxidative coupling of methane in a fluidized-bed reactor", **Catalysis Science and Technology**, v. 5, n. 2, pp. 942–952, 2015.

SCHWACH, P., PAN, X., BAO, X. "Direct Conversion of Methane to Value-Added Chemicals over Heterogeneous Catalysts: Challenges and Prospects", **Chemical Reviews**, v. 117, n. 13, pp. 8497–8520, 2017.

SHAHRI, S. M. K., ALAVI, S. M. "Kinetic studies of the oxidative coupling of methane over the Mn/Na2WO4/SiO2 catalyst", **Journal of Natural Gas Chemistry**, v. 18, n. 1, pp. 25–34, 2009.

SIMON, U., GÖRKE, O., BERTHOLD, A., *et al.* "Fluidized bed processing of sodium tungsten manganese catalysts for the oxidative coupling of methane", **Chemical Engineering Journal**, v. 168, n. 3, pp. 1352–1359, 2011.

SINEV, M., PONOMAREVA, E., SINEV, I., *et al.* "Oxygen pathways in oxidative coupling of methane and related processes . Case study : NaWMn / SiO 2 catalyst", **Catalysis Today**, v. 333, n. April 2018, pp. 36–46, 2019.

SINEV, M. Y. "Free radicals in catalytic oxidation of light alkanes : kinetic and thermochemical aspects", **Journal of Catalysis**, homolytical activation of methane is more favorable, v. 216, pp. 468–476, 2003.

SOHRABI, M., DABIR, B., ESKANDARI, A., *et al.* "Some aspects of kinetics and mechanism of the oxidative coupling of methane", **Journal of Chemical Technology and Biotechnology**, v. 67, n. 1, pp. 15–20, 1996.

SPALLINA, V., VELARDE, I. C., JIMENEZ, J. A. M., *et al.* "Techno-economic assessment of different routes for olefins production through the oxidative coupling of methane (OCM): Advances in benchmark technologies", **Energy Conversion and Management**, v. 154, pp. 244–261, 2017.

SPIVEY, J. J., HUTCHINGS, G. "Catalytic aromatization of methane", **Chem. Soc. Rev.**, v. 43, n. 3, pp. 792–803, 2014.

STANSCH, Z., MLECZKO, L., BAERNS, M. "Comprehensive Kinetics of Oxidative Coupling of Methane over the La2O3/CaO Catalyst", **Industrial & Engineering Chemistry Research**, v. 36, n. 7, pp. 2568–2579, 1997.

STOBBE, E. R. R., DE BOER, B. A. A., GEUS, J. W. W. "The reduction and oxidation

behaviour of manganese oxides", **Catalysis Today**, v. 47, n. 1–4, pp. 161–167, 1999.

SUN, J., THYBAUT, J. W., MARIN, G. B. "Microkinetics of methane oxidative coupling", **Catalysis Today**, v. 137, n. 1, pp. 90–102, 2008.

TAIFAN, W., BALTRUSAITIS, J. "CH4 conversion to value added products: Potential, limitations and extensions of a single step heterogeneous catalysis", **Applied Catalysis B: Environmental**, v. 198, pp. 525–547, 2016.

TAKANABE, K., IGLESIA, E. "Mechanistic aspects and reaction pathways for oxidative coupling of methane on Mn/Na2WO4/SiO2catalysts", **Journal of Physical Chemistry C**, v. 113, n. 23, pp. 10131–10145, 2009.

THUMMAVICHAI, K., WANG, N., XU, F., *et al.* "In situ investigations of the phase change behaviour of tungsten oxide nanostructures", **Royal Society Open Science**, v. 5, n. 4, 2018.

TIEMERSMA, T. P., TUINIER, M. J., GALLUCCI, F., *et al.* "A kinetics study for the oxidative coupling of methane on a Mn/Na2WO4/SiO2 catalyst", **Applied Catalysis A: General**, v. 433–434, pp. 96–108, 2012.

TRAYKOVA, M., DAVIDOVA, N., TSAIH, J. S., *et al.* "Oxidative coupling of methane - The transition from reaction to transport control over La2O3/MgO catalyst", **Applied Catalysis A: General**, v. 169, n. 2, pp. 237–247, 1998.

VAMVAKEROS, A., JACQUES, S. D. M. M., MIDDELKOOP, V., *et al.* "Real time chemical imaging of a working catalytic membrane reactor during oxidative coupling of methane", **Chemical Communications**, v. 51, n. 64, pp. 12752–12755, 2015a.

VAMVAKEROS, A., JACQUES, S. D. M., MIDDELKOOP, V., *et al.* "Real time chemical imaging of a working catalytic membrane reactor during oxidative coupling of methane", **Chemical Communications**, v. 51, n. 64, pp. 12752–12755, 2015b.

VAMVAKEROS, Antonis, MATRAS, D., JACQUES, S. D. M., *et al.* "Real-time multi-length scale chemical tomography of fixed bed reactors during the oxidative coupling of methane reaction", **Journal of Catalysis**, v. 386, pp. 39–52, 2020.

VOGT, T., WOODWARD, P. M., HUNTER, B. A. "The High-Temperature Phases of

WO3", **Journal of Solid State Chemistry**, v. 144, n. 1, pp. 209–215, 1999.

VOSKRESENSKAYA, E. N., ANSHITS, A. G., ROGULEVA, V. "Oxidant activation over structural defects of oxide catalysts in oxidative methane coupling", **Catalysis Reviews**, v. 37, n. 1, pp. 101–143, 1995.

WANG, D. J., ROSYNEK, M. P., LUNSFORD, J. H. "Oxidative Coupling of Methane over Oxide-Supported Sodium-Manganese Catalysts", **Journal of Catalysis**, v. 155, n. 2, pp. 390–402, 1995.

WANG, H., SCHMACK, R., PAUL, B., *et al.* "Porous silicon carbide as a support for Mn/Na/W/SiC catalyst in the oxidative coupling of methane", **Applied Catalysis A: General**, v. 537, pp. 33–39, 2017.

WANG, Jian, YOU, J., WANG, M., *et al.* "In-situ high-temperature Raman spectroscopic studies of the vibrational characteristics and microstructure evolution of sodium tungstate dihydrate crystal during heating and melting", **Journal of Raman Spectroscopy**, v. 49, n. 10, pp. 1693–1705, 2018.

WANG, Jiaxin, CHOU, L., ZHANG, B., *et al.* "Comparative study on oxidation of methane to ethane and ethylene over Na2WO4-Mn/SiO2catalysts prepared by different methods", **Journal of Molecular Catalysis A: Chemical**, v. 245, n. 1–2, pp. 272–277, 2006.

WANG, P., ZHAO, G., LIU, Y., *et al.* "TiO2-doped Mn2O3-Na2WO4/SiO2 catalyst for oxidative coupling of methane: Solution combustion synthesis and MnTiO3-dependent low-temperature activity improvement", **Applied Catalysis A: General**, v. 544, n. May, pp. 77–83, 2017.

WANG, P., ZHAO, G., WANG, Y., *et al.* "MnTiO 3 -driven low-temperature oxidative coupling of methane over TiO 2 -doped Mn 2 O 3 -Na 2 WO 4 /SiO 2 catalyst", **Science Advances**, v. 3, n. 6, pp. e1603180, 2017.

WANG, TAO, L., XIE, M., *et al.* "Dehydrogenation and aromatization of methane under non-oxidizing conditions", **Catalysis Letters**, v. 21, n. 1–2, pp. 35–41, 1993.

WANG, Y. C., HSU, C. H., HSU, Y. Y., *et al.* "Structural distortion and electronic

states of Rb doped WO 3 by X-ray absorption spectroscopy", **RSC Advances**, v. 6, n. 109, pp. 107871–107877, 2016.

WECKHUYSEN, B. M., WANG, D., ROSYNEK, M. P., *et al.* "Conversion of methane to benzene over transition metal ion ZSM-5 zeolites: I. Catalytic characterization", **Journal of Catalysis**, v. 175, n. 2, pp. 338–346, 1998.

WEI, H., LENG, W., SONG, J., *et al.* "Improved Quantitative SERS Enabled by Surface Plasmon Enhanced Elastic Light Scattering", **Analytical Chemistry**, v. 90, n. 5, pp. 3227–3237, 2018.

WERNY, M. J., WANG, Y., GIRGSDIES, F., *et al.* "Fluctuating Storage of the Active Phase in a Mn-Na 2 WO 4 /SiO 2 Catalyst for the Oxidative Coupling of Methane", **Angewandte Chemie**, v. 132, n. 35, pp. 15031–15036, 2020.

WU, J., LI, S. "The Role of Distorted WO4 in the Oxidative Coupling of Methane on Supported Tungsten Oxide Catalysts", **The Journal of Physical Chemistry**, v. 99, n. 13, pp. 4566–4568, 1995.

WU, J., *et al.* "Mechanistic study of oxidative coupling of methane over Mn2O3-Na2WO4SiO2 catalyst", **Applied Catalysis A: General**, v. 124, n. 1, pp. 9–18, 1995.

YAMAZOE, S., HITOMI, Y., SHISHIDO, T., *et al.* "XAFS Study of Tungsten L1 - and L3-Edges: Structural Analysis of WO3 Species Loaded on TiO2 as a Catalyst for Photo-oxidation of NH3", **The Journal of Physical Chemistry C**, v. 112, n. 17, pp. 6869–6879, 2008.

YILDIZ, M., AKSU, Y., SIMON, U., *et al.* "Enhanced catalytic performance of MnxOy–Na2WO4/SiO 2 for the oxidative coupling of methane using an ordered mesoporous silica support", **Chem. Commun.**, v. 50, n. 92, pp. 14440–14442, 2014.

YILDIZ, M., AKSU, Y., SIMON, U., *et al.* "Silica material variation for the MnxOy-Na2WO4/SiO2", **Applied Catalysis A: General**, v. 525, pp. 168–179, 2016.

YILDIZ, M., SIMON, U., OTREMBA, T., *et al.* "Support material variation for the MnxOy-Na2WO4/SiO2 catalyst", **Catalysis Today**, v. 228, pp. 5–14, 2014.

YU, Z., YANG, X., LUNSFORD, J. H., *et al.* "Oxidative Coupling of Methane over

Na2WO4/CeO2 and Related Catalysts", **Journal of Catalysis**, v. 154, n. 1, pp. 163–173, 1995.

YUNARTI, R. T., GU, S., CHOI, J. W., *et al.* "Oxidative Coupling of Methane Using Mg/Ti-Doped SiO2-Supported Na2WO4/Mn Catalysts", **ACS Sustainable Chemistry and Engineering**, v. 5, n. 5, pp. 3667–3674, 2017.

ZENG, J. L., XIONG, Z. T., ZHANG, H. Bin, *et al.* "Nonoxidative dehydrogenation and aromatization of methane over W/HZSM-5-based catalysts", **Catalysis Letters**, v. 53, n. 1, pp. 119–124, 1998.

ZHAN, C. G., NICHOLS, J. A., DIXON, D. A. "Ionization potential, electron affinity, electronegativity, hardness, and electron excitation energy: Molecular properties from density functional theory orbital energies", **Journal of Physical Chemistry A**, v. 107, n. 20, pp. 4184–4195, 2003.

ZHANG, Z., BAERNS, M., VERYKIOS, X. E. "Effect of electronic properties of catalysts for the oxidative coupling of methane on their selectivity and activity", **Catalysis Reviews**, v. 36, n. 3, pp. 507–556, 1994.